MODULATING OPTICAL AND ELECTRONIC PROPERTIES IN SILICON NANOWIRE SUPERLATTICES

David John Hill

A dissertation submitted to the faculty of the University of North Carolina at Chapel Hill in partial fulfillment of the requirements for the degree of Doctor of Philosophy in the Department of Chemistry.

Chapel Hill
2018

Approved by:

James F. Cahoon

Joanna M. Atkin

Scott C. Warren

Frank A. Leibfarth

Jillian L. Dempsey

©2018
David John Hill
ALL RIGHTS RESERVED

ABSTRACT

David John Hill: Modulating Optical and Electronic Properties in Silicon Nanowire Superlattices
(Under the direction of James F. Cahoon)

Here, we develop new techniques for implementing silicon nanowires (NWs) in complex photonic and electronic applications. First, we present waveguide scattering microscopy (WSM) as an alternative technique to dark-field microscopy (DFM) to image and analyze photonic nanostructures. WSM uses a white-light source coupled to a dielectric slab waveguide to generate an evanescent field that illuminates objects on the waveguide surface. We demonstrate high-contrast dark-field imaging of nanophotonic and plasmonic structures such as Si nanowires, Au nanorods, and Ag nanoholes. Scattering spectra collected in the WSM configuration show excellent signal-to-noise with minimal background signal compared to conventional DFM. In addition, the polarization of the incident field is controlled by the direction of the propagating wave, providing a straightforward route to excite specific optical modes in anisotropic nanostructures.

We also overcome several difficulties of VLS NW growth, such as nonselective deposition, kinking, and compositional gradients, and report the synthesis of uniform, linear, and degenerately doped Si NW superlattices. The synthesis is enabled by *in situ* chlorination of the NW surface with hydrochloric acid. We find the boron doping level to far exceed the solid solubility limit, resulting from crystallization kinetics. Because the boron and phosphorus doping levels are degenerate, both segments inhibit the etching of Si in basic solutions. Moreover, we find that the dopant transitions are abrupt, facilitating morphological control with a spatial resolution of $\sim$ 10 nm.

We delineate how the photovoltaic performance of NWs with axial *p-i-n* junctions is dictated not simply by the surface but also by the complex interplay of diode geometry - i.e. radius (R) and intrinsic length (L_i) - with the surface recombination velocity (S). Using a combination of finite-element simulations, analytical theory, and single-NW measurements, we evaluate the dependence of the dark saturation current (I_o), internal quantum efficiency (IQE), short-circuit current (I_{SC}), and open-circuit voltage (V_{OC}) on both geometric and recombination parameters, highlighting various trade offs in the

performance metrics. The results presented herein enable the growth of complex, degenerately doped *p-n* junction nanostructures and provide guidance for the rational design of photodiode and photovoltaic devices that can be explored for advanced NW architectures.

To the late Dr. Robert Orwoll, with whom I began this scientific journey so long ago. I hope that my work here has made the world a little better place to live.

ACKNOWLEDGEMENTS

I am in an immeasurable debt to my family, especially my parents Ken and Judy, my sisters Alicia and Megan, and all of my grandparents, for their love and support during this process and throughout my life. I am often unwilling or unable to express what I am feeling, but you have my gratitude for standing by me through the good and the bad. Cedar, we miss you dearly.

I would also like to thank my advisor Jim Cahoon for providing guidance and mentoring over my many years here. When I came to UNC, I didn't even know what a semiconductor was, and I have learned an immeasurable amount in that time. I would also like to thank him for putting up with my jokes and treating my opinions as worthwhile.

I would like to thank current and former members of the Cahoon lab, among whom I count many friends, for their help in the lab and outside of it, for teaching me and allowing me to teach, and for being with me there in the trenches.

I would also like to thank my friends and the good people at Habitat for Humanity of Orange County, for keeping me grounded and sane, and helping me to find a purpose even when my direction was unclear.

TABLE OF CONTENTS

LIST OF TABLES

LIST OF FIGURES

LIST OF ABBREVIATIONS

A	area
AAO	anodic aluminum oxide
AFM	atomic force micropscopy
B	radiative recombination coefficient
BHF	buffered hydrofluoric acid
B-DFM	back-scattering dark-field microscopy
CVD	chemical vapor deposition
C-WSM	coverslip waveguide scattering microscopy
DFM	dark-field microscopy
D_n	diffusion constant for electrons
D_p	diffusion constant for holes
$D_{p,n}$	diffusion constants for electrons and holes
D_{Π}	distribution of surface trap state energies
EBL	electron-beam lithography
EDS	energy-dispersive x-ray spectroscopy
EELS	electron energy loss spectroscopy
E_i	intrinsic Fermi level energy
ENGRAVE	Encoded Nanowire GRowth and Appearance through VLS and Etching
E_T	trap state energy
EQE	external quantum efficiency
FDFD	finite-difference frequency domain
FET	field-effect transistor
FF	fill factor
FIB	focused ion beam
F-DFM	forward-scattering dark-field microscopy
FWHM	full width at half maximum
I	current
I_L	light-generated current

I_o	dark saturation current
IPA	isopropyl alcohol
IQE	internal quantum efficiency
IR	infrared
I_{SC}	short-circuit current
I-V	current-voltage
J_{SC}	short-circuit current density
J_{SC}^{ideal}	ideal short-circuit current density
k_B	Boltzmann constant
LED	light-emitting diode
L_i	intrinsic segment length
L_n	electron effective diffusion length
$L_{n,p}$	electron and hole effective diffusion lengths
L_p	hole effective diffusion length
MFPL	mean-free path length
MIBK	methyl isobutyl ketone
MMA	methyl methacrylate
MOSFET	metal-oxide-semiconductor field effect transistor
n	electron concentration
n	ideality factor
$N_{A,D}$	doping level
n_D	electron concentration in the depletion region
n_i	intrinsic carrier concentration
NP	nanoparticle
NPGS	Nanometer Pattern Generation System
NR	nanorod
NW	nanowire
p	hole concentration
p_D	hole concentration in the depletion region

Φ_{IQE}	spatially-dependent internal quantum efficiency
P_{max}	maximum power
PML	perfectly matched layer
PMMA	poly(methyl methacrylate)
PV	photovoltaic
QD	quantum dot
R	nanowire radius
R_D	recombination rate in the depletion region
R_S	surface recombination rate
R_{Series}	series resistance
R_{SH}	shunt resistance
R_{SRH}	Shockley-Read-Hall recombination rate
S	surface recombination velocity
sccm	standard cubic centimeters per minute
SEM	scanning electron microscope
S_n	electron surface recombination velocity
S_p	hole surface recombination velocity
SRH	Shockley-Read-Hall
SRV	surface recombination velocity
STEM	scanning transmission electron microscope
s-SNOM	scattering-scanning near-field optical microscopy
S-WSM	substrate waveguide scattering microscopy
T	temperature
TE	transverse electric
TEM	transmission electron microscope
TIRFM	total internal reflection fluorescence microscopy
TIRM	total internal reflection microscopy
TM	transverse magnetic
τ	electron and hole recombination time

τ_{SRH}	Shockley-Read-Hall recombination time
$\tau_{SRH,n}$	electron Shockley-Read-Hall recombination time
$\tau_{SRH,p}$	hole Shockley-Read-Hall recombination time
UV	ultraviolet
V	voltage
V_{OC}	open-circuit voltage
$\tilde{V}_{OC}$	normalized open-circuit voltage
VLS	vapor-liquid-solid
VS	vapor-solid
VSS	vapor-solid-solid
WSM	waveguide scattering microscopy
W_D	depletion width
WZ	wurtzite
XPS	x-ray photoelectron spectroscopy
ZB	zincblende

INTRODUCTION

"Happy the Man, who, studying Nature's Laws, Thro' known Effects can trace the secret Cause"

- John Dryden, *The Works of Virgil*

1.1 Semiconductor Properties

Semiconducting materials form the basis for most modern electronic devices, largely due to the ways in which they can be modified. Semiconductor doping allows for modification of the material's electronic properties, changing its carrier density, disrupting the balance between electrons and holes, and even inverting the response of its conductivity to changes in temperature. The ability to spatially modulate dopant concentration and type within a semiconductor structure enables the creation of electrostatic junctions, which underlie computer circuits and photovoltaics. Improving device quality and performance requires ever more precise modulation of this dopant concentration, down to the nanometer scale. To move beyond the limitations of bulk devices, we need to take advantage of new properties, such as those that emerge on the nanometer scale. At this length scale, for example, light behaves as a wave, and thus the optical properties of a material are not solely limited by its composition, but can be modified by its size and shape. While conventional device production processes, such as lithography and diffusion doping, can achieve micrometer scale resolution, pushing these techniques to the nano scale is fundamentally challenging. As an alternative to this "top-down" approach, the "bottom-up" synthesis of nanomaterials through chemical processes offers an opportunity to control material composition and geometry on a much shorter length scale. Achieving the necessary level of compositional and geometrical control, however requires an in-depth understanding of the chemical processes affecting the production of nanomaterials.

Portions of this chapter reproduced from Hill, D. J.; Cahoon, J. F. Nanowire Synthesis: From Top-Down to Bottom-Up. *Material Matters* **2017**, *12.1*. Copyright 2017 Merck KGaA.

1.1.1 Semiconductor Doping

Semiconductors have a resistivity (ρ) between that of insulators and conductors, in the range of $\sim 10^6 - 10^{-3}\ \Omega$ - cm, and an intrinsic carrier density (n_i) from $\sim 10^6 - 10^{13}\ cm^{-3}$. Semiconductors at equilibrium conform to the equation [1]

$$n \cdot p = n_i^2 \tag{1.1}$$

where n and p are the electron and hole concentrations, respectively, and n_i is the material's intrinsic carrier concentration. In an intrinsic semiconductor, the electron and hole concentrations are equal. By introducing an impurity that can accept or donate an electron to the crystal lattice, an excess of electrons (n-type) or holes (p-type) can be produced. In silicon (Si) common n-type dopants include phosphorus (P), arsenic (As), and antimony (Sb), while common p-type dopants include boron (B), aluminum (Al), and gallium (Ga). As Si is a Group IV material containing 4 valence electrons, each Group V atom will donate one extra electron and each Group III atom will accept an electron (producing a hole), if electrically active within the crystal lattice. The introduction of these carriers increases the conductivity of the material as the carrier density increases towards $\sim 10^{18}\ cm^{-3}$. Above this level, the semiconductor is considered degenerately doped. As the carrier concentration increases, the material begins to behave more like a metal, wherein the conductivity decreases with increasing temperature, and the dopants may reach a sufficient density to produce additional bands within the band gap of the semiconductor.

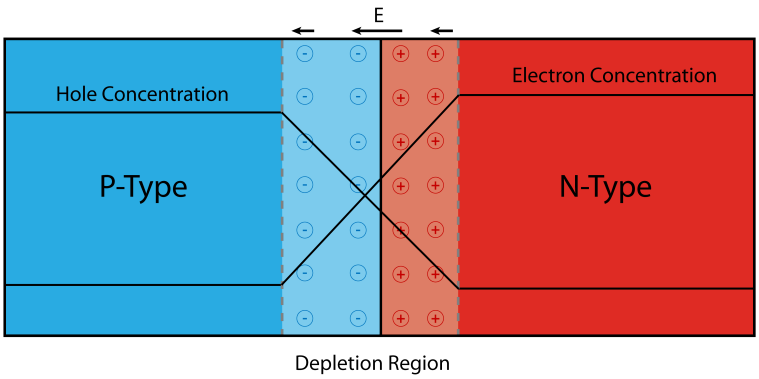

Figure 1.1: P-N junction. Schematic of a p-n junction at equilibrium, showing the electron and hole concentrations, and fixed charges in the depletion region, which produce an electric field.

When regions of different doping levels or doping types are placed in contact with one another, there is a concentration gradient of electrons and holes. Free carriers will migrate to mitigate this concentration gradient, leaving behind fixed charges. These fixed charges will produce a potential across the depletion region in proportion to the natural logarithm of the number of charges that were depleted. The width of this depletion region is inversely proportional to the carrier concentration. This p-n junction, shown in Figure 1.1, is a versatile component, which can separate charges and grow or shrink in response to an external field. A similar junction may also be formed at the intersection of two different semiconductor materials, depending on the alignment of the bands. The depletion width can also be expanded by introducing an intrinsic, or undoped, section between the p-type and n-type regions to produce a p-i-n junction.

1.1.2 Semiconductors and Light

Semiconductor materials also exhibit an electronic band gap, generally in the range of $0.1 - 4\,eV$, and the Fermi level lies within the band gap, such that carriers can be excited from the valence band into the conduction band, given sufficient energy. As a result, semiconductors can absorb light with a photon energy that exceeds the band gap. Upon excitation, semiconductors will excite an electron to the conduction band and leave a hole in the valence band. These carriers then subsequently relax to the band edge. Left unperturbed, the electron and hole will recombine, via either band-to-band recombination or through trap-state assisted recombination, to produce a photon (radiative) or a phonon (non-radiative). For most semiconductors, the relevant wavelength range is between the mid-IR and UV. The absorptivity of these materials is in part determined by whether the band gap is direct or indirect. In direct band gap materials, like CdS and GaP, absorption is very efficient, and light may be absorbed in < 1 μm. In contrast, absorption in indirect bad gap materials requires the aid of a phonon, reducing absorption probability and increasing light penetration lengths to $>$100 μm. The emission of light, as the reverse process of absorption, follows a similar set of rules: emission in direct band gap materials is probable, while emission in indirect band gap materials is improbable.[2]

1.2 Semiconductor Applications

1.2.1 Photovoltaics and Photodetectors

As a result of the ability absorb light and produce electrostatic junctions, semiconductors are well suited to to the conversion of light into electricity. If photogenerated electrons and holes are produced within the depletion region of a p-n or p-i-n junction, the electric field present will separate the charges, pulling holes towards the p-type side and electrons towards the n-type side. These charges can then be passed to an external circuit to perform work. When analyzing photovolatic performance, there are several factors to consider. The first is the short circuit current (I_{SC}). This value reflects the maximum current that can be extracted without an external bias. This value is primarily governed by the physical size, absorptivity, and charge carrier collection probability of the device. To account for the physical size, this value is often expressed as a short circuit current density (J_{SC}, in mA/cm^2). The second is the open circuit voltage (V_{OC}), or the maximum voltage that the cell can produce. The V_{OC} is largely determined by the magnitude of recombination within the device and the band gap of the material. The third primary value by which solar cells are characterized is the fill factor (FF). This is the ratio of the maximum power that the device can produce (P_{max}) to the product of the (I_{SC}) and (V_{OC}), reflecting the overall quality of the device, and factors into cell efficiency. The ideal diode conforms to the equation[1]

$$I = I_o(e^{\frac{qV}{k_BT}} - 1) - I_L \tag{1.2}$$

where I_L is the photogenerated current and I_o is the dark saturation current, reflecting the number of thermally generated charge carriers. However, real devices deviate from ideal behavior. Several additional factors can be implemented to reflect this behavior in the modified diode equation:

$$I = I_0(e^{\frac{q(V+IR_{Series})}{nk_BT}} - 1) + \frac{V + IR_{Series}}{R_{SH}} - I_L \tag{1.3}$$

where *n* is the ideality factor, reflecting the type of recombination, R_{Series} is the series resistance across the diode, and R_{SH} is the shunt resistance, or resistance to an alternate current pathway. Depending on the quality of the device, one or more of these factors may be considered insignificant, or additional complexity, like the double-diode model, may be added. A graphical representation of these factors can bee seen in Figure 1.2.

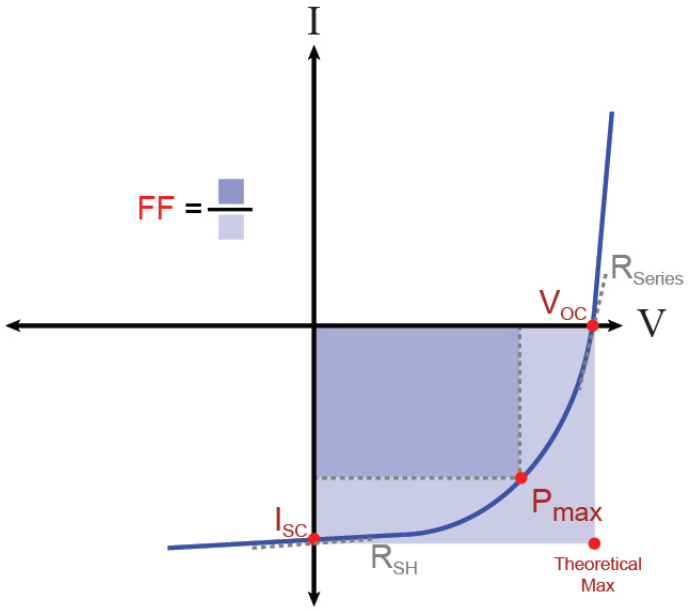

Figure 1.2: Solar cell *I-V* characterization. The typical characteristics of a solar cell under illumination are illustrated, included the short circuit current (I_{SC}), open circuit voltage (V_{OC}), maximum power point (P_{max}), fill factor (FF), series resistance (R_{Series}), and shunt resistance (R_{SH}).

When operated in the forward bias regime, the diode acts a photovoltaic, converting optical power into electrical power. In the reverse bias regime, the diode can operate as a photodetector, using the input electrical power to increase its sensitivity to incoming photons.

1.2.2 Light Emitting Diodes

As absorption and emission are reverse processes, light emitting diodes (LEDs) are constructed in much the same way as a photovoltaic cell, with p-type and n-type regions in contact with one another. Operated in forward bias, electrons and holes are sent towards one another to promote recombination. In direct band gap materials, this recombination will often be radiative. Currently, light emitting diodes are not produced from indirect band gap materials like Si because the probability of radiative recombination is too low. Instead they are produced from binary or ternary III-V compounds, such as $Al_xGa_{1-x}As$ (infrared), $GaAs_{1-x}P_x$ (red), GaP (green), and $In_xGa_{1-x}N$ (blue), wherein composition, doping, and heterostructure formation may be used to tune the emission wavelength.[2]

1.2.3 Computation

In addition to controlling light, semiconductors are also important in controlling the flow of electricity. The ability to switch the flow of electricity on or off using an orthogonal electrical signal provides the basis for creating a Boolean logic circuit. In particular, the formation of a NAND gate permits the formation of all other Boolean logical elements. Modern electronics use a field-effect transistor (FET), specifically a metal-oxide-semiconductor FET (MOSFET), in which the application of an electric field can be used to modulate conduction. MOSFETs can be constructed in either "enhancement-mode" or "depletion-mode" configurations, but both rely on the formation of a *p-n* junction. In the enhancement mode configuration, the source and drain are both of the same doping type (either n-type, forming an n-MOSFET or p-type, forming a p-MOSFET) and the channel between them is doped the opposite type. A dielectric gate is formed above the channel and serves to separate the channel from the gate electrode. As a gate bias is applied to the channel (positive for n-MOSFETs, negative for p-MOSFETs), minority carriers are drawn to the channel-dielectric interface and form a conductive channel between the source and drain. Enhancement mode transistors are thus "off" by default, and require a gate bias to conduct. Depletion mode devices are constructed similarly, except that the channel is of the same doping type as the source and drain, though more lightly doped, and the entire structure is formed on an oppositely doped substrate. When a bias is applied to the gate electrode (negative for n-MOSFETs, positive for p-MOSFETs), the channel is depleted of its majority carriers, preventing conduction between the source and drain. Depletion mode devices are thus "on" by default. Other types of transistors, such as bipolar transistors and tunnel-effect transistors may also be formed in semiconductor architectures. The formation of all types of semiconductor transistors, however, requires the ability to control the type, quantity, and spatial distribution of dopants within the semiconductor device.[2]

1.3 Nanomaterials

1.3.1 Optical Properties of Nanomaterials

While in the bulk, device properties are limited by composition and material properties. At the nano scale, however, material properties alone no longer dictate behavior. The most common example of this phenomenon is quantum-confined materials. When semiconductor materials, such as CdS, PbSe, and Si,

are reduced to length scales below the Bohr radius of the electron (typically in the range of 1-10 nm), the energy bands of the semiconductor are discretized, and the position and spacing of these energy levels then depends on the size of the nanoparticle.[3] This results from the wave-like properties of the electron interacting with the limited spatial extent of the semiconductor particle, as in the "Particle in a Box" quantum model. Similarly, in metallic systems, the collective oscillation of electrons that is produced under illumination (plasmon) can be spatially confined in nanomaterials (typically $<$100 nm), producing an optical absorption profile which depends on the size and shape of the metal nanoparticle.[4]

At slightly larger length scales ($\sim$50-300 nm), as the nanoparticle size approaches the wavelength of light in the medium (λ_o/n), optical properties become dictated by Mie theory,[5] where the size and shape of a nanoparticle alters its interaction with an incident field. This results in absorption and scattering profiles that differ from the bulk material, causing, for example, clouds to be white instead of clear, despite being composed of water. In the case of engineered nanomaterials, scattering and absorption can be easily modulated, as the electric field within the nanoparticle is dictated by the resonant modes of the structure, such as dipole, whispering-gallery, and guided modes.

1.3.2 Electronic Properties of Nanomaterials

In addition to the modulation of the optical properties of materials, the size reduction of bulk materials can also impact their electronic properties. Given the extremely high surface area-to-volume ratio of nanomaterials, the condition of the surface begins to play a significant role in dictating electronic behavior. In bulk materials, recombination between electrons and holes is typically described by three-dimensional bulk Shockley-Read-Hall mechanics (eq. 5.1). Yet in crystalline nanomaterials, the Shockley-Read-Hall lifetime may exceed the time it takes for a charge carrier to traverse the nanoparticle and interact with the surface. In this case, the recombination rate must be reformulated into a two-dimensional surface recombination (eq. 5.2). The extent to which surface recombination will dominate over bulk recombination will then depend on both crystal quality and nanoparticle diameter, leading to a complex relationship between total recombination rate and nanoparticle size.

1.3.3 Semiconductor Nanowires

Amongst nanomaterials, nanowires (NWs) offer a unique blend of nanoscale and bulk properties. Nanowires have diameters ranging from 1-500 nm, offering a platform for exploiting unique nanoscale

phenomena, but have aspect ratios greater than 1:100, extending geometries and charge transport to the micro or even macro scale. Nanomaterials must be able to interface with macroscopic devices to produce viable technologies, and nanowires fit many of the necessary criteria.

1.3.3.1 Nanowire Synthesis

As with most nanomaterials, the synthesis of nanowires can be approached using "top-down" or "bottom-up" techniques. Conventional top-down nanowire fabrication is a subtractive technique, like carving a statue from a block of marble, using chemicals rather than chisels to achieve nanoscale control. It utilizes many of the techniques employed by the semiconductor industry, such as lithography and chemical etching, to turn a bulk wafer or crystal into nanowire structures. In general, top-down fabrication relies on large, expensive, and precise instrumentation that can be found in clean room and nanofabrication facilities.

Top-Down Methods. Among the most popular top-down techniques for nanofabrication is lithography, which is used extensively in the microelectronics industry. This technique involves the deposition of a resist material, such as poly(methylmethacrylate) that will act like photographic film to produce a pattern after exposure and development using a patterned mask. The resolution of photolithography is limited by the lithographic technique and wavelength of light used, and it is often not suitable or practical for small nanowires. Patterns with higher resolution can be achieved with electron-beam lithography, which is a maskless direct-write exposure method. For the production of vertical nanowires, the pattern will consist of a series of circles or holes on top of a wafer of the target material. For horizontal nanowires, the pattern will be a series of lines or trenches on a layered substrate, such as silicon-on-insulator.

Nanowires can then be produced by etching the extraneous material from the wafer. Depending on the process, the resist may be used directly as the etch mask or may serve as the template for deposition of a more stable mask material, such as gold. Wet chemical etchants, like potassium hydroxide, or an electrochemical etchant can then be used to etch the pattern, as illustrated in Figure 1.3A. This technique often produces tapered rather than cylindrical wires due to etching underneath the mask. This problem can be minimized by the use of anisotropic etchants, but it is rarely completely eliminated.[6] One approach to achieving cylindrical vertical wires is to replace the wet chemical etch with a highly anisotropic deep reactive ion etch (DRIE), which can achieve vertical nanowires that are tens of microns

in length. Alternatively, the pattern can be inverted and metal-assisted etching used,[7] illustrated in Figure 1.3B, to achieve similar anisotropic structures.

Alternate approaches to conventional lithography promise higher resolution than can be achieved with optical lithography and higher throughput than is possible with conventional methods. Nanosphere lithography, for instance, involves the self-assembly of a monolayer of polystyrene nanospheres onto a substrate in a close-packed lattice.[8] These spheres serve as a mask for the deposition of a metal or other masking material and are subsequently removed after deposition. Nanoscale patterns also can be produced through mechanical transfer with nano-imprint lithography.[9] A high resolution master pattern is produced with a cost-intensive technique such as electron-beam lithography. This master is then pressed into the resist material to transfer the pattern.

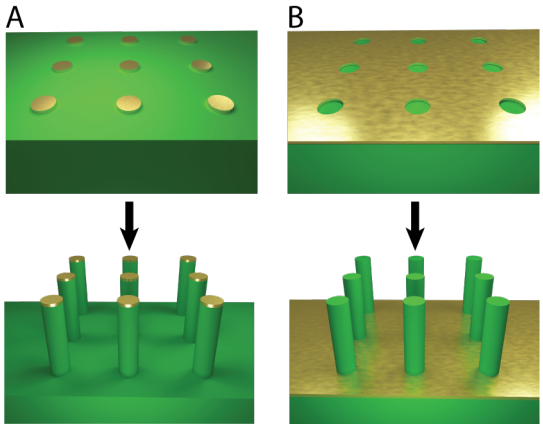

Figure 1.3: Top-down fabrication methods. A) Lithographic patterning of a metallic mask followed by anisotropic etching, such as DRIE. B) Lithographic patterning of exposed regions followed by anisotropic metal-assisted chemical etching.

Top-down nanowire fabrication is enticing due to the ease with which ordered arrays of nanowires can be constructed. This facilitates electrical contact to the nanowires and their integration into large-scale devices. Additionally, many of these processes are compatible with standard microelectronics industry processes, enabling their scale up.

Top-down fabrication does present several drawbacks. The applicability of photolithography to these processes diminishes as the desired length scales decrease, requiring the implementation of more advanced methods such as extreme ultraviolet lithography. Alternatives to photolithography, like electron-beam and scanning probe lithographies, are direct-write techniques, requiring slow serial writing of individual elements. Parallelization of these techniques will be necessary for industrial-scale production. Nanowires

formed by top-down processes also frequently lack complex electronic characteristics. When etched from a wafer, any desired modulation of composition must be encoded into the wafer by techniques like molecular beam epitaxy (MBE) or encoded after growth through implantation methods. This processing can greatly increase the material cost of nanowire devices compared to bottom up techniques.

Bottom-Up Methods. In contrast to top-down techniques, bottom-up processes are derived from a chemist's toolkit, where molecules are assembled piece-by-piece and scaled up to produce materials thousands of times larger than the average molecule. Bottom-up syntheses are additive, like the growth of a tree from a small seed, using chemistry to control structure.

The anisotropic growth of nanowires is frequently accomplished using nanoparticle catalysts and gas-phase precursors. One of the most common methods is vapor-liquid-solid (VLS) growth, wherein gaseous precursors of the desired nanowire material, such as SiH_4 for silicon, dissolve into a liquid-metal catalyst.[10] As the catalyst becomes supersaturated, the solid nanowire crystallizes from the liquid catalyst, as illustrated in Figure 1.4A. This synthesis involves a chemical vapor deposition (CVD) system, in which the temperature, pressure, and flow rates of precursors can be regulated. The conditions must be controlled to minimize non-catalytic growth of material on the side of the nanowire, which would disrupt the cylindrical geometry. Noble metal nanoparticles commonly serve as the initial seed for nanowire growth. For the VLS process, the metal must form a liquid droplet that serves as the catalyst. In many cases, this droplet forms a eutectic composition that melts at a lower temperature than the pure metal or semiconductor material. However, when synthesizing binary or ternary materials that contain a low melting metal, such as Ga in GaAs, the VLS process can be self-catalyzed using a Ga liquid droplet that is continuously resupplied by a vapor-phase precursor such as trimethylgallium.

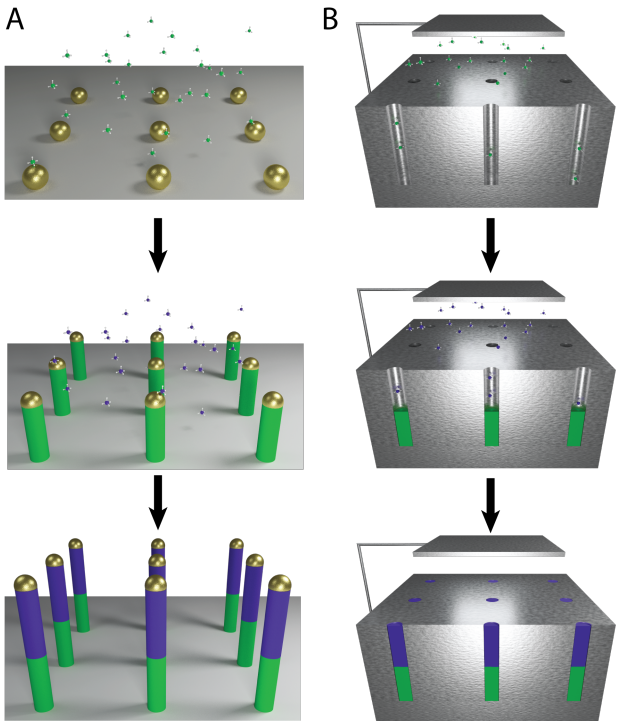

Figure 1.4: Bottom-up synthesis methods. A) Vapor-phase growth of segmented nanowires through the VLS process, with modulation of the gaseous precursor resulting in controlled compositional changes. B) Solution-phase growth of nanowires through electrochemical deposition into anodic aluminum oxide (AAO). A similar segmentation process is possible.

VLS processes are advantageous because they allow for compositional control. Dopant materials, such as phosphine for silicon, can be introduced and removed repeatedly throughout the nanowire growth, producing superlattice structures with modulated electronic properties.[11] Similarly, changing the ratio of the components in a ternary structure, like $GaAs_xP_{1-x}$, can produce nanometer-scale band gap modulation[12] and quantum well structures.

Although metal catalysts are commonly dispersed on a solid substrate, a variant called aerotaxy utilizes catalysts suspended in the reactor to achieve high growth rates.[13] A lower temperature process, called vapor-solid-solid (VSS) growth, uses many of the same principles as VLS growth.[14] However, the catalysts are solid rather than liquid, altering the kinetic processes. Rather than dissolving and supersaturating in a liquid, the precursors diffuse through the interface between the catalyst and nanowire in order to add material. This slows down the growth process, allowing for more abrupt (to the atomic level) compositional changes in the nanowire.[15]

Contamination of the catalyst material in the nanowire can be disadvantageous for certain processes, so non-catalyzed syntheses have also been developed. Templated growth provides one pathway to achieve the anisotropy needed for nanowires. AAO, produced by electrochemical etching, contains a honeycomb of nanometer-scale channels, offering the geometry required for producing arrays of vertical nanowires. Conventional vapor deposition techniques (CVD, sputtering, etc.) can be used to fill these channels, producing nanowires when the template is removed. A patterned substrate can be used for selective area epitaxy, in which epitaxial growth occurs in exposed regions, but deposition onto the mask material does not occur.[16] The presence of screw dislocations has also been demonstrated as a mechanism to induce catalyst-free nanowire growth.[17]

Many of the techniques employed in the vapor phase have analogies in the liquid phase. The solution-liquid-solid mechanism is similar to that of VLS, except nanowire precursors are dissolved into a high-boiling liquid, such as squalane, and the catalysts are suspended therein.[18] AAO substrates can also be used for templated solution growth, using electrochemical deposition to fill the channels[19] as shown in Figure 1.4B. Drawing upon the solution-phase synthesis of nanoparticles, redox reactions can also be used to produce nanowires.[20] Seed particles are first grown by a rapid reduction of a dissolved precursor with a strong reducing agent like sodium borohydride. Secondary growth is achieved with a weaker reducing agent, like l-ascorbic acid, to prevent additional seed particle production. The nanowire anisotropy is achieved by controlling surface chemistry. The introduction of surfactants that selectively alter the surface energy of particular crystal facets, such as hexadecyltrimethylammonium bromide, directs growth along particular axes, producing nanowires.

Bottom-up synthesis provides the opportunity for explicit control of nanowire composition during growth, enabling the production of complex superlattice structures. This compositional control can be used to encode novel electronic properties such as quantum well photodiodes, as well as provide a template for subsequent processing. Selective etching of these superlattice structures has been shown to produce a wide variety of shapes and structures that can be used in photonics, electronics, and memory[21] (Figure 1.5).

The main challenge facing further development of technologies based on bottom-up nanowires involves their integration into large-scale devices. Wires grown in vertical arrays can be used in a similar fashion to those fabricated by top-down methods, but many growth processes instead produce disordered “forests” of nanowires or solutions of nanowires. Recent research efforts have focused on how

to assemble and organize the nanowires so they can be interfaced with conventional manufacturing steps. The incorporation of these techniques will prove essential to moving nanowires from the laboratory to the factory.

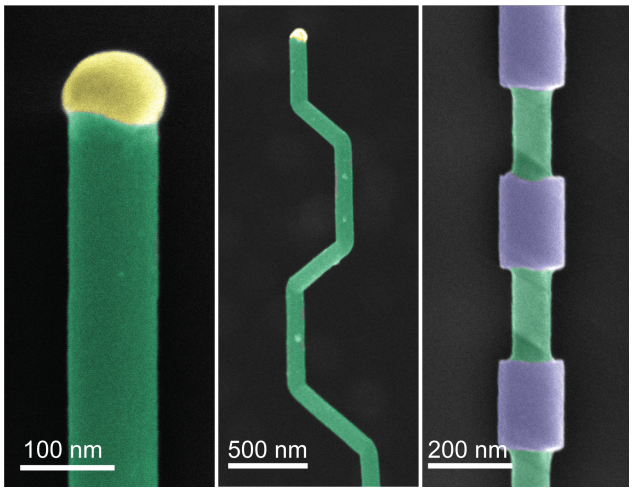

Figure 1.5: Nanowire structures. A) False-color SEM of a silicon nanowire grown by VLS (green) and the metal catalyst at the tip (yellow). B) False-color SEM of crystallographic kinking that can be accomplished by manipulating the reaction conditions. C) False-color SEM of morphology that can be achieved by modulating the composition during growth, followed by etching.

Compositional Modulation. The properties of nanowires derive primarily from the synthetic methods used to produce them. While top-down techniques allow for the rapid production of ordered arrays of nanowires, they often lack the complexity necessary for advanced applications. Bottom-up techniques, in contrast, provide the opportunity to control axial and radial composition, programming electronic and optical components into the NW structure. In III-V systems, the variety of interchangeable elements facilitates the production of compositional hetereojunctions,[22,23] which contain localized electric fields. Furthermore, as each semiconductor stoichiometry has a different band gap,[24] NWs containing spatially dependent band structures can be created by altering the ratio of the gaseous precursors as the NW growth progresses. III-V systems also show controllable crystal phase modulation, switching between wurtzite and zincblende structures to create atomic-level interfaces.[25]

In both III-V and group IV systems, electronic properties can also be changed by doping, adding impurities in concentrations far below stoichiometric ratios ($<1\%$) to alter the Fermi level within the semiconductor. For silicon, this process has been studied extensively as a result of the reliance on doped silicon interfaces in the commercial semiconductor industry. Group III elements, such as boron, aluminum,

and gallium, are used as p-type Si dopants, while group V elements, such as phosphorus, arsenic, and antimony, are used as n-type dopants. Solubility and diffusivity vary between these elements,[26] making them suitable for different applications. With bottom-up techniques, the presence and quantity of these dopants can be modulated during NW growth, producing abrupt or graded homojunctions. When produced by the VLS mechanism, the potential abruptness of the junction is limited by the reservoir effect.[27] As dopants are introduced to the NW via the liquid catalyst, the catalyst can serve as a reservoir of dopant atoms, continuing to supply them to the NW after the gaseous precursor is removed. Abrupt junctions require the dopants to have an alternate mechanism by which to leave the catalyst, such as evaporation.[28] In template-assisted methods, such as On-Wire Lithography[19] and Coaxial Lithography,[29] electro-deposition permits the formation of junctions between very different materials, such as semiconductors, metals, and polymers, at the expense of the crystallinity of the structure. Template-assisted selective epitaxy, however, maintains crystal quality, but has so far only been demonstrated for semiconductor junctions.[30]

Separate from or in addition to axial modulation, composition can also be controlled along the NW radius. Axial growth is first terminated by altering the reaction conditions, and radial growth is started, typically by the VS mechanism,[12,31] in which precursors decompose non-selectively on the NW surface. The absence of a catalyst in the VS mechanism removes several of the limitations of the VLS mechanism, allowing for more abrupt interfaces and higher active doping levels in radial junctions.

Diameter Modulation. While dopant modulation can produce complex electronic structures, the NW nevertheless remains a cylinder, unable to access many of the unique optical phenomena of nanostructures. In order to create localized optical states along the nanowire, we must be able to axially modulate diameter in the same way that we can modulate dopants. Several processes are available for selective shell growth on NWs, including plateau-Raleigh instability[32] and control of the VS process through surface chemistry.[33] However, these techniques are unable to match the spatial resolution of dopant profiles produced by VLS growth. The simplest way to match this spatial resolution is to use the doping profile itself as a template for diameter modulation. It has long been known that the etch rate of silicon in basic solutions strongly depends on doping level, with a dramatic slowdown in etch rate at degenerate doping levels. The ENGRAVE (Encoded Nanowire GRowth and Appearance through VLS and Etching) process[21] takes advantage of this phenomenon to precisely control diameter via the dopant profile.

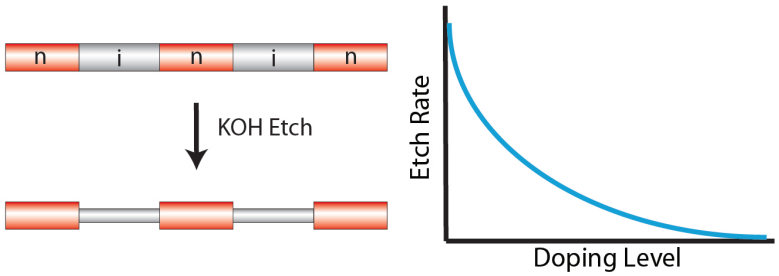

Figure 1.6: ENGRAVE Process. Schematic illustration of the ENGRAVE process. Dopant modulation is achieved during VLS growth, and the structure is subsequently etched in KOH. The diameter can be tuned precisely due to the relationship between doping level and etch rate.

1.3.3.2 Non-Equilibrium Processes

Bulk crystal properties limit the equilibrium concentration of dopant atoms in silicon.[34] Higher active doping levels can be achieved in conventional processes through high temperature annealing, where the solid solubility limit is much higher, and subsequent rapid cooling traps dopants at a level above the room temperature solid solubility. This process, however, also results in dopant diffusion, negating any dopant abruptness present within the structure. Alternate methods of increasing doping levels require dopant incorporation through non-equilibrium processes.

Ion implantation, followed by pulsed laser annealing,[35,36] can introduce non-equilibrium quantities of dopants in selective locations. The high energy of ion implantation can force dopant atoms into a substrate at quantities well above the solid solubility limit (hyper doping), but these dopants are often not electronically active. A subsequent annealing step is required to incorporate the dopants into the crystal lattice. Flash-lamp annealing can be used to rapidly heat and cool the entire substrate. Rather than expose the entire structure to high temperatures, pulsed laser annealing produces local temperatures that can exceed the melting point of the crystal. Removal of the laser then results in a rapid recrystallization, which traps dopants within the lattice. While this process has been demonstrated in NWs,[37,38] this technique requires lithographic masking and precise laser optics to produce spatially modulated dopant profiles, and may affect the crystal quality of the substrate.

For NWs, optimal hyper doping would occur during the NW growth process itself. NWs grown through the VLS process are not subject to an equilibrium crystal growth process, as would be typical of epitaxial crystal growth, as a result of the liquid catalyst-solid NW interface. Instead, the crystallization is dictated by the kinetics of solidification at that interface. The growth of Si NWs by VLS has been

proposed to follow Si-Si dimer bilayer step-flow kinetics which propagate from step edges.[39] Ultimately, this process differs from bulk systems due to the high surface area to volume ratio, which results in a much higher concentration of step edges. These locations pin dopant equilibration processes and effectively freeze dopants within each deposited bilayer.[40]. This processes has been demonstrated to introduce extremely high levels of Al, In, and Sn atoms into the silicon lattice when used as catalyst materials.[40,41] What remains, however, is to demonstrate this processes in extrinsic, gas-phase dopants, which can be modulated on and off. This process is only possible when the ratio of dopant atoms to NW precursor atoms within the catalyst far exceeds the solid solubility of the dopant atom in the NW crystal.

1.3.3.3 Nanowire Photonics

In contrast to their electrical properties, the optical properties of NWs are relatively insensitive to the doping level/profile. Rather than being dictated by material composition, optical properties of these structures are dictated primarily by geometry.[42,43] As the NW diameter is similar to or smaller than the wavelength of visible light, Mie scattering dominates optical behavior.[44] As Mie scattering depends primarily on diameter, it has been shown that the scattering color of a NW can be tuned throughout the visible spectrum by altering the NW diameter.[45] Under unpolarized illumination, NWs exhibit complex scattering spectra, resulting from a series of transverse magnetic (TM) and transverse electric (TE) modes. Furthermore, when illumination is not normal to the NW axis, there is a mixing between the Mie resonances of the diameter and the leaky/guided modes of the cylinder.[46] Full exploitation of these scattering resonances requires a much more controlled illumination geometry.

While scattering is the dominant observable of the light-matter interaction, NW absorption is also strongly affected by diameter.[47] This results from the optical resonances with the NW, such as dipole and whispering gallery modes. Depending on the crystal direction of the NW, the cross section of the NW is not always circular: it may also be square, triangular, or hexagonal. A combination of the nanowire size and the exact geometry of the cross section influences which modes are present, their strengths, and at what wavelengths they appear.[48] Thus, control over the NW geometry plays a fundamental role in dictating their optical properties.

In addition to the geometry of the semiconductor, the local environment also has a strong effect on NW optical properties. As subwavelength objects, NWs exhibit the “antenna effect”, wherein the NW interacts with light over an area larger than its physical cross section. The presence of a dielectric shell

on the nanowire has been shown to greatly increase the strength of this interaction, simultaneously - and somewhat paradoxically - increasing both scattering and absorption.[49] This phenomenon can only appear in deeply subwavelength structures: in bulk systems, an increase in scattering results in a commensurate decrease in absorption. When placed in close proximity to one another, NWs can couple together, with an energy exchange between the leaky modes of the individual NWs.[50] This coupling can also be used to modify the lasing properties of direct band gap NWs.[51] Numerous reports have explored nanowire arrays, using regularly sized and spaced vertical nanowires to produce photonic metamaterials. Well separated nanowires of a fixed diameter in an array produce structural color that derives from the photonic modes of the individual NWs.[52] As the NWs are placed closer together (spacing $<\lambda$), the array takes on the properties of a photonic crystal, in which the periodicity of the elements in the array dictate its photonic properties.[53,54] Bulk materials can also alter NW resonances, through either a change in the local refractive index or by producing interference effects. Coupling a NW to a resonant cavity has been demonstrated as an optomechanical resonator with a sensitivity approaching 1 fm/Hz$^{1/2}$.[55]

1.3.3.4 Nanowire Photovoltaics

Without an electronic backbone, however, many of these photonic structures remain passive, unable to integrate with conventional electronics. The simplest architecture used to created optoelectronic devices is the *p-n* or *p-i-n* junction. In NWs, this basic device element has been used to produce solar cells,[31,56–62] photodetectors,[63–65], and LEDs.[66,67] Several NW solar cells have reported record efficiencies resulting from photonic effects.[58,62] Specifically, the antenna effect acts as a localized solar concentrator, resulting in much more light absorption for a given amount of semiconductor that would be possible in a bulk configuration. Furthermore, the NW geometry relaxes many of the strain and dopant profile limitations of bulk devices, permitting the formation of complex heterostructures[66] and tandem cells.[57] The performance of these devices, however, is largely determined by the dopant profile and surface quality.

To characterize dopant distributions, a number of destructive and non-destructive techniques have been employed. Among the most sensitive is atom-probe tomography, which utilizes an ion beam to deconstruct the NW layer by layer and reconstruct an atomic profile through secondary ion mass spectrometry.[68,69] Less destructively, but with a lower sensitivity, TEM-based energy-dispersive x-ray spectroscopy[28,70] can also be used to map local elemental composition, albeit with the except of low x-ray

yield elements, like boron. These techniques, however, probe only the chemical composition. They cannot differentiate inactive, interstitial components from active, substitutional components. Stoichiometric changes along the NW axis can be imaged in direct band gap materials using photoluminescence and cathodoluminescence maps,[71] as changes in composition often result in a change in the band gap. Direct measurements of electronic properties typically utilize a localized nanoscale probe. Scanning photocurrent microscopy and electron beam-induced current mapping both measure electrical current as a function of localized excitation position,[71] which can be deconvoluted to determine field strengths and charge carrier diffusion lengths. Electron holography has been used in NWs to map out potential changes and space charge regions along the NW axis.[72,73] This has been correlated with electrical measurements to probe the effective electrical abruptness of a NW junction.

Atomic force microscopy-based techniques provide very localized probes of electronic structure. Kelvin probe force microscopy can detect localized electric fields, and thus map potential changes in the NW.[27,74–76] When combined with electrostatic simulations and electrical measurements, this technique can probe dopant transition widths, compensation doping, and core-shell screening effects. Scattering-scanning near field microscopy (s-SNOM) can measure local electric fields in addition to free-carrier terahertz absorption, mapping out doping profiles that exceed 10^{18} cm^{-3}.[77] This technique has been shown to be capable of differentiating between varying carrier levels within the degenerate doping regime as well as measure the effective electrostatic length of a doped NW segment, which may be shorter or longer than the physical dopant profile as a result of the strength and direction of the electric field.

It has been shown experimentally that surface modifications can drastically alter device performance.[59,78–82] As a result, previous theoretical analyses of NW behavior have focused primarily on the effects of crystal quality on device performance, as given by the bulk (SRH) and surface recombination rates. Overall, a reduction in recombination results in an increase in device parameters, such as short circuit current (I_{SC}) and open-circuit voltage (V_{OC}).[83] However, when the bulk recombination rate is high, the surface recombination rate has little effect on device performance, as the charge carrier diffusion length is limited by bulk recombination kinetics. Similarly, when the surface recombination rate is high, improvements in the bulk recombination rate produce little improvement in device performance. Device performance, then, is largely determined by the charge carrier diffusion length, which can be limited by multiple recombination methods.[84]

Though recombination may place an upper bound on device performance, it is not the sole determinant. It has been shown that in some cases, low values of the surface recombination velocity (up to $\sim 10^3$ cm/s) have a negligible effect on device performance.[85,86] Examining the internal quantum efficiency (IQE), it can been seen that IQE within the intrinsic region can remain at $\sim$100% even after the introduction of surface recombination.[84] When combined with the observation that increases in p- and n-type doping levels can result in an increase V_{OC},[87] it becomes clear that the electric field distribution within the structure can mitigate the effect of surface recombination. As the electric field is determined both by doping level and geometry,[88] an analysis of the effect of intrinsic length on recombination will prove important for understanding device behavior.

When vertically oriented, the spatial distribution of scattering and guided modes also plays a role in performance. In this case, the local carrier collection rate is the product of the carrier collection probability, as determined by electrostatic simulations, and the carrier generation rate, as determined from optical simulations.[89] The NWs shown herein experience uniform illumination along their axes, and as a result, the spatial carrier generation distribution can largely be neglected. Instead, we will explore the interplay between surface recombination and diode geometry in dictating device parameters.

METHODS

"The scientist is not a person who gives the right answers, he's one who asks the right questions."

- Claude Lévi-Strauss, *Mythologiques*

2.1 Nanowire Growth

NWs were produced in a home-built, hot-wall chemical vapor deposition (CVD) system. The system is constructed primarily of 304L stainless steel tubing joined by ConFlat fittings (Kurt J. Lesker) or welds. A vacuum with a base pressure of $\sim 3x10^{-3}$ Torr is achieved using a SDE120TX-45 dry screw pump (Kashiyama). Gas flows are controlled with fast-responding mass-flow controllers (MKS Instruments P4B). The total pressure is regulated with a 148-J needle valve (MKS Instruments) and monitored with Baratron Capacitance Manometers (MKS Instruments). The reaction occurs within a one inch fused-quartz tube (Chemglass Life Sciences) mounted via Ultra-Torr fittings (Swagelock) and heated with a single-zone Lindberg Blue M one inch diameter tube furnace (Thermo Scientific). All reaction parameters are controlled and monitored with a LabView program that provides automated temperature, pressure, and gas flow controls. All reactions were performed using Au NPs dispersed on Si-SiO_2 substrates. Prior to any reactions, the quartz tube is heated to 950 °C for 1 hour with an Ar flow of 20 sccm to remove any contaminants, then cooled below the growth temperature. Prior to reactions at 510 °C or 650 °C, the tube was first heated to 600 °C, and each dopant gas was briefly pulsed to remove excess pressure from the line before being heated to 950 °C.

2.1.1 Substrate Preparation

The growth substrate began as a 380 μm thick silicon wafer with 600 nm of wet thermal oxide (University Wafer). The wafer was cut into sections $\sim$ 2 cm x 1 cm. These sections were sonicated in acetone, then rinsed with acetone and isopropyl alcohol (IPA) and dried with nitrogen. The substrate was

then inserted into a UV-Ozone cleaner (Samco UV-1) for 100 s at 150 °C. The substrate was then covered in poly-L-lysine (0.1% w/v in water) for 4 minutes. The substrate was rinsed with nanopure water (Barnstead Nanopure; 18 $M\Omega \cdot cm$) and dried with nitrogen. Au nanoparticles (NPs) (BBI International; citrate stabilized) of diameters 50-200 nm are diluted in nanopure water at a ratio of 1:2 and dispersed onto the substrate for 4 minutes. The substrate was then washed with nanopure water and dried with nitrogen, and placed in the UV-Ozone cleaner for 5 minutes at 150 °C. The substrate is then inserted into the fused quartz tube and evacuated to $\sim 3x10^{-3}$ Torr while purging with Ar.

2.1.2 420°C Conditions

For n-type/intrinsic NWs grown at 420 °C, NWs are first nucleated between 440 °C and 450 °C at a pressure between 20 and 40 Torr. H_2 (Matheson Tri-Gas; 5N semiconductor grade) was used as a carrier gas, with flows between 60 and 200 sccm. SiH_4 (Voltaix) was used as the primary reactant gas, at a flow rate of 2 sccm. After 20 to 30 minutes, the temperature was ramped down to 420 °C at a rate of ∼1 °C per minute to minimize radial VS growth. Optionally, PH_3 (Voltaix; 1000 ppm in H_2) may also be introduced as a dopant, between flows of 0.15 and 20 sccm. The dopant flow can be rapidly modulated on time scales less than 1 second to produce precise dopant profiles. Under these conditions, with a silane partial pressure of ∼400 mTorr, the NW growth rate is ∼200 nm/min.

2.1.3 510°C Conditions

For p-type/n-type/intrinsic NWs grown at 510 °C, HCl (Matheson TriGas, 5N) was used to prevent VS deposition. Reactions were carried out at a total pressure of 20 Torr and a HCl:SiH_4 ratio of 2, unless otherwise noted, with a variety of flow conditions. In addition to PH_3, B_2H_6 (Voltaix; 1000 ppm in H_2) could be introduced as a dopant to produce p-type segments. NWs for four-point probe measurements were grown with 0.5 sccm SiH_4, 1 sccm HCl, and 180 sccm of H_2 carrier gas. NWs with a p-n superlattice were grown with 1 sccm SiH_4, 2 sccm HCl, and 90 sccm of H_2 carrier gas. In p-type segments, B_2H_6 flow was varied from 0-20 sccm to encode various doping levels, while n-type segments were grown with 20 sccm PH_3. The flow of H_2 carrier gas was varied between 180-200 sccm, depending on the dopant gas flow, to maintain a constant SiH_4 partial pressure of ∼ 200 mTorr. This yields a growth rate of 1.6 nm/(min·mTorr SiH_4) for p-type segments, 1.5 nm/(min·mTorr SiH_4) for intrinsic segments, and 1.4 nm/(min·mTorr SiH_4) for n-type segments.

2.1.4 650°C Conditions

All reactions at 650 °C were carried out at a total pressure of 20 Torr, with 0.5 sccm SiH_4 and 3.2-3.6 sccm HCl, except where the HCl flow was varied. The flow of H_2 carrier gas was varied between 180-200 sccm, depending on the dopant gas flow, to maintain a constant SiH_4 partial pressure of $\sim$50 mTorr. In p-type segments, B_2H_6 flow was varied from 0-20 sccm to encode various doping levels, while n-type segments were grown with 20 sccm PH_3. This yields a growth rate of 13 nm/(min·mTorr SiH_4) for p-type segments and 9 nm/(min·mTorr SiH_4) for intrinsic segments.

2.2 Nanowire Etching

Prior to wet-chemical etching, NWs were transferred onto silicon wafers coated with 100 nm of wet thermal oxide and 200 nm of low-pressure CVD Si_3N_4, which serves as an etch-resistant dielectric layer. NWs could be transferred mechanically, or by sonication in IPA and subsequent drop casting. The native oxide was first removed from the NWs by immersing the nitride substrate in a 20% solution of buffered hydrofluoric acid (Transene; BHF Improved) for 10 seconds and subsequently rinsing in nanopure water twice for 10 seconds each. When removing surface Au, the substrate was then immersed in IPA before being blown dry with nitrogen. The substrate was then immersed in a Au-etching solution of 4:1:40 (w/w/w) KI:I_2:H_2O for 30-60 s, rinsed twice with nanopure water, and then rinsed with IPA before being blown dry. If the Au etch was performed, the BHF etching process was repeated. The substrate was then placed in IPA that was equilibrated to the Si etch temperature (either room temperature or 40 °C) for 30 s. The substrate was then placed in the silicon etch solution, which consisted of 20% (w/w) potassium hydroxide (KOH; Fischer Scientific) in water capped with a layer of IPA, for a specified time, ranging from 10 s to 2 min, at either room temperature or 40 °C. The substrate was then placed in a 2% (v/v) solution of acetic acid in water to quench the etch. The substrate was subsequently washed in nanopure water and IPA before being blown dry. At high n-type doping levels, the repeated BHF-Au etch process may cause etching of the n-type section. In cases where the Au is still preventing proper etching, a short thermal oxidation followed by BHF etching will remove surface gold without introducing the Au etching solution.

2.3 Imaging

Scanning electron microscopy (SEM) was performed with an FEI Helios 600 Nanolab Dual Beam system with an imaging resolution of $<$5 nm using a typical acceleration voltage of 5 kV and imaging current of 86 pA.

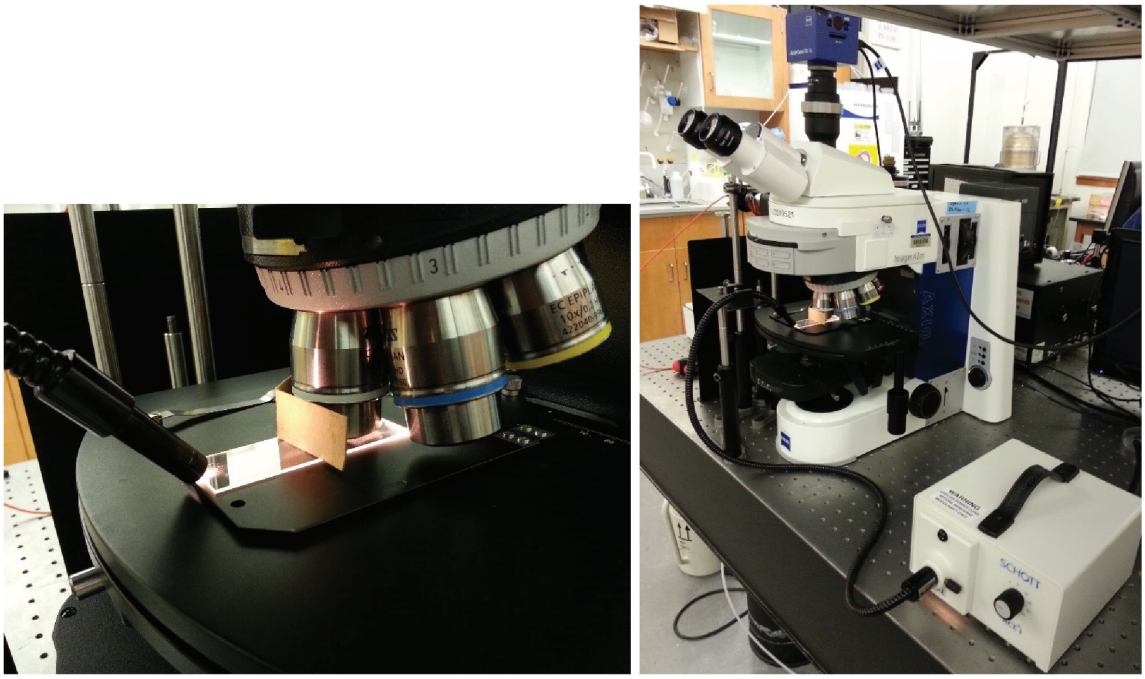

Figure 2.1: Waveguide scattering microscopy experimental setup. Images of the setup used for S-WSM. A transparent substrate is placed in a conventional microscope. A fiber optic light is then placed against the edge of the substrate to induce total internal reflection. Though the end-fire coupling into the slab waveguide is sub-optimal in this simple setup, high-contrast images are still produced. A beam blocker is placed in front of the objective to eliminate non-waveguided light from being collected by the objective. For C-WSM, the technique is similar: an opaque substrate is placed in a conventional microscope and a glass coverslip is placed on top, with a drop of refractive index-matching oil placed in between. The fiber optic light is then guided into the coverslip.

Standard DFM illumination was achieved using white light from a Zeiss HAL 100 halogen lamp installed on a Zeiss AxioImager A2M upright microscopy. A 10x objective with a numerical aperture of 0.2 and a working distance of 14.3 mm (Zeiss EC Epiplan 10x/0.2 HD WD=14.3 M27) was used for low magnification images and spectra. A 50x objective with a numerical aperture of 0.7 and a working distance of 1.1 mm (Zeiss EC Epiplan 50x/0.7 HD WD=1.1 M27) or a 100x objective with a numerical aperture of 0.8 and a working distance of 0.85 mm (Zeiss EC Epiplan 100x/0.8 HD WD=0.85 M27) was

used for high magnification images and spectra. Waveguide illumination was achieved by coupling a 150 W halogen lamp through a fiber optic cable (Schott ACE 1) into the end of a glass slide or coverslip. Note that the coupling efficiency into the waveguide is low; nevertheless, the 100-150 W halogen lamps typically installed on commercial microscopes provide sufficient power for WSM. Also note that the exact angle used for coupling the fiber source into the waveguide (see Figure 2.1) was not observed to have an impact on the images or spectra. All optical images were acquired with a CCD camera (AxioCam ERc 5s). Brightness and contrast adjustment were performed equally on all images. For WSM and DFM images, no corrections for the spectra of the two halogen lamps were applied because of the similarity of the two spectra (see Figure 2.2)

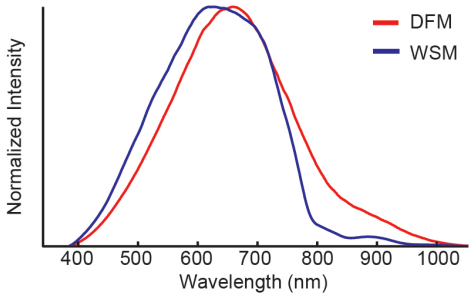

Figure 2.2: Halogen lamp spectra for DFM and WSM. A comparison of the normalized intensities of the spectra utilized for DFM (red) and WSM (blue) imaging and spectroscopy. The peaks of the two spectra are in similar positions. The WSM spectrum exhibits reduced intensity after 750 nm as a result of light absorption by the optical fiber.

2.3.1 Transition Width Fitting

The diameter profile obtained from an SEM image was fit to a previously reported[28] convolution of a Gaussian with an exponential to obtain the transition width. The equation is

$$f(t) = cA * exp\left[\frac{-((t-c_{t0})*\lambda_a - \sigma_a^2)}{\lambda_a^2}\right] * erf\left[\frac{\sqrt{2}*((t-c_{t0})*\lambda_a - \sigma_a^2)}{(2*\sigma_a*\lambda_a)+1}\right] + c_{I0} * \left[1 + erf\left[\frac{\sqrt{2}*(t-c_{t0})}{2*\sigma_a}\right]\right] + cA * erf\left[\frac{t-c_{t1}}{\lambda_b}\right] + c_{I1}, \quad (2.1)$$

where $cA = -c_{I0}$ and is the radius of the NW, c_{t0} is the location of the p-type/intrinsic transition, c_{t1} is the location of the intrinsic/p-type transition, σ_a is the Gaussian broadening, λ_a is the transition width of the p-type/intrinsic transition, λ_b is the transition width of the intrinsic/p-type transition, and c_{I1} is an offset based on the absolute position of the transitions.

2.4 Spectroscopy

DFM or WSM images were coupled into a Princeton Instruments Acton SP2500 spectrometer through a fiber-optic cable (Amphenol M40L01 400 μm 0.48 NA) through the side port of the AxioImager A2M for spectroscopic analysis. The microscope output was cropped by imaging with a CCD camera (Thorlabs DCC1645C) and an aperture mounted to the side port at the focal plane of the output port. Once cropped, the camera was removed and replaced with a fiber coupler. The light was detected by a liquid-nitrogen-cooled CCD array (Princeton Instruments LN/CCD-1340/400) coupled to a spectrograph (Princeton Instruments Acton SP2500) with a 150 groove/mm grating and a blaze angle centered for 500 nm. Longer wavelengths were collected with a long-pass filter (Thorlabs FGL570) placed in the beam path to prevent detection of second-order diffraction. Background scattering signals were collected in a similar fashion from a region of the sample without nanostructures. The background signal was subtracted from the scattering signal to yield the scattering spectrum. All spectra were divided by the spectrum of the white-light source (see Figure 2.2) to correct for spectral differences in illumination intensity. The DFM lamp spectrum was obtained using a Labsphere diffuse reflectance standard, and the WSM lamp spectrum was obtained by collecting the light scattered out of the end of the waveguide substrate. All optical measurements were performed after SEM imaging.

Sinusoidal NWs were prepared by dry transferring NWs from the growth substrate to a Si nitride wafer. The wires were then transferred to a flexible, stretched PDMS substrate ($\sim$2 mm thick; Dow Corning Sylgard 184) by direct contact of the two substrates. The tension in the PDMS substrate was slowly released, producing sinusoidal NWs similar to those described in the literature.[90]

2.5 Simulations

2.5.1 Optical Simulations

FDFD finite-element simulations were performed with COMSOL Multiphysics. Three-dimensional optical simulations were implemented using the total-field, scattered-field method. For DFM simulations, the background field was evaluated with a plane wave incident at an oblique angle ($\sim$60° with respect to surface normal) on the substrate using periodic boundary conditions on the four horizontal boundaries, a perfectly matched layer (PML) on the lower boundary, and the plane wave source on the upper boundary. The scattered field was then solved after adding the photonic structure to the simulation domain and replacing all boundaries with PMLs. For WSM simulations, a similar approach was utilized, except that the plane wave was incident at an oblique angle ($\sim$65° with respect to surface normal) from within the glass substrate to produce total internal reflection in the glass. Images of the surface plasmon modes in Au nanorods (NRs) were generated by evaluating the scattered electric field intensity ($|E|^2$) in a horizontal plane bisecting the nanorod. Images of the surface plasmon modes in nanohole simulations were produced by evaluating the total field intensity ($|E|^2$) in a horizontal plane 40 nm above the surface of the structure. To evaluate optical resonances in *p-i-n* structures, two-dimensional optical simulations were implemented using the total-field, scattered-field method. The background field was evaluated with a plane wave normally incident on the substrate using periodic boundary conditions on the two vertical boundaries, a perfectly matched layer (PML) on the lower boundary, and the plane wave source on the upper boundary. The scattered field was then solved after adding the NW to the simulation domain and replacing all boundaries with PMLs.

2.5.2 Electrostatic Simulations

Finite-element simulations were performed with COMSOL Multiphysics to predict the current-voltage characteristics of axial *p-i-n* diodes using the model reported previously but without Auger recombination.[84] Axially symmetric two-dimensional simulations were used to model the three-dimensional structure. The intrinsic region was varied from 200 nm to 2 μm, with 1 μm long p-type and n-type segments, doped at $2x10^{19}$ cm^{-3}. A 10 nm dopant transition width was used. The models incorporated standard drift and diffusion physics with Shockley-Read-Hall (the recombination lifetime was fixed at

1 μs) and surface recombination mechanisms. For simulations under approximate 1-sun illumination (Figure 5.1C and Figure 5.5A,C,D), an additional uniform charge carrier generation term corresponding to a J_{SC} value of 7 mA/cm^2 was assumed. For comparisons between experiment and simulation in Figure 5.10B and Table 5.1, the experimental 1-sun *I-V* curves were fit to simulated dark *I-V* curves shifted by the experimental I_{SC} value. For the analytical calculation of I_{SC} for comparison to simulations, eq. 5.14 was modified to integrate only over the 1 μm length of the n-type and p-type segments used in the simulations. For calculation of IQE, a generation term of 6 mol/($cm^{-3} \cdot s^{-1}$) was introduced stepwise in 5x5 nm^2 areal elements of the cylindrically symmetric simulation domain. Ohmic metal contacts on both n- and p-type segments were assumed to be carrier selective to avoid recombination and narrow-base diode effects in the simulation.

2.6 Microfabrication

2.6.1 Marker Pattern Fabrication

Marker patterns were produced as either positive or negative patterns. For positive patterns, an MMA/PMMA (MMA EL9, PMMA A2, Microchem) resist stack was spun onto Si/SiO_2/Si_3N_4 wafers at 4000 rpm using a spin coater (Laurell Technologies Model WS-650-23B). Each layer was spun for 30 s and dried at 180 °C for 60 s. Marker patterns were designed and fabricated through electron beam lithography (EBL, Nanometer Pattern Generation System connected to the Helios 600) with an accelerating voltage of 30 kV, beam current between 340 pA and 11 nA, and dosage of 350 μC/cm^2. The inner pattern was written at a magnification of 100x and the outer pattern was written at a magnification of 65x. The pattern developed in methyl isobutyl ketone (MicroChem MIBK/IPA 1:3 Developer) for 60s before being rinsed with IPA. A metal stack (Cr, 3nm; Au, 50 nm) was deposited with either thermal evaporation (Key High Vacuum KV-301) or electron-beam evaporation (Thermionics VE-100) and followed by lift off in acetone. The metal was degassed by achieving a deposition rate of 0.2Å/s with the shutter closed for several minutes. During deposition, the shutter was opened and the metal was deposited at a rate between 0.2-1Å/s. The micron-scale patterns shown in Figure 3.1 were prepared in the same way as the positive marker patterns.

For negative patterns, a resist stack of MMA/MMA/PMMA A7 was spun onto the nitride wafers at 4000 rpm. Marker patterns were fabricated with EBL at an dosage of 500 μC/cm^2 and developed in

MIBK. The pattern was then etched using deep reactive ion etching (Alcatel AMS 100 Deep Reactive Ion Etcher). The oxide and nitride portions of the substrate were etched over 3 minutes using 20 sccm of C_4F_8 and 150 sccm of Ar, with a position of 25%, source power of 1000 W, and substrate power of 75 W. The silicon was etched over 45 seconds using 100 sccm of SF_6 and 100 sccm of Ar, with a position of 25%, source power of 500 W, and substrate power of 50 W. Any remaining resist was removed by rinsing in acetone and cleaning with the UV-Ozone cleaner.

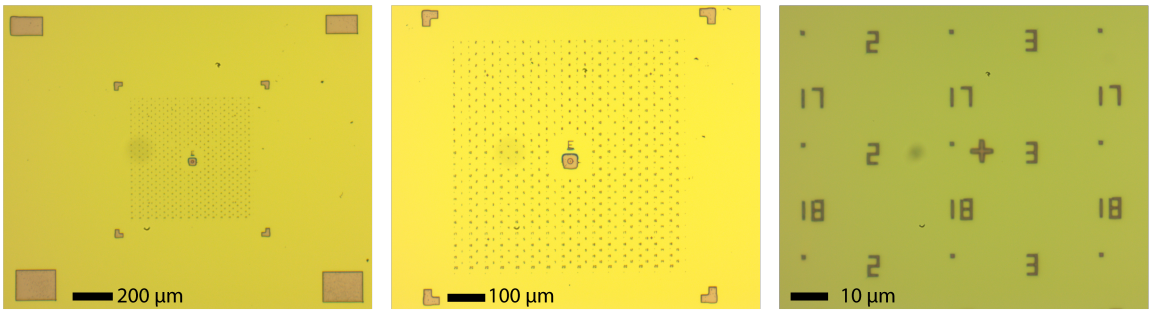

Figure 2.3: Marker pattern. An example of a marker pattern after dry etching

2.6.2 Nanowire Contact Fabrication

NWs were mechanically transferred onto the marker patterns and where appropriate, etched following the described procedure. Oxidation occurred in a hot-wall furnace (Lindberg Blue M, Thermo Scientific) with 3 temperature controlled zones and a 5 inch bore. A specific reaction time was achieved by placing the samples in a quartz boat connected to a quartz rod with a magnetic end. An external magnet was used to slide the quartz boat in and out of the heated zone. The quartz boat began outside of the heated zones and the system was evacuated to base pressure. The first zone was then heated to 950 °C with 20 sccm Ar flowing. After reaching the set temperature, the Ar was evacuated and the system was filled with O_2 at a flow rate of 20 sccm to a pressure of 200 Torr. The sample was then inserted into the heated region for 60 s using the magnet. At the completion of the oxidation, the sample was removed from the heated region, the O_2 was evacuated, and the system was flushed with Ar. The first zone was then cooled to 600 °C and the sample was reinserted. The annealing process was carried out in a 10% H_2/90% Ar atmosphere at 500 Torr, ramping the temperature from 600 °C to 300 °C over 2 hrs.

Alternative procedures for oxidation and annealing were also developed using a ULVAC- RIKO MILA-5000 Rapid Thermal Annealer. For oxidation, the intrument was evacuated and filled with pure

O_2 to 760 Torr. The sample was then rapidly heated to 950 °C and held for between 10 and 30 s. The substrate was then rapidly cooled while the chamber was evacuated. For annealing, the chamber was evacuated and filled with forming gas (10 % H_2, 90 % N_2, Airgas) to 760 Torr. The substrate was then rapidly heated to 600 °C and held for 10 min. The temperature was then ramped down to 300 °C over 90 min. The temperature is then held at 300 °C for 15 min before being ramped to 150 °C over 15 min. The wires used for four-point probe did not undergo the oxidation and annealing process. DFM images of the marker patterns taken at 10x, as well as higher resolution images of specific NWs taken at 50x, were used to register the position using custom Igor software. A point matrix containing the positions of the NWs was exported to DesignCAD, and contact lines $\sim 1\mu$m wide were drawn to connect each NW to larger contact pads.

A resist stack of MMA/MMA/PMMA A2 was then spun on top of the NWs. Under the SEM, alignment markers were used to correctly orient the designed contact pattern. The NW contacts and measurement pads were patterned using EBL. After patterning, the sample was developed in MIBK. In the clean room, the NW oxide was etched with BHF for 15 s, washed in nanopure water twice, and rinsed in IPA before being blown dry with nitrogen. The sample was then inserted into the electron beam evaporator and pumped down within 2 minutes to prevent the accumulation of an oxide on the bare NW surface. After pumping overnight to a base pressure of $\sim 9x10^{-8}$ Torr, the Ti and Pd sources were degassed. Once the system achieved base pressure after degassing, metal contacts were deposited (3 nm Ti, 300 nm Pd) using an initial deposition rate of 0.2Å/s. When the thickness of the Pd was above 10 nm, the rate was increased to 0.5Å/s, and above 100 nm, the rate was further increased to 1Å/s. After deposition, the excess metal was lifted off in acetone.

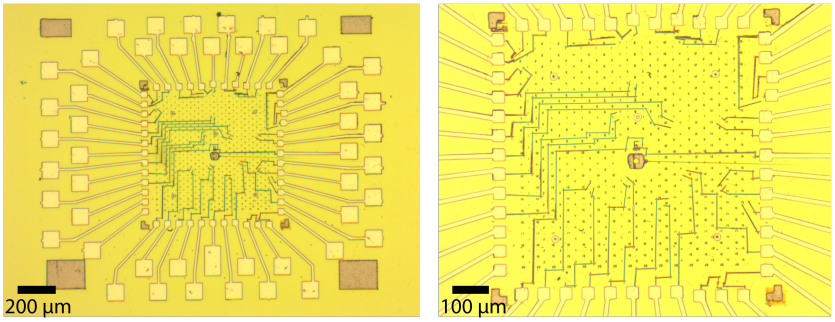

Figure 2.4: Nanowire contacts. An example of a metal contacts fabricated on NWs.

2.6.3 Nanohole Fabrication

A Ag film $\sim$170 nm thick was deposited onto a glass slide with an electron-beam evaporator (Thermionics VE-100) at normal incidence with a rate of $\sim$1 Å/s at a pressure$\sim 1x10^{-7}$ Torr. Arrays of rectangular nanoholes were fabricated in the Ag film by focused ion beam milling (FEI Helios 600 Nanolab Dual Beam system) at a typical ion acceleration voltage of 30 kV and current of 28 pA. Each nanohole is 200 nm x 260 nm with an x and y pitch of 550 nm and 450 nm, respectively.

2.6.4 PCB Fabrication

A contact pattern was first designed that would allow for a back contact to the wafer as well as numerous additional contact lines. This pattern was then printed onto Pulsar PCB toner transfer paper. A PCB blank was then scoured and scrubbed clean before use. This pattern was then transferred to the copper side of the PCB blank by pressing the transfer paper onto the PCB blank and passing it through an Apache laminator at 375 °F multiple times. The paper was removed by soaking in warm water. Any defects in the pattern were corrected with a an etch-resistant marker. Additional protection was then provided by laminating Pulsar Green Toner-Reactive Foil to toner marks using the same heating process. An etch bath was prepared in a glass dish with 50 mL of HCl (12M, Fisher Scientific) and 200 mL of water. The PCB was placed in the bath using plastic implements and was completely submerged. Hydrogen peroxide (30% aq., Fisher Scientific) was slowly added until bubbling was observed. The PCB was agitated in this solution and additional peroxide was added as needed. The bath turns green as the copper is oxidized and catalyzes the reaction, increasing its exothermicity. When all exposed copper was removed, the PCB was washed in water and scrubbed to remove the toner. Breakaway female pin-headers were then soldered onto the copper lines.

2.7 Device Measurement

2.7.1 IV Measurement

Light and dark current-voltage (*I*-*V*) measurements were taken using a Keithley 2636A SourceMeter in conjunction with Signatone micropositioners (S-725) and probe tips (SE-TL) averaged over 10 power line cycles with a measurement delay of 0.5 s between voltage steps. Each measurement consisted of

at least 100 voltage steps. Light measurements involved illumination from a Newport model 91191 (1 kW Xe lamp) solar simulator with an AM1.5G filter and was calibrated to 1-sun (100 mW/cm$_2$) using a calibrated reference solar cell (Newport model 91150V). Power dependent measurements focused this light source to various sizes using a single lens.

2.7.2 Four-Point Probe

Four-point probe measurements were taken using a Keithley 2636A SourceMeter in conjunction with a Lake Shore Cryotronics probe station (PS-100). The current sourced on the outer contacts was swept from -100 nA to +100 nA over 300 steps, with each step averaged over 5 power line cycles and with 0.3 s delay between each step. The voltage was measured across the inner two contacts using a dual-channel configuration, in which channel A sourced current along the outer contacts and was grounded, while channel B measured voltage along the inner contacts and was floating.

2.7.3 EQE Measurement

To perform EQE measurements, a device was first tested with probes, mounted onto a prefabricated PCB carrier with carbon tape, and appropriate contacts were wire bonded to the PCB. Previous to wire bonding, the copper contacts were scoured and cleaned to removed copper oxide, which can prevent an ohmic contact. Special care was taken to remain grounded and static-free when handling wire-bonded devices. Wire bond connections were made with a West Bond Model 7476D-79 wire bonder, using 1% Si/Al wire. Wire-bonded connections were then plugged into wires that were soldered to coaxial connectors. The PCB carrier was mounted on a rotating stage to enable polarization measurements. Photocurrent measurements were performed with the same SourceMeter and a supercontinuum laser (NKT Photonics, SuperK Extreme) operating at 78 MHz passing through a spectrograph (Princeton Instruments, SpectraPro SP-2300) with slits set at 1.5 mm. A Glan-Thomson polarizer (Thorlabs, GTH10M) was used to achieve polarization control; it was set at 45° relative to the spectrograph slit to average out the polarization-dependent dispersion efficiency of the grating. Measurements were taken at 5 nm increments, with light and dark measurements taken at each wavelength. Dark measurements were subtracted, and the photoresponse was corrected for the power spectrum of the illumination source, as measured by a calibrated silicon photodetector (Newport model 918D-SL-OD1). The pulsed source operates at 78 MHz, and the observed currents were $\sim$10 pA, which equates to approximately one

collected charge carrier per laser cycle. Thus, EQE spectra measured in this configuration should be equivalent to what would be measured in a continuous-wave configuration.

2.7.4 AFM Measurements

The near-field microscopy experiments were performed using a home-built infrared s-SNOM system based on a modified commercial AFM (Bruker Innova) as described in Ritchie et al.[77] A vertically polarized CO_2 laser (Access Lasers) at 10.6 μm wavelength is used as an excitation source. s-SNOM experiments were carried out with a homodyne interferometric scheme. The intensity of the near-field signal was demodulated at the third harmonic (n = 3) of the tapping frequency and used to construct an optical image simultaneously with the AFM topography. To allow for comparison of the near-field signal across samples, Si NWs were deposited onto Au-coated Si_3N_4 substrates and were normalized to the high-intensity signal from the gold surface. Near-field spatial resolution was determined from near-field approach curves to be $\sim$10 nm. Several scans (2 x 2 μm, 256 x 256 pixels) were taken along the length of the wire to observe the doping profile. Doping assignments were determined by comparing section lengths to the dopant flow profile. The n-type sections were shown to have the highest near-field intensity, with p-type sections having a lower intensity, and intrinsic Si having the lowest. We observe an average n-type length of 342 $\pm$ 6.8 nm, p-type length of 790 $\pm$ 13 nm, and intrinsic Si length of 1730 $\pm$ 55 nm.

WAVEGUIDE SCATTERING MICROSCOPY FOR DARK-FIELD IMAGING AND SPECTROSCOPY OF PHOTONIC NANOSTRUCTURES

"Nature and Nature's laws lay hid in night: God said, "Let Newton be!" and all was light."

- Alexander Pope

3.1 Introduction

Dark-field microscopy (DFM) is used extensively in biological and materials research for applications ranging from single nanoparticle spectroscopy[91–97] to label-free live tissue imaging.[93,98–103] As illustrated in Figure 3.1A, DFM typically requires white-light illumination of a sample at oblique angles and collection of the scattered light by an objective lens, producing a bright object surrounded by a dark background. In nanomaterials research, DFM has become particularly useful because nanoscale objects strongly scatter light at specific wavelengths as a result of optical resonances that depend on the size, shape, and composition of the material. For instance, Mie resonances in semiconductor nanowires (NWs) produce distinct colors that strongly depend on the wire diameter,[45,47,55,104] and the frequencies of localized surface plasmon resonances in anisotropic metallic nanoparticles are well known to depend on the particle size and aspect ratio.[91–97,105] When integrated with a spectrometer, DFM enables quantitative measurement of these types of wavelength-dependent scattering characteristics in single nanoscale objects.

Despite the ubiquity of DFM, the technique presents several limitations or caveats. First, the angular distribution of the white-light source varies from microscope-to-microscope, producing a range of results

Portions of this chapter reproduced with permission from Hill, D. J.; Pinion, C. W.; Christesen, J. D.; Cahoon, J. F. Waveguide Scattering Microscopy for Dark-Field Imaging and Spectroscopy of Photonic Nanostructures. *ACS Photonics* **2014**, *1* (8), 725731. Copyright 2014 American Chemical Society.

from the same sample when imaged with different DFM systems.[106,107] Second, the polarization of the input white light is difficult to control because of the angular distribution of the incoming rays, preventing highly selective excitation of polarization-dependent optical resonances in anisotropic objects.[108] Third, the incident light is supplied by a lens, which limits the range of angles that can be collected by the objective lens and reduces the numerical aperture and resolution of the image.

Here, we describe an alternative DFM method called waveguide scattering microscopy (WSM),[109–111] which illuminates nanoscale objects in the near field using white-light transmitted through a multi-mode dielectric slab waveguide. Light scattered into the far field is collected by an objective lens to generate a dark-field, full-color image. WSM is similar to both total internal reflection microscopy (TIRM)[112–117] and total internal reflection fluorescence microscopy (TIRFM),[118,119] but it uses an incoherent white-light source coupled to a waveguide to generate the evanescent field rather than a laser source coupled to a lens or prism. In a few instances, TIRM has been performed with white light illumination to evaluate plasmon resonances in Au nanoparticles.[112–115] Similarly, Au nanorods have been deposited and imaged on the surface of an optical fiber waveguide coupled to a halogen lamp.[120] Waveguide-based variations of TIRFM have also been performed by coupling laser or diode light sources into glass waveguides.[121–126] In addition, optical fiber waveguides and slab waveguides are commonly used to perform spectroscopy in both the infrared[95] and optical[96] regimes on samples deposited in the near field of the waveguide surface. Here, we use WSM to both image and spectroscopically analyze plasmonic and photonic nanostructures. WSM is utilized to produce images and spectra with high signal to background ratios and excite polarization dependent scattering modes in metallic and dielectric nanostructures. WSM is surprisingly easy to implement using standard microscope equipment and can overcome limitations encountered with standard DFM for specific applications.

3.2 Results and Discussion

A standard DFM configuration is illustrated schematically in Figure 3.1A for both forward-scattering (F-DFM) and backward-scattering (B-DFM) geometries. In F-DFM, the substrate is transparent and light is incident and collected on opposite sides of the substrate. In B-DFM, the substrate is often opaque and light is incident and collected on one side. Two analogous WSM configurations are illustrated in Figure 3.1B. If the substrate is transparent (such as a standard glass microscopy slide), then total internal

reflection of white light within the substrate provides waveguide illumination for objects on the surface. If the substrate is opaque, a coverslip can be placed on the substrate using an optical-quality oil at the interface between the nanostructure and coverslip. Total internal reflection within the coverslip provides waveguide illumination, and the oil serves to improve light coupling by homogenizing the local refractive index and increasing physical contact between the substrate and coverslip through capillary forces. In the two WSM configurations, referred to as substrate waveguide scattering microscopy (S-WSM) and coverslip waveguide scattering microscopy (C-WSM), respectively, light scattered out of the waveguide by the sample is collected with an objective lens to form a dark-field image.

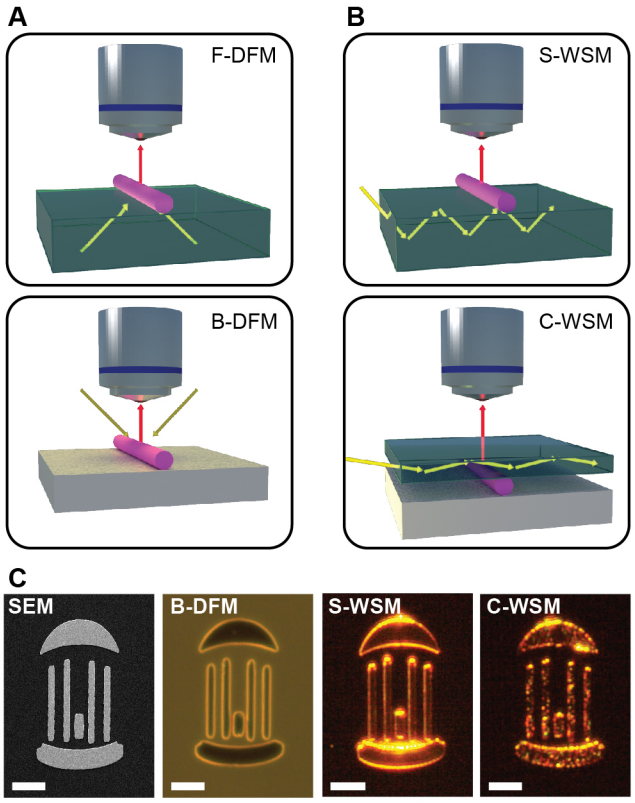

Figure 3.1: Comparison of conventional DFM and WSM (A) Schematic of conventional forward-scattering (upper) and backward-scattering (lower) DFM systems. (B) Schematic of a substrate-based (upper) and coverslip-based (lower) WSM apparatus. Green substrates indicate transparent materials and white substrates indicate opaque materials; however, the substrate in B-DFM and C-WSM may be opaque or transparent. In C-WSM, an index-matching oil is placed in vicinity of the nanostructure to enhance optical coupling. (C) Images of a micropatterned logo defined in a 50-nm thick Au film by electron-beam lithography on glass, showing SEM image (far left) and DFM (middle left), S-WSM (middle right), and C-WSM (far right) optical images with a 10x microscope objective; all scale bars, 20 μm.

We implemented WSM on a standard upright microscope (Zeiss Axio Imager A2M; see Figure 2.1) using an inexpensive fiber-coupled tungsten halogen lamp as the white light source. The white light was coupled into standard microscope slides and coverslips at the unpolished edges of the glass (see Figure 3.2 and Methods). A comparison of dark-field images generated with B-DFM, S-WSM, and C-WSM is shown in Figure 3.1C for a simple micron-scale Au pattern deposited on a glass substrate. The B-DFM produces an image with significant background signal due to refraction and reflection within the substrate.

In contrast, the two WSM modes produce high-contrast images with negligible background signal. In addition, the S-WSM exhibits sensitivity to the edges of the pattern whereas C-WSM is sensitive to surface topology, producing an image of surface irregularities in the Au film. This latter effect results from the high surface sensitivity of the evanescent field (see Figure 3.3).

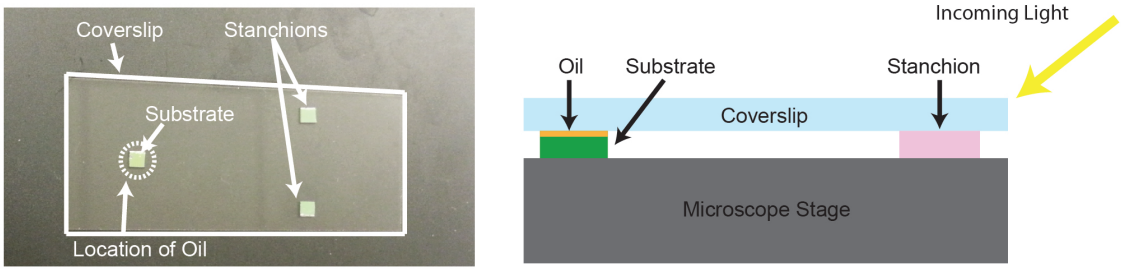

Figure 3.2: Geometry of the coverslip for C-WSM. An image of the configuration of the substrate used for C-WSM (left) and a side-view diagram (right), highlighting the locations of the coverslip, index-matching oil, and substrate containing nanostructures. Stanchions keep the coverslip level. The base plate acts as a support and can be any transparent or opaque material.

3.2.1 Plasmonic Nanoparticle Spectroscopy

In addition to imaging, DFM is extensively used for the spectroscopic analysis of nanostructures, such as Au nanoparticles and nanorods exhibiting localized surface plasmon resonances.[92,97,105,127,128] Similar to previous analyses of Au nanostructures by TIRM,[112–115] WSM can be used to image and analyze these materials, as illustrated in Figure 3.4. Au nanorods $\sim$150 x 50 nm in length and diameter, respectively (Figure 3.4A), appear as bright orange spots in both B-DFM and S-WSM (Figure 3.4B). S-WSM provides an image with substantially improved contrast ratio because of the suppressed background scattering. Optical simulations of the plasmon resonance in these particles using finite-difference frequency-domain (FDFD) calculations (see Methods) demonstrate that the optical field in both DFM and WSM (Figures 3.4C and 3.4D, respectively, as well as Figure 3.5) can excite the transverse and longitudinal plasmon resonances in the nanorod.

Scattering signals, as shown in Figure 3.4E, were measured from the same ensemble of nanorods using B-DFM and S-WSM. Background signals (without nanorods) were also measured and subtracted from the scattering signals to yield the final scattering spectra, as shown in Figure 3.4F. Although

background subtraction is critically important for DFM, the background signal from WSM is both low in amplitude and spectrally featureless (e.g. compare red and blue dashed curves in Figure 3.4E), eliminating the need to collect a background spectrum. Quantitatively, the maximum signal-to-background ratio for DFM is ∼2.2 whereas the maximum value for WSM is ∼14,000. Background suppression is thus one key advantage of WSM over DFM for the spectroscopic analysis of photonic nanostructures. As expected from the optical simulations, the DFM and WSM spectra both exhibit peaks for the longitudinal (∼670 nm) and transverse (∼550 nm) modes.

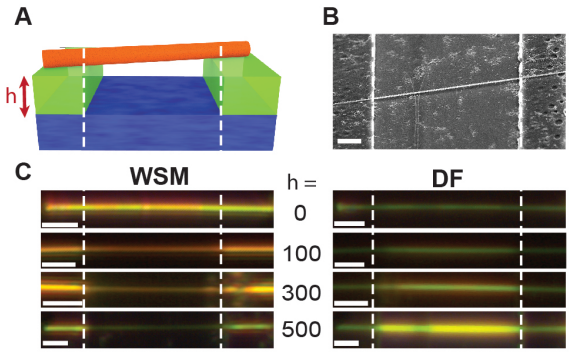

Figure 3.3: Surface Sensitivity of WSM (A) Schematic of a wire suspended over a PMMA trench on glass. (B) Titled (52) SEM image of a suspended wire; scale bar, 2 μm. (C) Optical images of wires suspended over PMMA trenches of varying heights (in nanometers) under S-WSM (left) and B-DFM (right) illumination; scale bars, 2 μm. Trenches ∼10 μm wide were formed in poly(methyl-methacrylate) by electron beam lithography, and the depth of the trenches was varied systematically (100 nm, 300 nm, and 500 nm). Silicon nanowires ∼100 nm in diameter were then suspended across the trenches. Under S-WSM illumination, the intensity of the scattered light observed from the suspended NWs progressively decreased with increasing trench depth, an effect that is attributed to the exponential decay of the evanescent field. Under B-DFM illumination, however, the opposite trend is observed: the suspended segments appear brighter as the trench depth increases. This observation is attributed to a light-trapping effect in the trench.

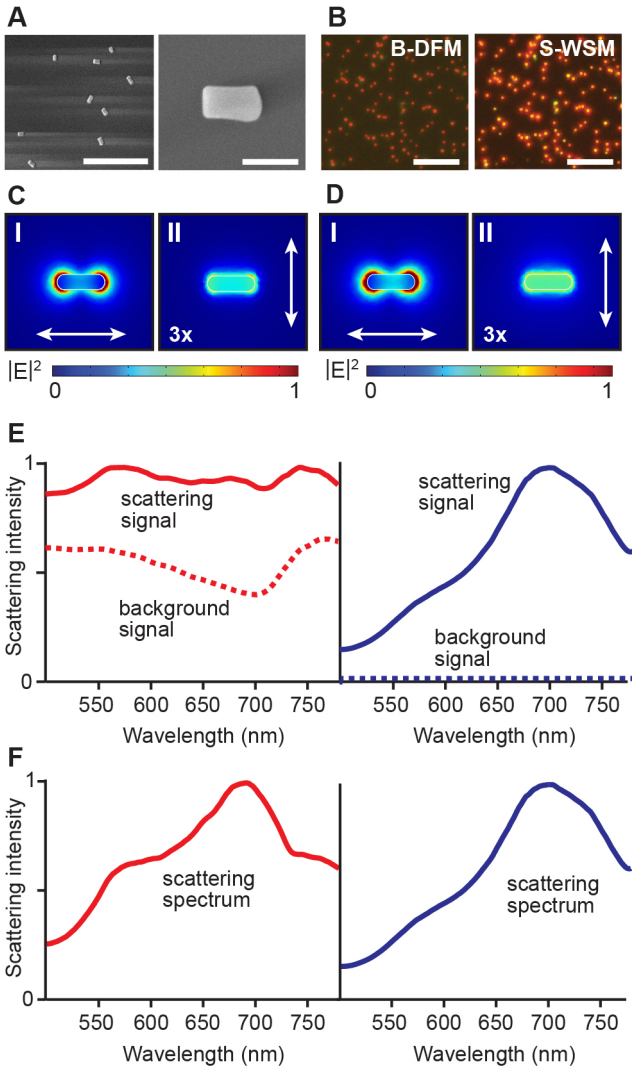

Figure 3.4: Comparison of scattering spectra from plasmonic nanorods acquired with DFM and WSM (A) SEM images of Au nanorods; scale bars, 1 μm (left) and 100 nm (right). (B) B-DFM image (left) and S-WSM image (right) of multiple Au nanorods; scale bars, 50 μm. (C and D) Optical simulations of the longitudinal (I) and transverse (II) plasmon resonances in Au nanorods on a glass substrate excited using a plane wave incident at 60 with respect to the surface normal (panel C) or waveguided in the substrate (panel D), representing DFM and S-WSM configurations, respectively. Directions of the electric field polarizations are denoted by double-headed arrows, and intensities of the transverse modes (II) are scaled by a factor of 3 to increase their visibility. See Figure S4 for cross-sectional images of these resonances. (E) Scattering signal collected from an ensemble of Au nanorods (solid) and background signal (dashed) collected from the substrate for B-DFM (left, red) and S-WSM (right, blue). (F) Scattering spectrum of Au nanorods generated by subtracting the substrate background signal from the scattering signal in panel E for B-DFM (left) and S-WSM (right). Differences in the scattering spectrum result from differences in the illumination geometry, which shift the relative intensities and resonance frequencies of individual nanorods. All spectra in panels E and F were corrected based on the spectrum of the white light sources (see Methods).

3.2.2 Dielectric Nanowire Scattering Spectroscopy

We also investigated the scattering spectra from Si NWs, which behave as cylindrical, subwavelength Mie scattering centers.[45,47,55,104] Because the wires lie on substrates that break the cylindrical symmetry, scattering peaks measured by DFM tend to shift with the various illumination angles produced by different microscope objectives. This type of substrate effect has been observed in the scattering from plasmonic nanoparticles.[129] In some cases, it can be used advantageously to excite specific, angle-dependent optical resonances, although it also adds a complication to the interpretation of scattering spectra. This effect is illustrated by DFM and WSM images and scattering spectra (Figure 3.6A and 3.6B, respectively) collected on the same Si NW 50 nm in diameter. A conventional DFM image collected with a 100x objective shows a red NW, and scattering spectra (red curve) show Mie resonances at ∼405 nm and ∼650 nm. For DFM collected with a 10x objective (red dashed curve in Figure 3.6B), however, the Mie resonances red shift by ∼40 nm and ∼100 nm for the short and long wavelength peaks, respectively. In contrast, WSM produces images with a blue color and spectra that show a single Mie scattering resonance (blue curves in Figure 3.6B). Most importantly, the scattering resonance observed with WSM does not shift with the microscope objective, showing a peak at ∼470 nm with both 100x and 10x objectives.

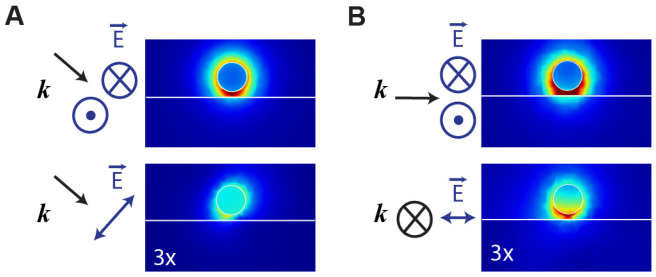

Figure 3.5: Cross-sectional view of plasmon resonances in Au nanorods. Optical simulations of the longitudinal (upper) and transverse (lower) plasmon resonances in Au nanorods on a glass substrate excited using a (A) plane wave incident at 60 with respect to the surface normal or (B) substrate-based waveguide, representing DFM and S-WSM configurations, respectively. Directions of the electric field polarizations are denoted by double-headed arrows, incident k vectors are indicated by single-headed arrows, and the intensities of the transverse modes (lower) are scaled by a factor of 3 for clarity.

To examine the diameter-dependent scattering of Si NWs, we fabricated a single NW with six distinct diameters along the growth axis (Figure 3.6C) using the ENGRAVE (Encoded Nanowire GRowth and Appearance through VLS and Etching) process described elsewhere.[21] For the largest diameters (∼200

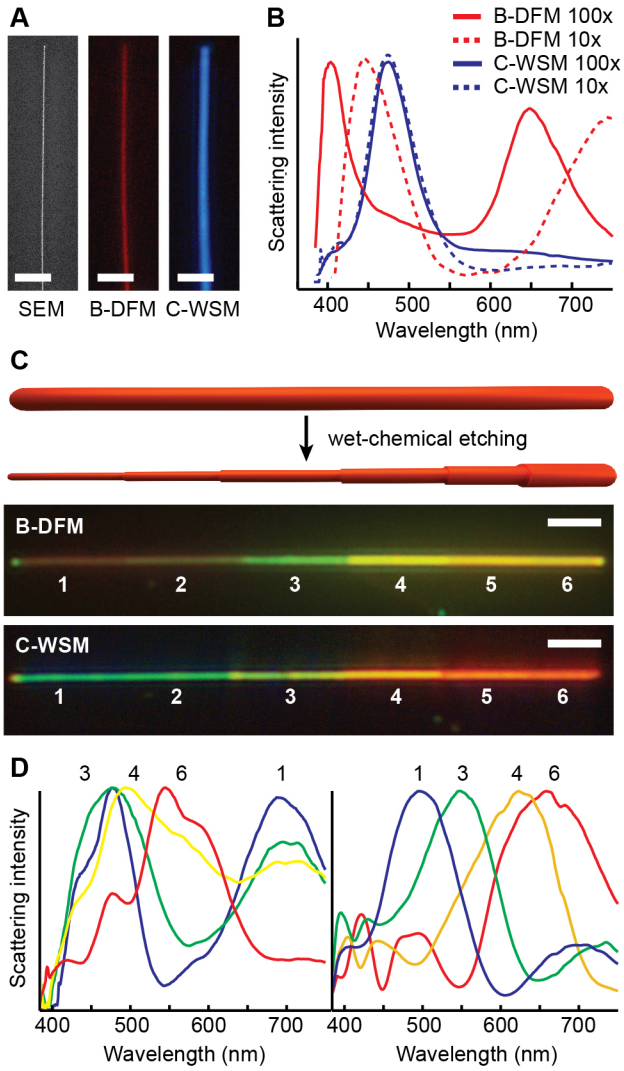

Figure 3.6: Comparison of Mie scattering spectra from Si NWs acquired with DFM and WSM (A) SEM (left), DFM (middle), and WSM (right) images of a 50 nm diameter Si NW; scale bars, 2 μm. (B) Comparison of the scattering spectra using DFM with a 100x objective (solid red) and 10x objective (dashed red), and C-WSM with a 100x objective (solid blue) and 10x objective (dashed blue). (C) Upper: schematic illustration of a Si NW encoded with six distinct diameters by the ENGRAVE process, which uses selective wet-chemical etching to reduce the wire diameter. Lower: Images collected by B-DFM (top) and C-WSM (bottom) of the diameter-encoded NW; scale bars, 5 μm. Regions of different diameter are denoted by the numbers 1-6. (D) Scattering spectra collected by B-DFM (left) and C-WSM (right) of select regions of the NW shown in panel C.

nm), the wire scatters yellow or red light followed by progressively shorter wavelengths for smaller diameters, producing the rainbow effect in the images in Figure 3.6C. C-WSM scattering spectra collected from sections with distinct diameters (Figure 3.6D, right) confirm a smooth shift of the scattering peaks to shorter wavelengths. For B-DFM, however, the spectral response (Figure 3.6D, left) is more complex because of the broad distribution of input wavevectors, and a clear progression is not easily discerned.

3.2.3 Polarization Control

In addition to diameter-dependent effects, the scattering of anisotropic nanostructures depends on the polarization of the electromagnetic field. In DFM, polarization control is exerted by placing polarization optics in the incident or scattered beam paths. In WSM, however, polarization control can be achieved simply by changing the direction of the wavevector,*k*, for the light source (see Figure 3.8 for details). Light in a multimode waveguide is composed of both *s*-polarized and *p*-polarized fields, as illustrated in Figure 3.7A.[130] At the waveguide surface, however, the evanescent field is linearly polarized (parallel to the surface) for the *s*-polarized light and is elliptically polarized in the plane of incidence for the *p*-polarized light (with components primarily perpendicular but also parallel to the surface).[113,114,131] For nanostructures with high aspect ratios, particularly NWs,[132] light scattering is strongly favored for light polarized parallel to the long axis of the structure. For nanostructures lying on the waveguide surface, this results in preferential scattering by *s*-polarized light if the long axis of the nanostructure is oriented perpendicular to *k*, referred to as the transverse magnetic (TM) direction (Figure 3.7A top). Orientation parallel to *k*, referred to as the transverse electric (TE) direction, minimizes scattering by the *s*-polarization (Figure 3.7A bottom). Because anisotropic structures are typically oriented with the long axis parallel to the substrate surface, scattering from *p*-polarized light is minimal (see Figure 3.10).

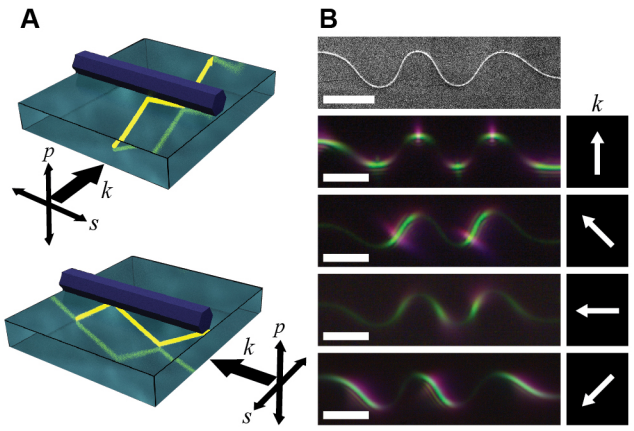

Figure 3.7: Polarization-selective illumination of Si NWs with WSM (A) Schematic of TM (top) and TE (bottom) waveguide illumination of a NW, showing the *s*-polarized electric field parallel and perpendicular, respectively, to the wire axis. (B) SEM (top) and WSM images (bottom) of a sinusoidal Si NW under waveguide illumination using the wavevector directions denoted by arrows; scale bars, 5 μm.

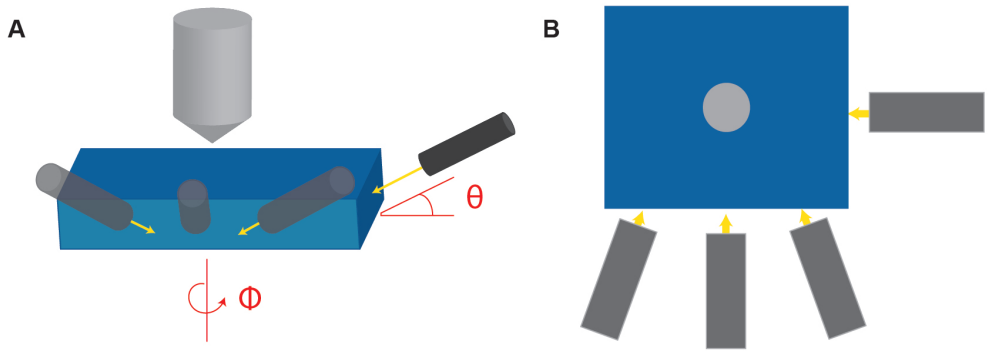

Figure 3.8: Directional coupling into the waveguide to control the wavevector. (A) Schematic demonstrating the method by which light from the fiber optic cable is coupled into the waveguide. The angle theta () is set to achieve total internal reflection, but the exact angle utilized may vary. The fiber optic cable may be rotated around the substrate by angle phi () to change the polarization of the light relative to a given axis of nanostructure of interest. (B) Top-down view of the schematic illustrating the rotation of the light source about angle phi

This polarization effect is well illustrated by WSM images collected on a sinusoidal Si NW using four distinct directions for *k* (Figure 3.7), achieved by altering the position of the light source relative to the nanowire axis (Figure 3.8). Sinusoidal wires were created following a literature procedure[90] for depositing NWs on a flexible, stretched polydimethylsiloxane (PDMS) substrate, which was then released to form bent wires in a planar sinusoidal shape (see Methods for details). Because PDMS is transparent, it was also utilized as the waveguide substrate, illustrating the generality of the WSM technique for any

planar, optically transparent substrate material. As shown by the WSM images for specific k directions in Figure 3.7B, segments of the wire satisfying the TM condition exhibit strong light scattering whereas segments satisfying the TE condition are dark. These images confirm that light scattering primarily results from the s-polarization and confirm that the input k direction provides polarization control for imaging and analysis of anisotropic nanostructures by WSM.

To demonstrate WSM polarization control with plasmonic nanostructures, we fabricated an asymmetric array of rectangular nanoholes in an Ag film deposited on a glass substrate, as shown in Figure 3.9A (see Methods for fabrication details). Plasmon resonances in these types of structures have been shown to depend on the polarization of incoming light, causing the transmission of different wavelengths for orthogonal polarizations of the incoming beam.[133–135] As shown in Figure 3.9B, we performed optical simulations of the Ag nanohole array under waveguide illumination with the wavevector parallel (vertical s-polarization) and perpendicular (horizontal s-polarization) to the long axis of the array. These simulations confirm that distinct surface plasmon resonances can be excited by the waveguide at wavelengths of $\sim$600 nm for the vertical polarization and $\sim$800 nm for the horizontal polarization.

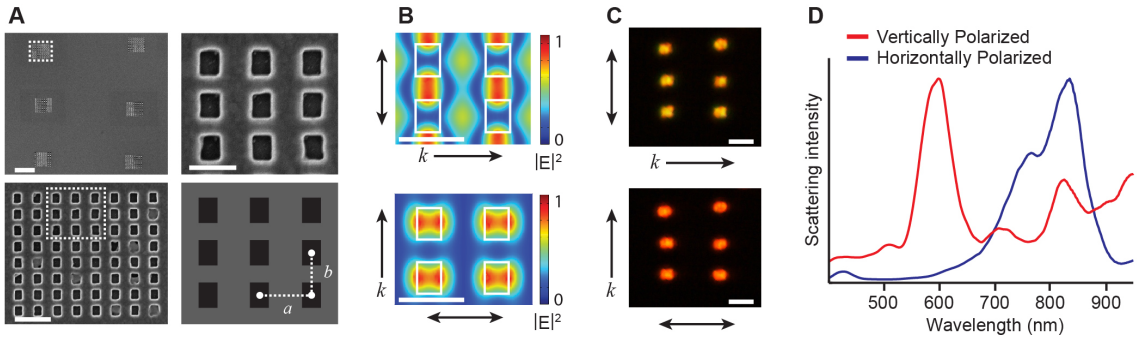

Figure 3.9: Polarization-selective illumination of plasmonic Ag nanohole arrays with WSM (A) SEM images of a set of six 8 x 8 Ag nanohole arrays, showing all six arrays (upper left; scale bar, 5 μm), a magnified image of a single 8 x 8 array (lower left; scale bar, 1 μm), and a magnified image of nine nanoholes (upper right; scale bar, 500 nm). Dashed white boxes denote the magnified regions. Lower right: The nanohole geometry used for optical simulations with a horizontal pitch, a, of 550 nm and vertical pitch, b, of 450 nm (B) FDFD optical simulations showing the electric field intensity (—E—2) 40 nm above the surface of the Ag film for vertically (upper) and horizontally (lower) s-polarized illumination of the array with wavevector and polarization directions indicated by single- and double-headed arrows, respectively; scale bars, 500 nm. (C) WSM images of six 8 x 8 nanohole arrays obtained for vertically (upper) and horizontally (lower) s-polarized illumination; scale bar, 1 μm. (D) WSM scattering spectra obtained for vertically (red) and horizontally (blue) s-polarized illumination of the nanohole arrays shown in panel C.

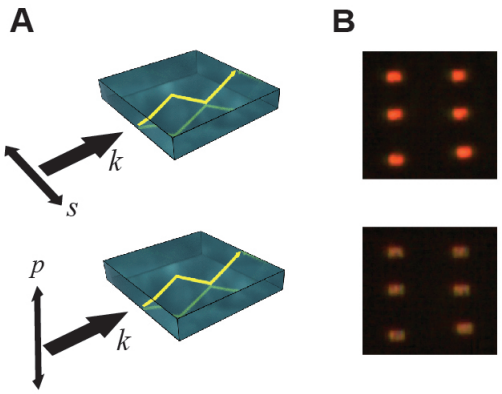

Figure 3.10: Polarization of WSM. (A) Schematic of *s*-polarized (top) and *p*-polarized (bottom) WSM illumination. (B) Optical images of nanohole arrays with *s*-polarized (top) and *p*-polarized (bottom) WSM illumination produced using polarization optics placed at the input to the waveguide. The incomplete suppression of light scattering in the *p*-polarized configuration most likely results from *s*-polarized light generated by scattering off the edges and surfaces of the waveguide.

WSM images of the nanohole arrays show two distinct colors from the horizontal and vertical polarization conditions (Figure 3.9C). Scattering spectra collected in these two conditions (Figure 3.9D) show distinct scattering resonances located at ∼600 nm for the vertical polarization and 750-850 nm for the horizontal polarization. This result confirms that the direction of the input wavevector, k, in WSM can be used to produce polarization-resolved imaging and scattering spectra from anisotropic plasmonic nanostructures. Furthermore, it highlights the similarity of the data produced by WSMwithout polarization opticsto the data collected with more conventional polarization optics.[133–135]

3.3 Waveguide Photovoltaics

Conventional solar cells utilize vertical illumination, wherein the path length available for absorption is dictated by the thickness of the solar cells. The use of back reflectors and antireflective coatings has been implemented in an attempt to minimize light loss and maximize light absorption in these solar cells, but scattering, reflection, and transmission limit their real-world efficiencies.

A fundamentally different illumination geometry is emerging to bypass these processes illumination via a waveguide[136] (Figure 3.11A). In such a geometry, light is coupled into a dielectric, transparent waveguide, such as an optical fiber, at a high angle and, through total internal reflection, retained within the waveguide. In the near-field, an evanescent wave decays away from the surface of a waveguide

without absorption, so long as it does not interact with any other objects. When photoabsorbing materials are placed on the surface of the waveguide, they interact with the evanescent wave, either absorbing or scattering some of the light. Any light that does interact with the photoabsorber continues to be transmitted within the waveguide. It has been demonstrated that this geometry can significantly enhance the energy conversion efficiency of nanostructured solar cells. [137]

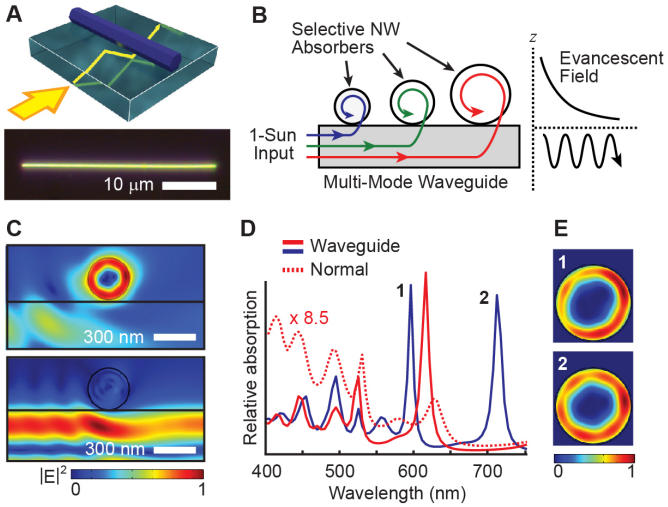

Figure 3.11: Waveguide Photovoltaics.(a) Schematic of waveguide illumination and the total internal reflection of light (top) and image of nanowire under waveguide illumination (bottom) (b) Illustration of the selective interaction of nanowires with certain wavelengths of light, while letting others continue within the waveguide (c) Optical simulations of a waveguide with a NW 300 nm in diameter showing coupling at an on-resonance wavelength (710 nm; upper image) and off-resonance wavelength (435 nm; lower image). (d) Simulations of relative absorption under transverse magnetic illumination for a NW 250 nm in diameter under normal incidence (dashed red; scaled by 8.5x) and waveguide illumination (solid red) and NW 300 nm in diameter under waveguide illumination (blue). (e) The power loss density within the 300nm TM wire at the maximal absorption wavelengths: 595nm (1) and 710nm (2).

Nanowires are well suited as waveguide photoabsorbers since their radial dimensions are comparable to the decay length of the evanescent field (wasting no material) and their dimensions and orientations are controllable. Figure 3.11B shows a schematic illustrating how nanowires can selectively interact with light of different wavelengths while allowing other wavelengths to be passed on to other wires. The ability of NWs to interact with particular wavelengths is dictated primarily by their diameter and orientation relative to the electric field of the incoming light. When light is passed into a slab waveguide, its electric field is oriented along one axis, so the orientation of the wire on the waveguide determines its orientation relative to the electric field. Figure 3.11D shows optical simulations that compare the relative

absorption of 250nm wires in normal incidence and waveguide illumination geometries as well as several other diameters under waveguide illumination. These results highlight both the spectral tunability, even into the red, and absorption enhancement of the waveguide geometry, as the normal incidence results must be scaled up to be comparable to the waveguide results. A combination of wires with different spectral selectivities, based on diameter and orientation, will produce an efficient array for the absorption of waveguided light. In addition, alterations made to decrease the scattering of these wires will further enhance total light absorption.

3.4 Conclusions

Conventional DFM has proven to be a valuable tool for the study of plasmonic and photonic nanostructures. WSM represents a complementary dark-field technique that can have advantages over conventional methods, is easily implemented with standard microscopy equipment, and is well-suited for nanostructures fabricated on planar substrates. The elimination of in-objective illumination in favor of waveguide illumination permits the use of higher numerical-aperture objectives and the collection of higher resolution images. In addition, the evanescent field illumination reduces background scattering and produces higher contrast dark-field images. WSM also provides a consistent illumination geometry across varying instruments, which can eliminate variations in the spectroscopic data collected from similar samples. The waveguide also allows for polarization-controlled illumination using the direction of the incident wavevector, enabling the selective excitation of specific dielectric and metallic scattering resonances. WSM is thus a straightforward and versatile addition to any microscopy apparatus and allows for efficient imaging and spectroscopic analysis of photonic and plasmonic nanostructures.

ENCODING HIGHLY NONEQUILIBRIUM BORON CONCENTRATIONS AND ABRUPT MORPHOLOGY IN P-TYPE/N-TYPE SILICON NANOWIRE SUPERLATTICES

"Everything must be made as simple as possible. But not simpler."

- Albert Einstein

4.1 Introduction

The bottom-up synthesis of nanomaterials, such as semiconductor nanowires (NWs) grown by the vapor-liquid-solid (VLS) mechanism, allows for precise control of composition and doping, which enables the creation of nanoscale technological devices such as solar cells,[12,31,56,58] photodiodes,[64] thermoelectric devices,[138–142] and field-effect transistors.[143–147] Device characteristics need not be controlled by composition alone, however, as morphological control at the nanoscale can also be used to modify photonic, electronic, and thermal characteristics. In the case of silicon (Si) NWs, *in situ* dopant modulation[11,21] or gold (Au) surface deposition,[70,148] in combination with wet-chemical etching, can be used to modulate the radial dimensions of NWs, introducing structure that can be varied along the NW axis.16 The dopant-controlled process is termed ENGRAVE (Encoded Nanowire GRowth and Appearance through VLS and Etching) and has been reported only for phosphorus (P)-doped n-type silicon (Si) segments, in which a degenerate P doping level either impedes or enhances the etch rate of the NW.[11] Although it is known for bulk Si that boron (B)-doped p-type silicon can also modulate etching,[149,150] this effect has been noticeably absent[56,148] in prior reports on p-type VLS-grown Si NWs. This absence can be attributed to a substantially lower B doping level compared to P-doped NWs grown

This chapter reproduced with permission from Hill, D. J.; Teitsworth, T. S.; Kim, S.; Christesen, J. D.; Cahoon, J. F. Encoding Highly Nonequilibrium Boron Concentrations and Abrupt Morphology in P-Type/N-Type Silicon Nanowire Superlattices. *ACS Appl. Mater. Interfaces* **2017**, *9*, 37105-37111. Copyright 2017 American Chemical Society.

under the same conditions,[56] and this low doping level has, for instance, prevented the realization of fully VLS-grown Esaki diodes.[151]

Conventionally, degenerate doping levels in bulk semiconductors are achieved either by using high temperatures,[34,152] which increase the solid solubility of the dopant, or by using a nonequilibrium process such as laser annealing,[35,36] which kinetically traps dopant atoms in the material at a concentration above the solid solubility limit. However, for Si VLS growth, nonequilibrium dopant concentrations above the solid solubility limit have been reported when using a metal catalyst that can also serve as a dopant.[40,153] For instance, in the case of both aluminum[40] and indium/tin[153] catalyzed growth, the group III element was observed to be incorporated in the NW at a concentration 2 orders of magnitude or more above the solid solubility limit, which could be attributed to kinetic trapping of catalyst atoms at the liquid-solid interface.

In addition to control of the absolute doping level, control over the axial and radial spatial distribution of dopants within the NW is desired. In the radial direction, higher temperatures that may favor higher dopant incorporation also cause the decomposition of the Si precursor silane (SiH_4),[154] leading to the nonselective vapor-solid (VS) growth of a silicon shell on NW sidewall. B also serves to catalyze the decomposition of SiH_4,[155] further exacerbating the problem for p-type growth. VS shell growth can lead to substantial tapering of NWs and undesired doping in the radial direction, screening the underlying electronic structure[27,155,156] and prohibiting wet-chemical etching. However, the use of gas-phase additives that can passivate or etch the NW surface have been shown to reduce VS growth in both Ge[33,157] and Si[158,159] NWs.

For dopant spatial distributions in the axial rather than radial direction, a common problem encountered during VLS growth is the reservoir effect, in which compositional changes are broadened because the liquid catalyst serves as a reservoir of material even after the vapor-phase source is removed, blurring the transition.[27,72,156] Although the reservoir effect can prevent the production of well-defined morphologies through the ENGRAVE process, recent work has shown that the effect can be suppressed if other catalyst depletion modalities, such as evaporation or sidewall diffusion of the precursor material,[28,160] occur faster than NW growth.

Here, we describe the synthesis of degenerately doped p-type and n-type segments in Si NWs using HCl to chlorinate the NW sidewall and stabilize VLS growth at temperatures from 500 to 700 °C. Under these conditions, we find the doping level of B-doped segments to be at least 1 order of magnitude greater

than the solid solubility limit. Moreover, transitions between p-type, intrinsic, and n-type segments are abrupt, enabling the creation of complex morphology in p-n junctions that can be used for a range of technological applications.

4.2 Results and Discussion

p-Type NW Growth. NWs were grown in a home-built, hot-wall chemical vapor deposition (CVD) system, utilizing hydrogen (H_2) as the carrier gas, SiH_4 as the Si source, HCl as the Cl source, and diborane (B_2H_6) and phosphine (PH_3) as B and P sources, respectively (see Methods for growth details). We explored the relationship between temperature and HCl:SiH_4 ratio and observed four growth regimes, as illustrated in Figure 4.1A, which yielded the characteristic NW morphologies shown by the images in Figure 4.1B. In region I, where the HCl flow is low and the temperature is below 700 °C, we observe stable NW growth with significant VS shell growth, resulting in tapered NWs with bases thicker than the original catalyst diameter. In region III, higher HCl flow rates over the same temperature regime slow NW growth, producing either shorter NWs or no NWs at all. Between these two regimes is region II, in which reliable NW nucleation and stable growth is achieved without significant VS overcoating, resulting in cylindrical NWs. Above 700 °C, in region IV, we observe unstable NW growth, in which the Au catalyst shrinks in diameter over time, resulting in a diameter change of $\sim$1 nm/μm of growth.

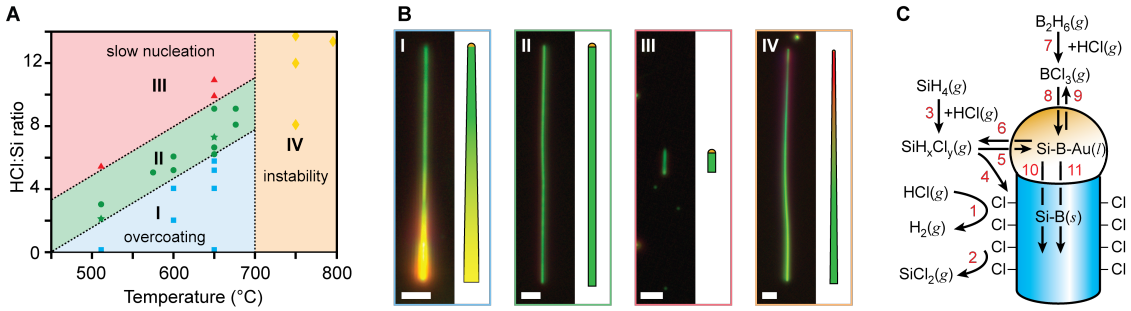

Figure 4.1: p-type NW growth conditions. (A) Qualitative analysis of p-type NW growth conditions, illustrating four regimes, overcoating (I), optimal (II), slow nucleation (III), and instability (IV), that depend on temperature and HCl:SiH_4 ratio. Conditions used for further experiments are marked with a star. (B) Dark-field microscopy images (left) and schematics (right; not to scale) exemplifying NWs grown in regimes I-IV, as indicated in panel A; scale bars, 4 μm. (C) Schematic of the microscopic chemical processes that can occur during p-type NW VLS growth with Au catalysts using HCl, B_2H_6, and SiH_4 precursor gases.

The known temperature-dependent kinetics of Si chlorination [161–163] provide a basis for understanding the origin of the different growth regimes by considering the microscopic reactions illustrated in Figure 4.1C. Labile chlorine atoms introduced to a Si surface react with dangling bonds to produce $SiCl_x$ surface species (Figure 4.1C, reaction 1). Si surfaces exhibit only monochlorinated species when the surface concentration is below ~60% of surface site saturation or when the temperature is above 400 °C.40 Monochlorinated surface species are optimal for surface passivation because multiply chlorinated species, such as $SiCl_2$, can desorb from the surface and etch the NW (reaction 2). HCl has been shown to chlorinate silicon surfaces less effectively than Cl_2 at low temperatures, [162] making it less likely to form the multiply chlorinated species required for etching and thus more suitable for surface passivation. This surface chlorination then provides a barrier to VS deposition [158,159] (reaction 4), as observed in prior studies. [70,158,159]

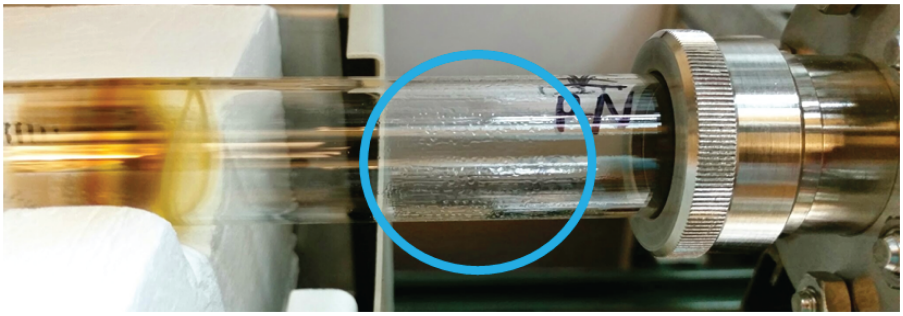

Figure 4.2: Production of multiply chlorinated silanes. An image of the downstream end of the reactor tube after a reaction containing HCl and SiH_4 at 800 °C. A condensate appeared in the cool region of the reactor in reactions above 700 °C, which oxidized on exposure to air. $SiHCl_3$ and $SiCl_4$ are liquid at room temperature, but SiH_4, SiH_3Cl, and SiH_2Cl_2 are not. The absence of these condensates at reaction temperatures below 700 °C suggests that gas phase chlorination of the silane feed gas scales with temperature.

Si chlorination can also occur in the gas phase (see Figure 4.21), converting the silane into chlorosilane species (reaction 3). As the relative concentration of HCl is increased, the equilibrium will be driven toward multiply chlorinated, less reactive chlorosilanes like $SiCl_4$, slowing both VS deposition and catalyst incorporation [70] (reaction 5). Region I, which exhibits VS deposition, likely results from insufficient Si chlorination on the surface and/or in the gas phase. Low chlorination in the gas phase may yield a high concentration of the more reactive silanes, which promote VS deposition. Alternatively, depletion of the HCl concentration through gas phase reactions may leave insufficient HCl present for surface

chlorination. In either case, increasing the HCl concentration will overcome the VS deposition. Region III, in contrast, likely results from excessive chlorination in the gas phase, which impedes nucleation and growth of the NW. The instability in region IV, on the other hand, can likely be explained by a loss of Cl surface passivation, which is known to result in the loss of Au from the catalyst.[70,158,159] Surface passivation has also been shown to directly influence the stability of a liquid Au eutectic catalyst.[164] $SiCl_2$ is the primary species through which Cl leaves the Si surface above 500 °C, and it exhibits a desorption peak at 677 °C. Above 777 °C, no Cl is observed to remain on the Si surface;[163] thus, the instability observed in region IV is well explained by Cl desorption from the NW surface. Region II represents optimal chlorination, where VS growth is prevented and VLS growth is allowed, and sidewall stabilization keeps the catalyst intact. Unless noted otherwise, NWs used in this work were grown at 650 °C with an HCl:SiH_4 ratio of 7. These wires exhibit an $\sim$10 nm change in diameter over 60 μm length scales. This slow change in diameter likely results from the loss of Au from the catalyst to the NW sidewalls, as demonstrated previously[70] and observed in Figure 4.7. Thus, these optimized conditions demonstrate the effectiveness of HCl in stabilizing NW growth and preventing VS deposition.

4.2.1 p-Type Etching

Using optimized p-type NW growth conditions (region II in Figure 4.1A), we can evaluate the etch characteristics of the B-doped NWs in aqueous potassium hydroxide (KOH) solution (see Methods for details). By rapidly modulating the dopant flow as the wire is growing, we can encode specific doping levels along the NW axis, as shown by the dopant profile and scanning electron microscopy (SEM) image in Figure 4.3A. This NW consists of segments encoded (reflecting the B:Si ratio in the gas phase) at $5.7x10^{21}cm^{-3}$ alternated with segments of varying doping level, from nominally intrinsic (I) to $1.1x10^{21}cm^{-3}$ (VI). We determined the etch rate at room temperature as a function of the encoded doping level by measuring the diameter reduction of the NWs (see Methods for details). We observed nominally intrinsic silicon to etch at a rate of $\sim$45 nm/min, and the etch rate decayed as the encoded doping level increased. In Figure 4.3B, the measured etch rate is plotted against the encoded doping level and the B_2H_6 flow rate. At moderate doping levels, etched segments show surface roughness as well as faceting that persists at high doping levels. This suggests that the B may partially self-segregate to particular crystal facets,[165] though further research is required to examine this point in detail. Above an

encoded doping level of $1.4x10^{21}cm^{-3}$, the NWs did not exhibit a measurable diameter reduction after etching for 2 min at room temperature.

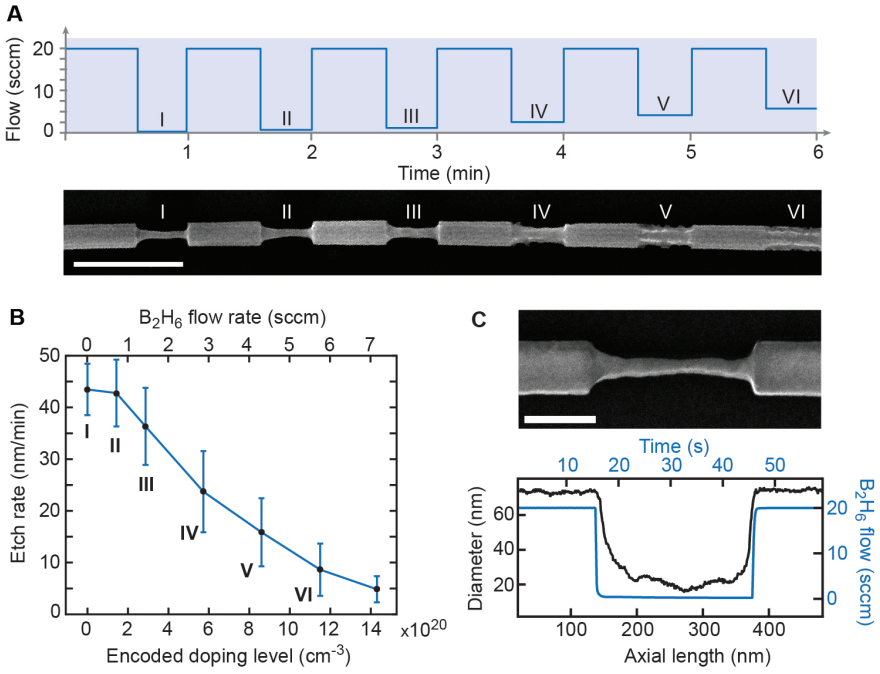

Figure 4.3: Wet-chemical etching of p-type modulation doped NWs. (A) Upper: schematic of B_2H_6 flow during NW growth. Lower: SEM image of an etched NW with segments, denoted by Roman numerals, encoded at doping levels of 0 (I), $1.4x10^{20}$ (II), $2.9x10^{20}$ (III), $5.7x10^{20}$ (IV), $8.6x10^{20}$ (V), and $1.1x10^{21}cm^{-3}$ (VI). Large diameter segments correspond to an encoded doping level of $5.7x10^{21}cm^{-3}$; scale bar, 500 nm. (B) Plot of the NW etch rate at room temperature in aqueous KOH solution as a function of the encoded doping level (lower axis) or the B_2H_6 flow rate (upper axis). (C) Upper: SEM image of an etched p-i-p profile, showing where B_2H_6 is removed (left) and reintroduced (right); scale bar, 100 nm. Lower: graph illustrating the diameter profile as a function of axial length (lower and left-hand axes) and the encoded B_2H_6 flow as a function of time (upper and right-hand axes). The asymmetry in the etch profile shows the extent of the reservoir effect.

The diameter profile of individual etched structures provides insight into the abruptness of the dopant profile. An SEM image and diameter profile of an etched p-i-p NW segment plotted against the recorded B_2H_6 flow profile are shown in Figure 4.3C. The transition on the right-hand side (i.e., the i-p transition), which reflects the reintroduction of B_2H_6 and is not expected to display a reservoir effect, exhibits an abrupt transition (length $<<$ diameter) with a characteristic length of 6.8 ± 0.7 nm. The transition on the left-hand side (i.e., the p-i transition), which reflects the termination of B_2H_6 flow, is expected to

exhibit an elongated profile relative to the gas-phase precursor flow if the reservoir effect is substantial.[28] This p-i transition exhibits a length of 20 $\pm$ 1 nm, which is $\sim$3-fold longer than the i-p transition. This difference implies that there is a B reservoir effect, but the magnitude of the effect is relatively minimal and the length scale is substantially less than the NW diameter of $\sim$76 nm. We postulate that the B in the catalyst may be removed by a mechanism other than incorporation into the NW, such as by the evaporation of boron trichloride (Figure 4.1C, reaction 9).

4.2.2 p-Type Doping Level

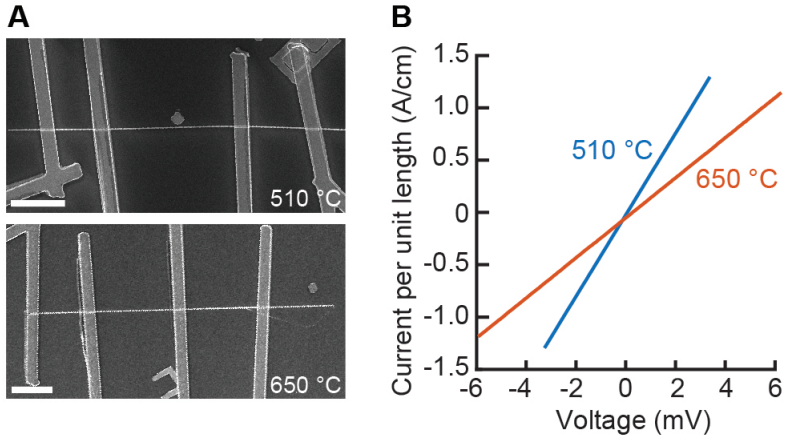

Figure 4.4: p-type NW electrical transport properties. (A) SEM images of devices for four-point probe measurements, showing p-type NWs grown at 510 °C (upper) and 650 °C (lower); scale bars, 5 m. (B) Four-point-probe conductivity measurements collected from p-type NWs grown at 510 °C (blue) and 650 °C (orange) at an encoded doping level of $410^{21} cm^{-3}$. Current values were multiplied by the NW length between the inner Ohmic contacts and divided by the NW cross-sectional area, so the slope directly reflects the conductivity of the NW.

To determine the active doping level of these NWs, we fabricated Ohmic contacts to p-type NWs grown at 650 and 510 °C doped with an encoded B doping level of $4x10^{21} cm^{-3}$. We measured the NW resistivity through a four-point-probe configuration (see Methods), as shown by SEM images in Figure 4.4A and the transport measurements in Figure 4.4B. On the basis of the empirical relationship between resistivity and doping level for bulk silicon,[166] which accounts for the decrease in mobility at increased doping levels, we find the active doping level of wires grown at 650 °C to be $\sim 2x10^{19} cm^{-3}$ based on measurements from several NWs (see 4.1) and assuming a uniform dopant distribution in the NWs. Although nonuniform dopant distributions have often been observed in the literature,[156,165,167] we

note that the CVD conditions in this study are distinct from prior studies and have been optimized to facilitate highly stable VLS growth without VS deposition; thus, we do not necessarily expect the same nonuniform distribution to be present for the NWs in this study. Upon decreasing the encoded doping to $2x10^{21}cm^{-3}$, we found no change in the active doping level, indicating that the dopant incorporation process has saturated. However, this active doping level is approximately twice the solid solubility limit of B in Si at 650 °C ($\sim 1x10^{19}cm^{-3}$).[34] Nevertheless, it is slightly more than 2 orders of magnitude lower than the encoded gas-phase ratio of the dopant atoms, indicating that substantially fewer B atoms are active in the NW than are supplied in the gas phase. Although the active doping level for these p-type NWs is comparable to what has been determined previously for P-doped n-type NWs,[28] the difference between the encoded and active doping level is about 1 order of magnitude larger for p-type NWs than for n-type NWs. Moreover, NWs grown at 510 °C exhibited an active doping level of $\sim 4.5x10^{19}cm^{-3}$, more than twice the active doping level achieved at 650 °C, as apparent from the steeper slope of the line for 510 °C in Figure 4.4B. This active doping level is more than 1 order of magnitude larger than the extrapolated solid solubility limit of B in Si at 510 °C ($\sim 3x10^{18}cm^{-3}$).[34] Thus, the active doping level in B-doped NWs under these conditions apparently increases at lower temperatures, which is surprising and the opposite result from what is expected from bulk Si doping processes.

Temperature (°C)	Diameter (nm)	Length (nm)	Resistance ($k\Omega$)	Encoded Doping Level (cm^{-3})	Measured Doping Level (cm^{-3})
650	111	10079	56.13	$2.00x10^{21}$	$1.95x10^{19}$
	93	9941	82.73	$2.00x10^{21}$	$1.84x10^{19}$
	117	15348	72.72	$2.00x10^{21}$	$2.08x10^{19}$
	123	14678	64.48	$2.00x10^{21}$	$2.03x10^{19}$
	123	15094	64.87	$2.00x10^{21}$	$2.08x10^{19}$
	103	12670	80.95	$4.00x10^{21}$	$1.95x10^{19}$
	113	19876	104.3	$4.00x10^{21}$	$1.99x10^{19}$
	105	14076	89.29	$4.00x10^{21}$	$1.91x10^{19}$
510	105	8286	19.92	$4.00x10^{21}$	$5.64x10^{19}$
	106	11430	33.21	$4.00x10^{21}$	$4.43x10^{19}$
	101	7779	25.09	$4.00x10^{21}$	$4.43x10^{19}$
	101	7794	24.50	$4.00x10^{21}$	$4.63x10^{19}$
	84	14152	56.05	$4.00x10^{21}$	$5.35x10^{19}$
	96	6649	27.95	$4.00x10^{21}$	$3.75x10^{19}$
	90	6633	31.82	$4.00x10^{21}$	$3.63x10^{19}$

Table 4.1: Resistivity Measurements of p-type NWs

In addition to the active doping level, we also attempted to quantify the amount and spatial uniformity of B incorporated into the NWs (i.e., the chemical doping level) utilizing X-ray photoelectron spectroscopy (XPS), energy-dispersive X-ray spectroscopy (EDS), and electron energy loss spectroscopy (EELS). Because of the low atomic number, low electron binding energy, and low X-ray fluorescence yield of B, we were unable to accurately quantify the B content of the NWs (see Figures 4.5, 4.6, and 4.7). On the basis of the limits of quantification for these techniques, however, we estimate that the incorporated B concentration is less than $\sim 1x10^{20}cm^{-3}$ even when the encoded doping level is $4x10^{21}cm^{-3}$. Thus, we can infer that B is incorporated in the NW at a B:Si ratio that is at least 100-fold lower than the gas-phase B:Si ratio and that 20% or more of the B dopants incorporated in the NW are electrically active.

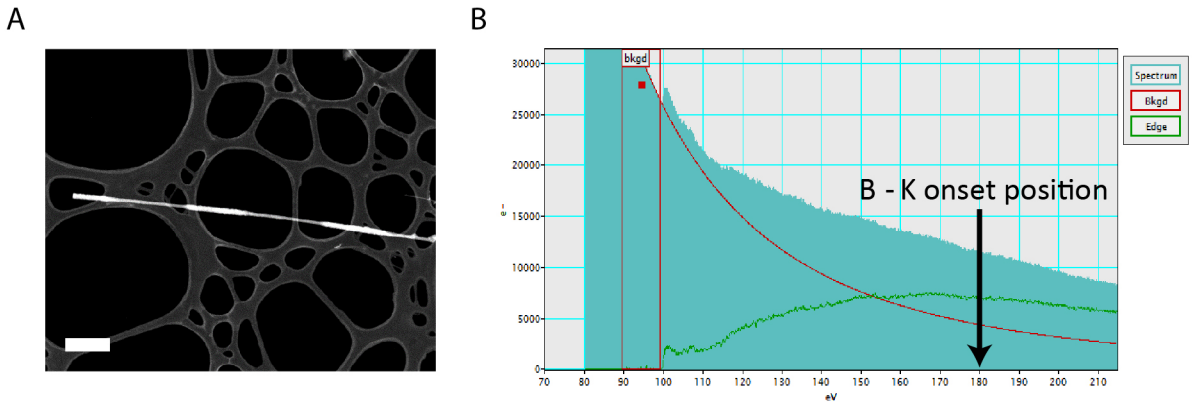

Figure 4.5: EELS Characterization. Electron energy loss spectroscopy of doped nanowires at 200 kV and 100 pA. (A) TEM image of a doped and etched p-i-p structure; scale bar 500 nm. (B) Resultant spectrum from a doped region. The Si background appears to overwhelm any B signal.

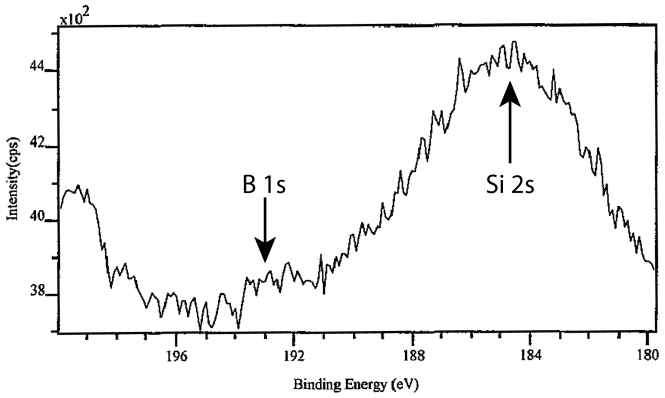

Figure 4.6: X-ray photoelectron spectroscopy characterization of B-doped Si NWs grown on indium-doped tin oxide. The B 1s was not sufficiently distinguishable from the Si 2s line shape to quantify the B content.

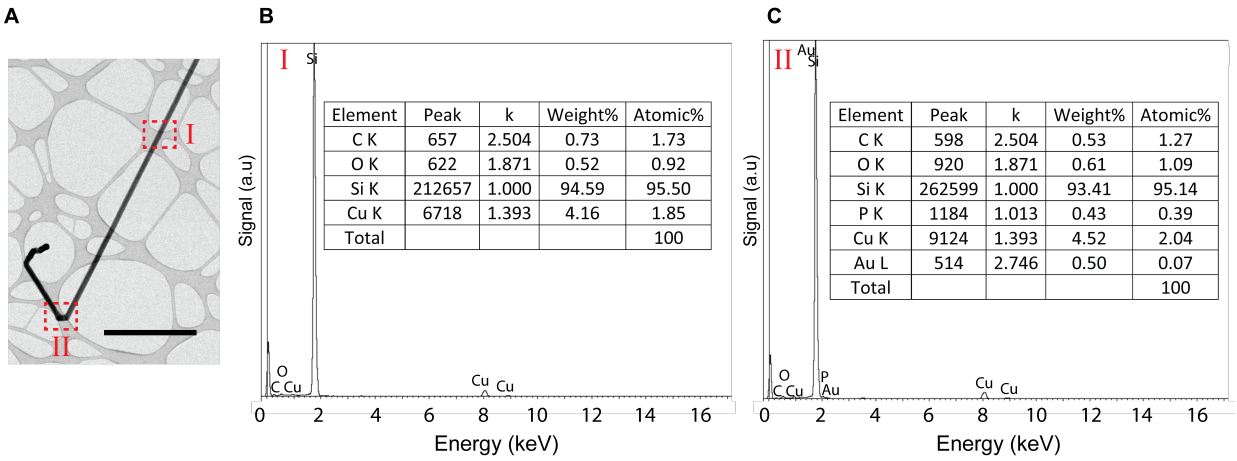

Element	Peak	k	Weight%	Atomic%
C K	657	2.504	0.73	1.73
O K	622	1.871	0.52	0.92
Si K	212657	1.000	94.59	95.50
Cu K	6718	1.393	4.16	1.85
Total				100

Element	Peak	k	Weight%	Atomic%
C K	598	2.504	0.53	1.27
O K	920	1.871	0.61	1.09
Si K	262599	1.000	93.41	95.14
P K	1184	1.013	0.43	0.39
Cu K	9124	1.393	4.52	2.04
Au L	514	2.746	0.50	0.07
Total				100

Figure 4.7: EDS Characterization. (A) Transmission electron microscope image of a modulation-doped nanowire; scale bar, 2 m. (B) Energy dispersive x-ray spectrum of a p-type nanowire segment, collected from the dashed box region denoted I in panel A. Neither B nor Au were detected in this region. Inset: table of weight percentages and atomic percentages for various elements detected in the spectrum. (C) Energy dispersive x-ray spectrum of an n-type nanowire segment, collected from the dashed box region denoted II in panel A. Inset: table of weight percentages and atomic percentages for various elements detected in the spectrum. Au detection in this region was variable, being below or just above the limit of detection ($\sim$0.05 at. %) at different points.

The measurement of active B doping levels well above the solid solubility limit, as well as the unexpected temperature dependence, suggests that the doping levels are strongly dictated by the kinetics of B and Si incorporation into the catalyst (Figure 4.1C, reactions 5 and 8), causing a nonequilibrium concentration of B to be kinetically trapped in the NW. The temperature-dependent results can be explained if the B incorporation reaction begins to saturate at or below 510 °C while the Si incorporation reaction continues to increase with temperature. This dependence of doping level on the rates of the microscopic incorporation processes, as described previously assuming a hemispherical liquid catalyst of radius r,[28] is given by

$$N_A = \frac{k_{BC}C_{BC}\pi r^2\Omega_B}{k_{SiC}C_{Si(l)}\pi r^2\Omega_{Si}} \approx \frac{k_{BC}C_{BC}}{k_{SiC}C_{Si(l)}} \tag{4.1}$$

where N_A, the total doping level defined as the ratio of B to Si, is given by the ratio of the rates of B crystallization and Si crystallization at the liquid-solid interface (Figure 4.1C, reactions 11 and 10) in the numerator and denominator, respectively. These rates depend on their respective crystallization rate

constants, k_{BC} and k_{SiC}, as well as the concentrations of the species in the liquid catalyst, $C_{B(l)}$ and $C_{Si(l)}$, and the atomic volumes, Ω_B and Ω_{Si}. By assuming $\Omega_B \approx \Omega_{Si}$, we simplify the expression in the right-hand side of eq 4.1 to depend only on the rate constants and concentrations. The steady-state concentration of each species depends on the rates of incorporation, evaporation, and crystallization, as shown for B:

$$\frac{dC_{B(l)}}{dt} = 0 = k_{BI}P_B\frac{S}{V} - k_{BE}C_{B(l)}\frac{S}{V} - k_{BC}C_{B(l)}\frac{A}{V} \tag{4.2}$$

where S is the surface area of the catalyst hemisphere-gas interface ($2\pi r^2$), A is the interfacial surface area between the catalyst and the wire (πr^2), k_{BI} is the B incorporation rate constant, and PB is the partial pressure of B in the reactor. A similar expression exists for Si. By solving for the liquid concentration and substituting into eq 4.1, we can define the total doping level as a function of microscopic rate constants and partial pressure:

$$N_A = \frac{k_{BC}k_{BI}(2k_{SiE} + k_{SiC})}{k_{SiC}k_{SiI}(2k_{BE} + k_{BC})}\frac{P_B}{P_{Si}} \tag{4.3}$$

Thus, the ratio of B to Si in the gas phase, given by $\frac{P_B}{P_{Si}}$, is modulated by the factor in eq 4.3 to give the final doping level in the NW, which is dictated by the kinetic rate constants of the respective reactions. We speculate that the barrier to B incorporation into the liquid catalyst might be substantially lower than that barrier to Si incorporation, causing the effective rate constant of B incorporation to saturate at high temperatures. The rate constant of Si incorporation does not saturate, as evidenced by the increase in NW growth rate from ∼1.6 to ∼13.2 nm/(min·mTorr) from 510 to 650 °C, respectively, where the growth rate is referenced to the partial pressure of SiH_4 in mTorr.

4.2.3 ENGRAVE Morphology in p-Type and n-Type NWs

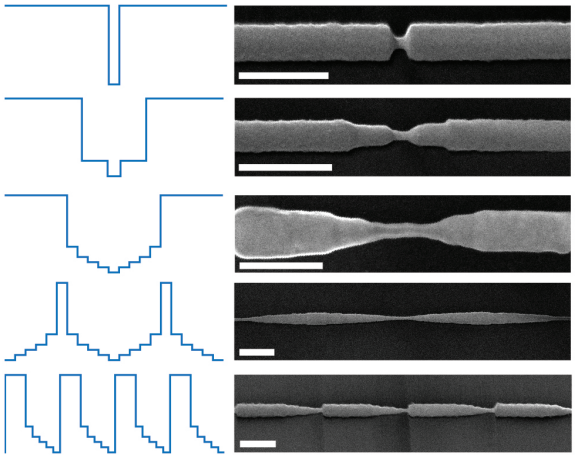

Figure 4.8: p-type ENGRAVE NWs. B2H6 dopant flow profiles (left) and SEM images (right) of various complex morphologies encoded through the ENGRAVE process at 650 C using the dependence of the Si etch rate on p-type doping level; scale bars, 200 nm.

We found that high quality p-type NWs with abrupt transitions could be encoded anywhere within region II of Figure 4.1A. Figure 4.8 displays a range of complex morphologies - including nanorods, bow ties, sinusoids, and sawtooths - encoded in p-type NWs at 650 °C using the ENGRAVE process, in which precisely chosen B doping levels encode a specific etch rate at every point along the NW growth axis. We also synthesized single NWs in which both p-type and n-type segments were encoded with complex morphology. However, we found that n-type segments exhibit a substantial reservoir effect at temperatures greater than ∼500 °C, as shown by the SEM images and diameter profiles in Figure 4.9A and 4.9B, respectively. We hypothesize that the appearance of a P reservoir effect at higher temperatures may result from hydrogen desorption from the liquid catalyst, inhibiting evaporation (associative desorption) of P as PH_3,[28] but determining the exact cause requires further experiments with careful control of surface chemistry. Nevertheless, we found that a growth temperature of 510 °C was optimal both for abrupt n-type and p-type transitions, permitting the synthesis of the high-resolution p-type/n-type superlattice structure shown in Figure 4.9C by an abrupt transition from p-type to n-type modulation-doped regions.

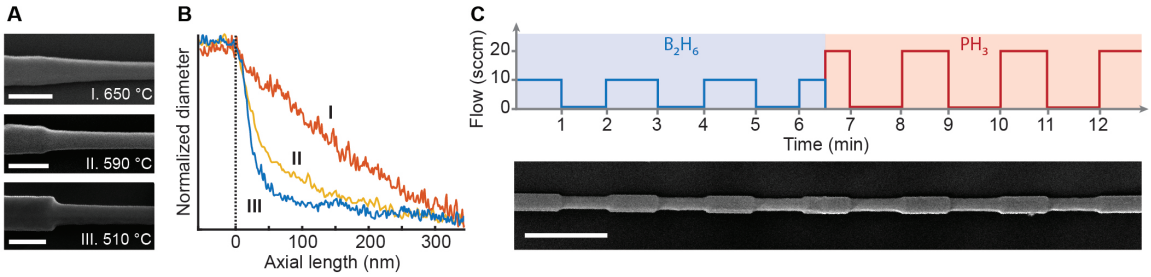

Figure 4.9: Abrupt dopants and morphology in p-type and n-type NWs. (A) SEM images of etched n-i dopant transitions at temperatures of 650 (I), 590 (II), and 510 °C (III); scale bars, 200 nm. (B) Diameter profiles derived from the SEM images in panel A illustrating the change in n-i transition length at 650 (I), 590 (II), and 510 °C (III). (C) Upper: B_2H_6 and PH_3 flow profiles during the growth of a p-type/n-type superlattice encoded as (p-i-p-i-p-i-p)-(n-i-n-i-n-i-n) at a temperature of 510 °C. Lower: SEM image of the p-type/n-type ENGRAVE nanowire encoded by the dopant profile shown above; scale bar, 500 nm.

4.3 Conclusions

We have demonstrated the synthetic conditions necessary for creating degenerately doped, linear, and uniform p-type Si NWs by using surface chlorination to passivate and stabilize VLS NW growth. The B doping level achieved is an order of magnitude above the solid solubility limit and is sufficient to provide an etch stop in alkaline solutions. Moreover, because doping level can be rapidly modulated with a minimal reservoir effect, the ENGRAVE technique can now be extended to p-type NWs, allowing the creation of p-n junctions with fully tunable morphology. The elucidation of the proper conditions for HCl-stabilized growth and the ability to encode morphology into both p-type and n-type NW segments provide new techniques for the synthesis of advanced optoelectronic NW devices.

INTERPLAY OF SURFACE RECOMBINATION AND DIODE GEOMETRY FOR THE PERFORMANCE OF AXIAL *P-I-N* NANOWIRE SOLAR CELLS

"Science, my lad, is made up of mistakes, but they are mistakes which it is useful to make, because they lead little by little to the truth."

- Jules Verne, *A Journey to the Center of the Earth*

5.1 Introduction

Nanowires (NWs) have garnered substantial attention for the unique properties and technological applications that are made possible by their nanoscale radial dimensions and high anisotropy. The bottom-up vapor-liquid-solid (VLS) growth of NWs allows for precise dopant[28,168,169] and morphological[11,21,170] profiles to be encoded along the axial dimension, permitting the creation of various active and passive device elements.[171,172] For instance, well-controlled syntheses can produce polytypic interfaces,[173] compositional heterostructures,[63,66] and plasmonic resonators[160] with interfaces defined on the single- to sub-nanometer scale in the best cases. Perhaps the most fundamental device element is the *p-n* junction, and numerous reports on NW axial *p-n* or *p-i-n* junctions have enumerated the conditions for producing the structures in both group IV[31,56,78,174,175] and III-V[57–59] materials. Devices including light-emitting diodes,[66,67] photodetectors,[63–65] and solar cells[31,56–62] have been demonstrated; however, the characteristics of these devices depends strongly on the geometry and precision of dopant profiles encoded during synthesis.

A key challenge for *p-n* or *p-i-n* NWs has been precisely controlling the diode geometry, which requires control of the doping level and dopant profile in both axial and radial directions. Several techniques have been used to characterize these quantities, which influence the performance of the diode.

"Reproduced with permission from ACS Nano, submitted for publication. Unpublished work copyright 2018, American Chemical Society."

For instance, dopant elemental profiles can be reconstructed using atom-probe tomography[68] and mapped using energy-dispersive x-ray spectroscopy in transmission electron microscopes.[28,70] Photoluminescence and cathodoluminescence[71] maps can reveal the composition and doping in direct-band gap materials while scanning photocurrent microscopy[74,78,79] and electron beam induced current can map the position of junctions and charge carrier diffusion lengths.[80] In addition, Kelvin probe force microscopy[27,74–76] can map potential changes within the NW that result from the dopant profile, and electron holography can map potential changes and space charge regions within the NW.[72,73] Scattering-scanning near-field optical microscopy (s-SNOM),[77] as used herein, can detect dopant profiles through local free-carrier terahertz absorption.

In addition to the evaluation of dopant and electrostatic profiles, the photovoltaic (PV) performance of NW axial *p-i-n* junctions has been evaluated theoretically[84–86,88,176] as well as in devices composed of single-NWs and large-area NW arrays. In devices, it has been shown that a reduction in surface recombination results in significantly improved performance, boosting both photocurrent and photovoltage.[59,78–80,82,177] Though recombination may place an upper bound on device performance, it is not the sole determinant. It has been shown that in some cases, low values of the surface recombination velocity (S) of up to $\sim 10^3$ cm/s have a negligible effect on device performance.[85,86] Moreover, the performance of *p-i-n* Si NWs has been observed to be strongly dependent on the diode geometry, with longer intrinsic regions corresponding to improved performance.[56] In addition, the internal quantum efficiency (IQE) within the intrinsic region of NWs has been observed to be relatively weakly dependent on S.[84] Here, we systematically explore the connection between diode geometry (i.e. radius and intrinsic length) and surface recombination, which together dictate nearly every PV parameter. We first discuss a theoretical analysis of the PV performance using an analytical model and finite-element simulations. Second, we compare these prediction of PV performance to experimental device measurements on single NWs with various geometries and well-defined dopant profiles, as verified by s-SNOM. The results elucidate the complex and sometimes counterintuitive connection between surface recombination and diode geometry of NW *p-i-n* junctions, providing guidelines for the evaluation and design of high-performance devices.

5.2 Results and Discussion

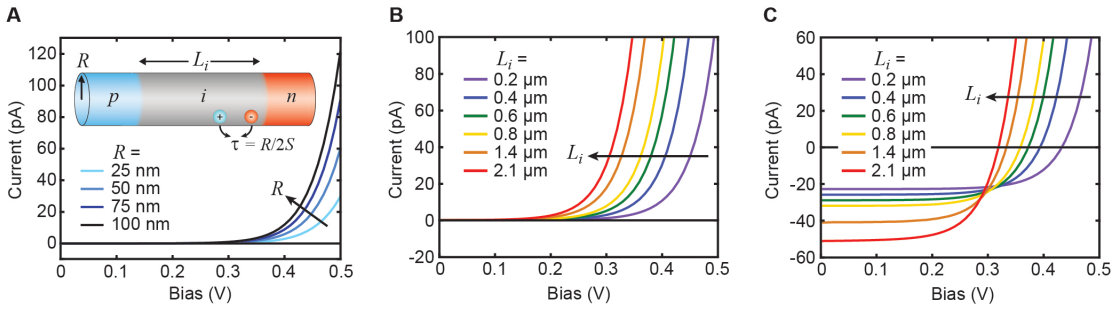

Figure 5.1: Simulated *I-V* characteristics of axial *p-i-n* NW devices. (A) Simulated dark *I-V* curves for R ranging from 25 to 100 nm with S of 200 cm/s and L_i of 1 μm. Inset: schematic of the geometrical and recombination parameters of an axial *p-i-n* junction. (B) Simulated *I-V* curves in the dark for R = 110 nm, L_i ranging from 0.2 to 2.1 μm, and S of 2,000 cm/s. (C) Simulated *I-V* curves under 1-sun illumination for R = 110 nm, L_i ranging from 0.2 to 2.1 μm, and S = of 2,000 cm/s.

5.2.1 Theoretical Analysis

We consider the device physics of the axial *p-i-n* structure (inset of Figure 5.1A) in the limit where recombination within the depletion region dominates the overall recombination current of the diode. Beginning with the standard equation for volumetric Shockley-Read-Hall recombination via a mid-band state,[178]

$$R_{SRH} = \frac{pn - n_i^2}{\tau_{SRH,n}(p + n_i e^{\frac{E_i - E_T}{k_B T}}) + \tau_{SRH,p}(n + n_i e^{\frac{E_T - E_i}{k_B T}})}, \tag{5.1}$$

where p and n, are the hole and electron concentrations, n_i is the intrinsic carrier concentration, E_i is the intrinsic Fermi level energy, E_t is the trap state energy, and τ is the electron or hole lifetime, we can interpret surface recombination in the same form. Assuming initially a distribution of surface trap states D, the surface recombination can be expressed as

$$R_S = \int_{E_V}^{E_C} \frac{pn - n_i^2}{\frac{p + n_i e^{\frac{E_i - E_T}{k_B T}}}{S_n(E_t)} + \frac{n + n_i e^{\frac{E_T - E_i}{k_B T}}}{S_p(E_t)}}, \tag{5.2}$$

where S_n and S_p are the electron and hole surface recombination velocities, respectively. If, as with SRH recombination, we assume a single mid-band state, eq. 5.2 reduces to

$$R_S = \frac{pn - n_i^2}{\frac{p+n_ie^0}{S_n} + \frac{n+n_ie^0}{S_p}}, \tag{5.3}$$

which gives recombination per unit area. In assuming a cylindrical geometry, we can formulate surface recombination in volumetric terms via the ratio of surface area to volume in an infinite cylinder:

$$R_S = \frac{2\pi RL}{\pi R^2 L} \cdot \frac{pn - n_i^2}{\frac{p+n_ie^0}{S_n} + \frac{n+n_ie^0}{S_p}} = \frac{2}{R} \cdot \frac{pn - n_i^2}{\frac{p+n_ie^0}{S_n} + \frac{n+n_ie^0}{S_p}} \tag{5.4}$$

Thus, surface recombination velocity can be reformulated into a lifetime, as in SRH recombination, for the depletion region:

$$R_D = \frac{p_D n_D - n_i^2}{\tau_n(p + n_i) + \tau_p(n + n_i)} = \frac{n_i(e^{\frac{qV}{2k_BT}} - 1)}{\tau_n + \tau_p} \tag{5.5}$$

If $p_D = n_D$ throughout the depletion region, the equation can be reduced to the right side of eq. 5.5. Solving for the majority carrier flux through the depletion region, it can be shown that

$$I = -qA\frac{W_d n_i}{\tau_n + \tau_p}(e^{\frac{qV}{2k_BT}} - 1) = \frac{-q\pi R^2 W_D n_i}{2\tau}(e^{\frac{qV}{2k_BT}} - 1) \tag{5.6}$$

where $A = \pi R^2$ for a cylinder, and assuming $\tau_n = \tau_p = \tau$. By solving the minority carrier diffusion equations, the current can be shown to match the classic ideal diode equation

$$I = -I_o(e^{\frac{qV}{2k_BT}} - 1). \tag{5.7}$$

By combining eq. 5.6 & 5.7, the dark saturation current, I_o, can be expressed as

$$I_o = q\pi R^2 W_D n_i / 2\tau = q\pi R L_i n_i S, \tag{5.8}$$

where *q* is elementary charge, *R* is the radius of the NW, W_D is the depletion width, n_i is the intrinsic carrier concentration at room temperature ($\sim 1.5x10^{10} cm^{-3}$ for Si), and τ is the effective recombination lifetime for both electrons and holes in the depletion region.[178] For NWs with relatively small R and non-negligible values of the surface recombination velocity *S*, τ can be expressed as $\tau = R/2S$, assuming the same value of *S* for electrons and holes.[78,179] Assuming the Shockley-Read-Hall lifetime is 1 μs or

greater, this approximation for τ should be nearly exact if the value of *S* is greater than ~50 cm/s for NWs ~250 nm or less in diameter. To expand the applicability to all semiconductors, direct band-to-band radiative recombination must also be considered. For simplicity, a version of eq. 5.5 can be used to represent the non-radiative recombination rate (R_{nr}), where $\tau_n = \tau_p = \tau$

$$R_{nr} = \frac{pn - n_i^2}{\tau(p + n + 2n_i)}. \tag{5.9}$$

Radiative recombination is described by

$$R_r = B(pn - n_i^2), \tag{5.10}$$

where B is the radiative recombination coefficient, with values of $\sim 10^{-15}$ cm^3/s for indirect band gap semiconductors and $\sim 10^{-10}$ cm^3/s for direct band gap semiconductors. As surface recombination dominates over SRH recombination in the NW geometry, the ratio of radiative to non-radiative recombination rates can be given by the ratio of band-to-band (eq. 5.10) to volumetric surface recombination (eq. 5.4) where $\tau = R/2S$

$$R_r/R_{nr} = \frac{B(pn - n_i^2)}{\frac{2S(pn-n_i^2)}{R(p+n+2n_i)}} = \frac{BR(p + n + 2n_i)}{2S}. \tag{5.11}$$

Assuming that $p = n$ reduces the ratio to

$$R_r/R_{nr} = \frac{2BR(n + n_i)}{2S} = \frac{BR(n + n_i)}{S}. \tag{5.12}$$

For an InP NW ($B = 1.2x10^{-10}$ cm^3/s, $n_i = 1.3x10^7$ cm^{-3}) with radius R = 100 nm and surface recombination velocity S = 100 cm/s, the ratio of radiative to non-radiative recombination is shown in Figure 5.2.

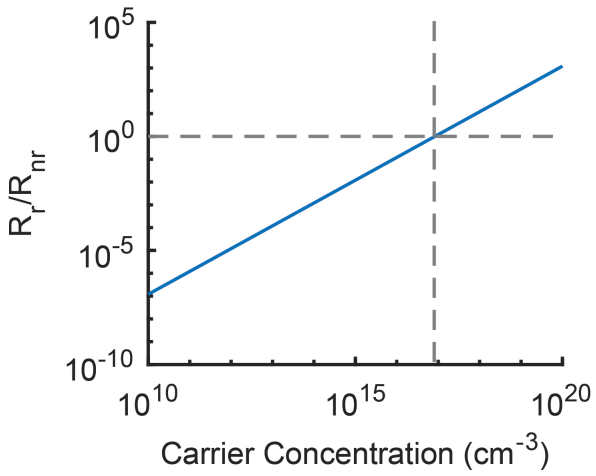

Figure 5.2: Radiative and non-radiative recombination. The ratio of the radiative recombination rate (R_r) to the non-radiative recombination rate (R_{nr}) as a function of carrier concentration for an InP NW with radius R = 100 nm and surface recombination velocity S = 100 cm/s.

For both direct and indirect band gap semiconductors, the surface recombination rate will far exceed the radiative recombination rate up to excess charge carrier densities of $\sim 10^{17} cm^{-3}$, and can thus be neglected with regard to the properties of the intrinsic region in this analysis. In addition, in the limit of degenerately-doped n-type and p-type segments, W_D can be approximated as the length of the intrinsic segment, L_i. Using these two approximations results in the expression on the right-hand side of eq. 5.8. Moreover, the value of *S* can be estimated from I_o and the geometrical parameters R and L_i by rearranging eq. 5.8 as:

$$S = I_o / q\pi R L_i n_i. \tag{5.13}$$

Interestingly, eq. 5.8 predicts that I_o is directly proportional to R and L_i while eq. 5.13 predicts that *S* is inversely proportional to both quantities. Thus, NWs with smaller radii or shorter L_i should exhibit a smaller I_o and thus relatively improved diode characteristics (e.g. a higher turn-on voltage) if *S* is constant. To validate these expressions, we compare the predictions of eqs. 5.8-5.13 to a previously developed finite-element simulation[84] that describes the full geometry and electrostatics of a Si *p-i-n* junction under the influence of drift, diffusion, charge-carrier generation, and recombination by surface and Shockley-Read-Hall mechanisms (see Methods for details). In Figure 5.1, simulated current-voltage (I-V) curves are shown for Si NW radii, R, ranging from 25 nm to 100 nm (Figure 5.1A) with fixed *S*

and L_i of 200 cm/s and 1 μm, respectively, and for L_i ranging from 0.2 to 2.1 μm (Figure 5.1B) with fixed S and R values 2,000 cm/s and 110 nm, respectively. As expected from eq. 5.8, a higher turn-on voltage is observed for both smaller R and smaller L_i. Under approximate 1-sun AM1.5G illumination, the simulated *I-V* curves (Figure 5.1C) at various L_i show the same improved diode behavior as apparent in the dark, and the photocurrent shows a strong dependence on L_i, as discussed later.

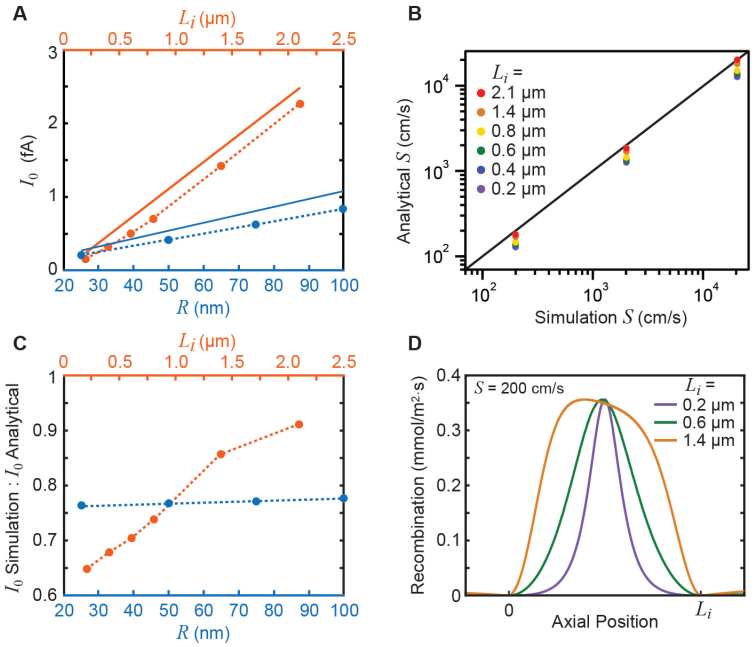

Figure 5.3: Comparison of simulated and analytical PV metrics. (A) I_o as a function of R (blue) and L_i (orange) from simulation (circles and dashed lines) and eq. 5.8 (solid lines) assuming S = 200 cm/s and $L_i = 1\mu m$ (blue data) and S = 2,000 cm/s and R = 110 nm (orange data). (B) Correlation between S parametrized in finite-element simulations and S calculated from eq. 5.13 for R = 110 nm at six values of L_i ranging from 0.2 to 2.1 μm. (C) Ratio of I_o from simulations and from eq. 5.8 as a function of L_i (orange circles) and R (blue circles). The ratio is calculated from the corresponding data in panel A. (D) Recombination rate as a function of axial position at a bias of 0.4 V, with S = 200 cm/s and L_i of 0.2 (purple), 0.6 (green), and 1.4 μ m (orange).

Fits of the dark *I-V* curves in Figures 5.1A-B to the ideal diode equation were used to determine I_o. The dependence of I_o on R and L_i is displayed in Figure 5.3A (circles and dashed lines), showing that I_o increases approximately linearly with both R and L_i, as expected from eq. 5.8 (solid lines in Figure 5.3A). Moreover, S can be calculated from eq. 5.13 using I_o, and a comparison of the S values determined from eq. 5.13 relative to the S values used in various simulations is shown in Figure 5.3B. The results indicate that eqs. 5.8-5.13 correctly predict the values of both I_o and S within a factor of $\sim$2

or better. The ratio of I_o from simulations and from eq. 5.8 is plotted in Figure 5.3C as a function of R and L_i. The ratio is relatively independent of R but is strongly dependent on L_i, increasing toward unity for longer values. The trend can be explained by examining the spatial dependence of recombination within the depletion region for different L_i, as shown in Figure 5.3D. As is apparent from this plot, the recombination width (i.e. the full width at half maximum (FWHM) of each curve in Figure 5.3D) is substantially less than, and does not scale linearly with, L_i. For instance, at L_i of 0.2, 0.6, and 1.4 μm, the recombination FWHM equals 19, 38, and 69% of L_i. This effect indicates that eq. 5.8 tends to overestimate I_o because it overestimates the length of the intrinsic region that contributes to the overall dark saturation current of the diode. Similarly, eq. 5.13 underestimates the value of S because the recombination current is effectively divided over a larger area of the surface, lowering the calculated value. Nevertheless, because the difference between the values is a factor of two or less, this analysis suggests that a dark *I-V* curve measurement should be sufficient to estimate I_o and S in real devices using eqs. 5.8 and 5.13.

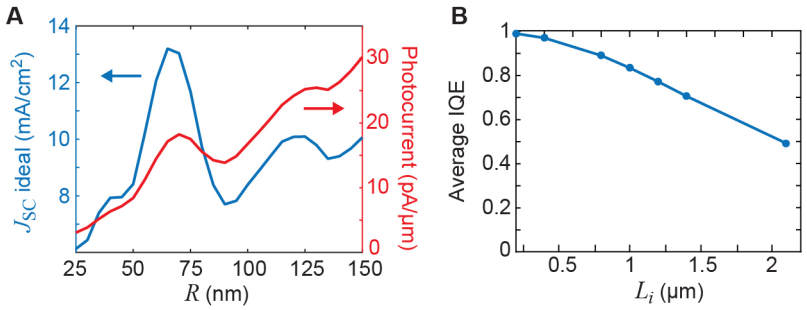

Figure 5.4: Geometry-dependent photocurrent and IQE. (A) J_{SC}^{ideal} (blue) and expected photocurrent per unit length (red) as a function of NW radius, based on finite element simulations of absorption convoluted with the solar spectrum. (B) Finite element simulation of average IQE within the intrinsic region of a *p-i-n* NW with R = 110 nm and S = 200,000 cm/s.

Under 1-sun illumination, the I_{SC} varies greatly with L_i, as apparent from the *I-V* curves in Figure 5.1C. I_{SC} depends both on light absorption in the NW and the spatially-dependent internal quantum efficiency (IQE) of the *p-i-n* junction. To account for light absorption in a NW with radius R, the ideal short-circuit current density J_{SC}^{ideal} (assuming an IQE of unity) of a NW illuminated uniformly along its axial length can be calculated as the integral over the wavelength- and radius-dependent absorption efficiency (calculated from finite-element optical simulations) and the incident power density for simulated AM1.5G 1-sun illumination. The values and dependence of J_{SC}^{ideal} on R are illustrated in

Figure 5.4, and the accuracy of these values has been verified in prior reports.[45,180] To account for the spatially-dependent IQE, we assume a constant IQE value, Φ_{IQE}, within the depletion region, W_D, and an exponential decay elsewhere.[84] Thus, I_{SC} can be approximated as:

$$I_{SC} = 2J_{SC}^{ideal}\Phi_{IQE}R(W_D + L_n + L_p) = 2J_{SC}^{ideal}\Phi_{IQE}R(L_i + L_n + L_p). \tag{5.14}$$

where L_n and L_p are the effective diffusion lengths of electrons and holes, respectively, as calculated by $L_{n,p} = (D_{p,n}R/2S)^{1/2}$, with $D_{p,n}$ the diffusion constant for electrons (D_n) or holes (D_p). On the right-hand side of eq. 5.14, we again assume that $W_D = L_i$. Thus, this expression predicts that the measured I_{SC} should scale linearly with L_i, as has been observed in previous reports of NW *p-i-n* devices,[56] but should also include an offset reflecting photocurrent generated outside of the depletion region if L_n and L_p are non-negligible. In direct band gap materials, $L_{n,p}$ can be dictated by either radiative or surface recombination, depending on the surface recombination lifetime. When R is large and S is small, $L_{n,p}$ will be dominated by radiative recombination, according to $L_{n,p} = (D_{p,n}/BN_{A,D})^{1/2}$, where $N_{A,D}$ is the dopant concentration in the p- or n-type region. While the denominator of $L_{n,p}$ will thus be smaller for direct band gap materials, the larger J_{SC}^{ideal} and larger diffusion constants can result in a similar quantity of photocurrent generated. At very small values of R, or when S is large ($>10^5$ cm/s), $L_{n,p}$ will be dominated by surface recombination, according to $L_{n,p} = (D_{p,n}R/2S)^{1/2}$. In this regime, however, $L_{n,p}$ is small and represents a negligible fraction of the generated photocurrent.

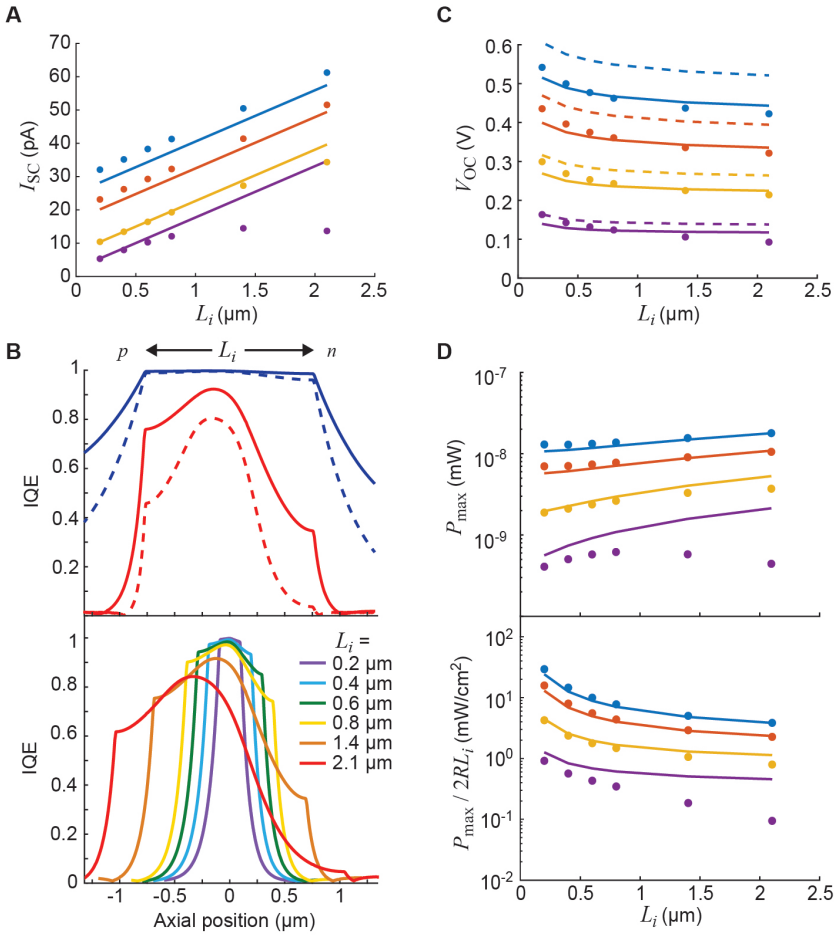

Figure 5.5: The effect of L_i on PV metrics. (A) Comparison of analytically predicted (solid lines) I_{SC} values and those extracted from simulations (circles) for R = 110 nm and S = 200 (blue), 2,000 (orange), 20,000 (yellow) and 200,000 (purple) cm/s. (B) Upper: Plot of IQE as a function of axial position at R of 110 nm (solid lines) and 34 nm (dashed lines) with S = 2000 cm/s (blue) and 200,000 cm/s (red); Lower: IQE vs axial position with S = 200,000 cm/s, R = 110 nm, and L_i of 1.4 (red), 1.2 (orange), 1.0 (yellow), 0.8 (green), 0.4 (blue), and 0.2 μm (purple). (C) Comparison of analytically predicted V_{OC} values (lines) and those extracted from simulations (circles) for R = 110 nm and S = 200 (blue), 2,000 (orange), 20,000 (yellow) and 200,000 (purple) cm/s, when n = 2 (dashed lines) and n = 1.7 (solid lines). (D) Upper: Comparison of analytically predicted (solid lines) P_{max} and those extracted from simulations (circles) for R = 110 nm and S = 200 (blue), 2,000 (orange), 20,000 (yellow) and 200,000 (purple) cm/s. Lower: Comparison of analytically predicted (solid lines) maximum power density ($P_{max}/2RL_i$) and those extracted from simulations (circles) for R = 110 nm and S = 200 (blue), 2,000 (orange), 20,000 (yellow) and 200,000 (purple) cm/s.

To evaluate the validity of eq. 5.14, in Figure 5.5A we plot the I_{SC} of NW devices from simulated *I-V* curves as a function of L_i at a fixed R of 110 nm and S ranging from 200 to 200,000 cm/s, as shown

by the circles in Figure 5.5A. Predictions from eq. 5.14, assuming Φ_{IQE} of unity, are also shown as the solid lines. The two calculations show reasonably good agreement, verifying eq. 5.14. I_{SC} does exhibit a linear relationship with L_i but with a constant offset that increases with lower values of S and extrapolates to a non-zero current at L_i = 0. The non-zero current primarily reflects photocurrent generated in the quasi-neutral n-type and p-type segments but also photocurrent generated within the non-negligible depletion region. At low values of S, the small offset between the simulations and predictions of eq. 5.14 can be explained by the latter, highlighting the limitations of assuming $W_D = L_i$ in eq. 5.14. At high values of S, in contrast, the simulations strongly deviate from the prediction of eq. 5.14, exhibiting a peak and decline at higher values of L_i. This deviation originates from a non-uniform and non-unity value of Φ_{IQE}, as discussed below.

To examine the magnitude and uniformity of IQE, we calculated the spatially-dependent IQE of NWs with various values of R, S, and L_i, as shown in Figure 5.5B. For L_i of 1.4 μm (Figure 5.5B, upper), the IQE of both large (220 nm) and small (68 nm) diameter wires exhibit high values of IQE within the intrinsic region when S = 2,000 cm/s (solid and dashed blue lines, respectively). However, when S = 200,000 cm/s, the IQE of the small diameter wire (dashed red line) is substantially lower than the larger (solid red line). For high S values, the spatial dependence of IQE with different L_i (Figure 5.5B, lower) shows that for small L_i, the average IQE of intrinsic region remains close to 99%. As L_i increases to 2 μm, however, the average IQE drops to $\sim$50% (Figure 5.4). As a result, I_{SC} does not scale linearly with L_i at high values of S, and instead peaks and declines as L_i increases, as shown by the data (purple circles) in Figure 5.5A. Overall, the results in Figure 5.5B show that the IQE within the intrinsic region is relatively independent of both L_i and R for moderate to low values of S ($< 10^4 - 10^5$ cm/s) but is strongly affected by both parameters at high values of S.

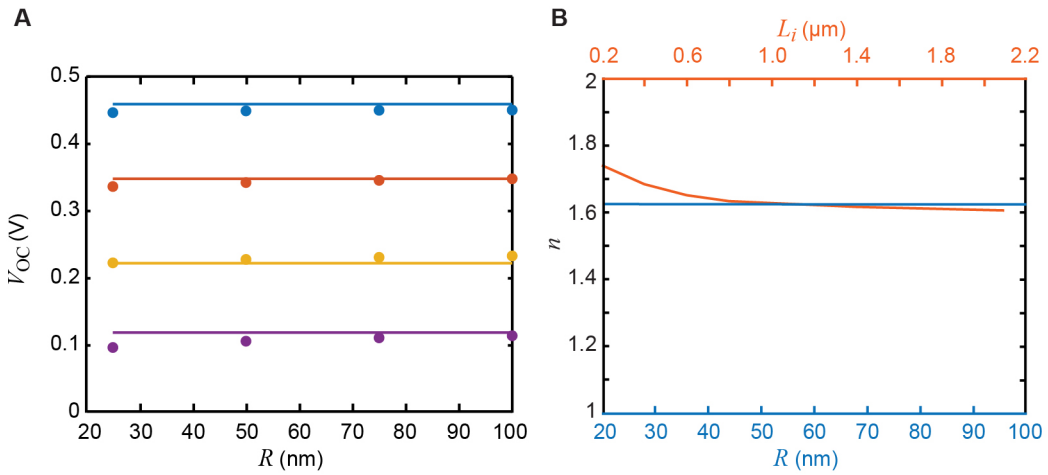

Figure 5.6: Geometrical effects on V_{OC} and n determined by finite-element simulations. (A) Dependence of V_{OC} on R when S = 200 (blue), 2000 (orange), 20,000 (yellow), and 200,000 (purple) cm/s. (B) Dependence of ideality factor n on R (blue) and L_i (orange) when S = 200 cm/s.

In addition to I_{SC}, V_{OC} also depends on geometrical parameters of the NW *p-i-n* junction. Rearranging the ideal diode equation to solve for V_{OC} yields:

$$V_{OC} \approx (nk_BT/q)ln(I_{SC}/I_o) = (nk_BT/q)[ln(2J_{SC}^{ideal}\Phi_{IQE}/q\pi n_i S)+ln(1+(L_n+L_p)/L_i)] \quad (5.15)$$

where k_B is the Boltzmann constant and n is the ideality factor. In the right-hand side of eq. 5.15, we have substituted in the expressions for I_o and I_{SC} from eq. 5.8 and eq. 5.14, respectively. Because I_o and I_{SC} both scale linearly with R, this quantity cancels out of the expression, implying that V_{OC} is independent of R, as verified by finite-element simulations (Figure 5.6. However, V_{OC} still indirectly depends on Rthrough the diameter-dependent light absorption characteristics of the NW, reflected in J_{SC}^{ideal} (*c.f.* Figure 5.6). Interestingly, eq. 5.15 also predicts that V_{OC} should decrease with increasing L_i due to the second logarithmic term on the right-hand side of eq. 5.15, and predicted V_{OC} values from eq. 5.15 for various values of S, assuming $n = 2$, are shown as the dashed lines in Figure 5.5C. To verify this somewhat unexpected prediction, we determined the V_{OC} from finite-element simulations as function of L_i and S, and the results (circles in Figure 5.5C) show good agreement with eq. 5.15 in terms of both absolute magnitude and the trend with L_i. Deviations of the analytical values from the simulation largely result from the assumption that $n = 2$. As shown in Figure 5.6, the n calculated from the simulations is

in the range of 1.6-1.7 and varies slightly with L_i and S. In the derivation of eq. 5.8, it is assumed that the electron concentration and hole concentrations are constant and equal within the depletion region and each vary exponentially with qV/nk_BT, where $n = 2$. As shown in Figure 5.7, the electron and hole concentrations change throughout the intrinsic region and are approximately equal (within a factor of 2-3) only over a relatively short segment of the region. As a result, the ideality factor varies from the ideal value of 2, but an empirically determined value of $n \approx 1.7$ can be used to produce good agreement between eq. 5.15 and simulations, as shown by the solid lines in Figure 5.5C.

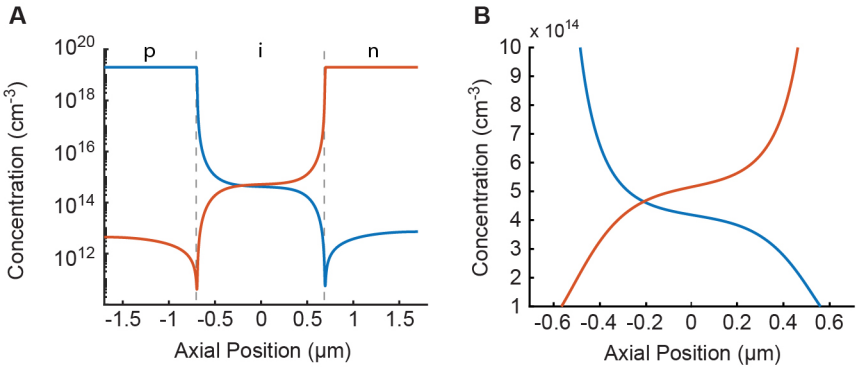

Figure 5.7: Electron and hole concentration in the *p-i-n* junction. (A) Simulated electron (orange) and hole (blue) concentrations within the *p-i-n* structure. Dashed lines indicate the intrinsic region. (B) Simulated electron (orange) and hole (blue) concentrations within the intrinsic region (L_i = 1.4 μm).

The maximum power (P_{max}) generated by the *p-i-n* junctions can be calculated from the product of I_{SC}, V_{OC}, and fill factor (FF), yielding:

$$P_{max} = I_{SC}V_{OC}FF =$$
$$(2J_{SC}^{ideal}\Phi_{IQE}Rnk_BT/q)[ln(2J_{SC}^{ideal}\Phi_{IQE}/q\pi n_i S) + ln(1 + (L_n + L_p)/L_i)](L_i + L_n + L_p)FF, \quad (5.16)$$

where the expressions from eqs. 5.14 and 5.15 have been substituted for I_{SC} and V_{OC}, respectively, on the right-hand side of the expression. In addition, the FF was calculated using the V_{OC} values from eq. 5.15 and the well-known empirical expression[181] derived from the ideal diode equation assuming n = 1.7. The FF ranges from ~0.35 to ~0.75, which is in good agreement with the FF calculated from simulations for all but the highest values of S (Figure 5.8). Because I_{SC} tends to increase with increasing

L_i while V_{OC} tends to decrease, the dependence of P_{max} on L_i is relatively complex. However, as illustrated by the solid lines in the upper panel of Figure 5.5D, P_{max} tends to moderately increase with longer L_i for all values of S, exhibiting an increase of ~60-100% as L_i increases by a factor of 10. Nevertheless, the power density, calculated by dividing P_{max} by the projected area of the intrinsic region as $P_{max}/2RL_i$, decreases, as shown by the lower panel in Figure 5.5D. Values calculated from finite-element simulations are also shown as the circles in Figure 5.5D. At low values of S, eq. 5.16 closely matches the simulation. At high values of S, however, the simulations deviate from eq. 5.16, exhibiting a peak and decline with increasing L_i. This deviation results from the assumption of unity IQE within the intrinsic region, which is violated at high S (c.f. Figure 5.5B). Overall, the results in Figure 5.5D highlight the trade-off between absolute power generation and power density (i.e. power-conversion efficiency) as L_i increases.

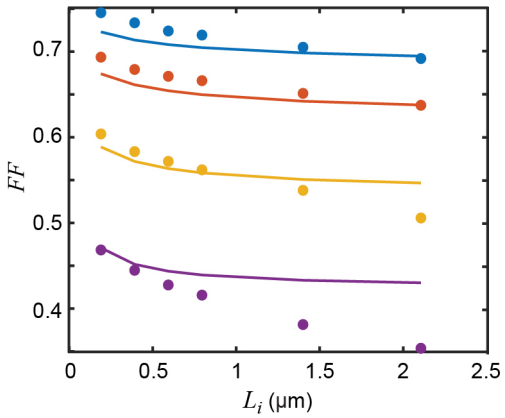

Figure 5.8: Effect of geometry and S on FF. Dependence of FF on L_i when S = 200 (blue), 2000 (orange), 20,000 (yellow), and 200,000 (purple) cm/s. Circles denote the result from finite-element simulations while solid lines reflect the FF calculated from the empirical relationship[181]:

$$FF = (\tilde{V}_{OC} - ln(\tilde{V}_{OC} + 0.72))/(\tilde{V}_{OC} + 1) \quad (5.18)$$

where $\tilde{V}_{OC}$ is the normalized open-circuit voltage defined as qV_{OC}/nk_BT. (C) Dependence of V_{OC} on R when S = 200 (blue), 2000 (orange), 20,000 (yellow), and 200,000 (purple) cm/s.

5.2.2 Experimental Comparison

To experimentally verify our theoretical predictions, we have synthesized Si NWs with geometrically well-defined axial *p-i-n* structures and fabricated single-NW solar cells. Following previous reports,[21,70,170] NWs were synthesized using HCl-stabilized growth conditions that yield degenerately-doped n-type and p-type segments with abrupt dopant transitions. The high doping levels and abrupt

transitions were confirmed by wet-chemical etching of the *p-i-n* junction, as shown in Figure 5.9A. As discussed in prior reports,[28,70] the etch profile directly reflects that encoded dopant profile, confirming sub-20 nm dopant transitions for both the n-type/intrinsic and intrinsic/p-type transitions. Atomic force microscopy (AFM) images over the *p-i-n* region of an unetched NW in Figure 5.9B show a uniform diameter across each dopant transition. Moreover, near-field measurements (Figure 5.9B) of the same junction using infrared s-SNOM show three distinct regions, which can be assigned the p-type, intrinsic, and n-type segments on the basis of prior studies[77] and segment length. The transition widths between each segment are instrument-limited by the size of the AFM tip, thus confirming the abrupt transitions in our as-synthesized *p-i-n* structures.

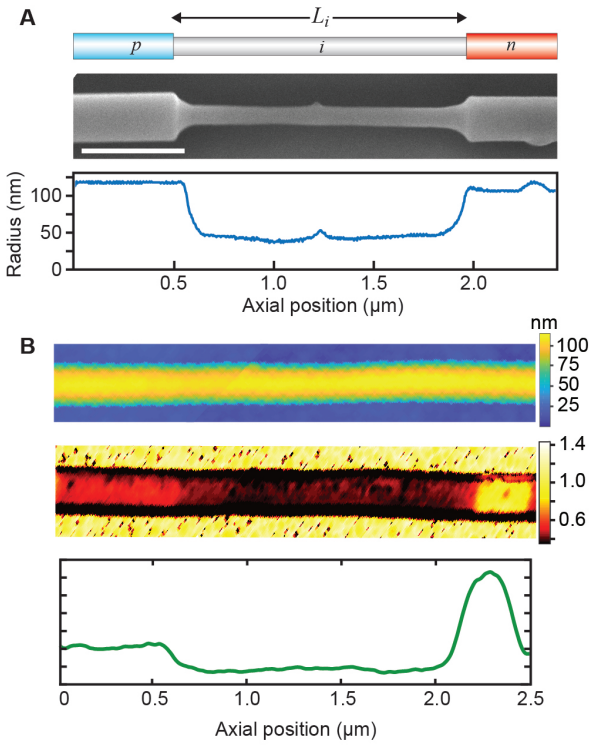

Figure 5.9: Geometrically-defined and degenerately-doped axial *p-i-n* NWs. (A) Schematic (upper) of an etched *p-i-n* junction, SEM images of an etched (middle) and diameter profile (lower) junction; scale bar, 500 nm. (B) AFM image of a *p-i-n* NW (upper), s-SNOM map of near-field signal in a *p-i-n* NW (middle), and a line trace of the s-SNOM signal (lower).

To examine the PV performance of these structures, we performed *I-V* measurements on single-NW devices in the dark and under simulated 1-sun AM1.5G illumination. Because the PV performance is strongly influenced by S, we performed a 950 °C thermal oxidation and hydrogen anneal on some devices

and compared their performance to that of as-grown NWs. Figure 5.10A shows the dark *I-V* curves of two devices, one fabricated from as-grown wires (blue) and one from wires that have undergone the oxidation and annealing treatment (orange). The corresponding simulated AM1.5G 1-sun *I-V* characteristics are depicted in Figure 5.10B. From these curves, we extract the PV device metrics summarized in Table 5.1, which include the V_{OC}, I_{SC}, I_o, n, effective short-circuit current density (J_{SC}), fill factor (FF), and effective power-conversion efficiency (η). The as-grown and treated NW devices exhibit substantial differences in nearly all device metrics. Using the value of I_o and encoded intrinsic length, eq. 5.13 yields values of S of 3200 $\pm$ 300 cm/s and 150 $\pm$ 16 cm/s for the as-grown and treated devices, respectively.

	τ_{SRH} (μs)	S (cm/s)	V_{OC} (V)	I_{SC} (pA)	${J_{sc}}^a$ (mA/cm^2)	FF	η (%)	n	I_o (fA)	R (nm)	L_i (μm)
Untreated NW:											
Experiment	-	3200[c]	0.256	11.3	4.03	0.46	0.47	1.77	24.5	100	1.4
Simulation	1[b]	300	0.258	11.3	4.03	0.50	0.52	1.79	51.1	100	1.4
Treated NW:											
Experiment	-	150[c]	0.376	16.5	5.34	0.68	1.37	1.56	1.25	110	1.4
Simulation	-	300	0.372	16.5	5.34	0.65	1.29	1.78	5.73	110	1.4

Table 5.1: Comparison of experimental and simulated photovoltaic metrics for as-grown and oxidized/annealed axial *p-i-n* NWs measured in the dark and under simulated 1-sun illumination.

[a] estimated using the intrinsic segment projected area for axial NWs

[b] higher values produced similar photovoltaic metrics

[c] calculated using eq. 5.13

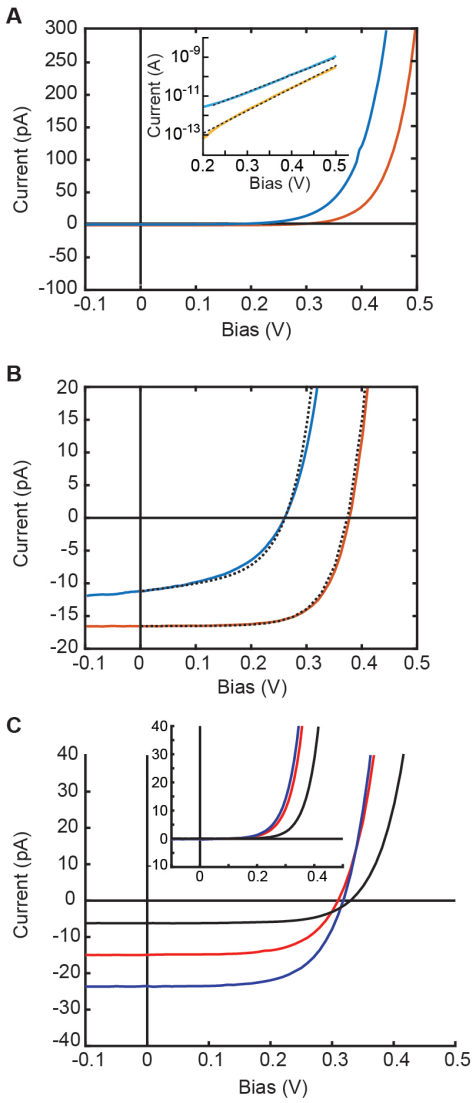

Figure 5.10: Axial *p-i-n* single-NW PV devices. (A) *I-V* curves of as-grown (blue) and treated (orange) devices in the dark. Inset, curves plotted on a log scale with linear fits (dashed lines). (B) Forward bias *I-V* curves of as-grown (solid blue) and treated (solid orange) devices under 1-sun illumination. Corresponding finite-element simulations are shown as dashed lines. (C) *I-V* curves of NW *p-i-n* devices under 1-sun illumination, with intrinsic segment lengths of 0.5 μm (black), 1 μm (red), and 1.5 μm (blue). Inset: *I-V* curves of these devices in the dark.

For comparison, we also performed finite-element simulations to fit the experimental *I-V* data. The as-grown NWs exhibit a finite shunt resistance of $\sim 1x10^{11}$ Ω, which was included in the fit. The best fits to finite-element simulations are shown as the dashed lines in Figure 5.10B and yield values of S of 3000 and 300 cm/s, respectively. The relatively good agreement between the result from eq. 5.13 and the simulations confirms that the diode characteristics of axial *p-i-n* NW devices are almost entirely dictated

by surface recombination within the depletion regions of the structures. Moreover, it experimentally confirms that that the relatively simple measurement of a dark *I-V* curve is sufficient to evaluate S in these devices using eq. 5.13. S of 100-300 cm/s compares favorably to measurements in high-purity bulk Si, which have demonstrated S as low as $\sim$30 cm/s for (100) Si oxidized at 1000 C.[182] The low value of S yields a V_{OC} of 0.376 V and FF of 0.68 under 1-sun illumination. In contrast, previously reported axial *p-i-n* Si NW devices have exhibited V_{OC} values below $\sim$0.3 V,[56,84] which can be attributed to values of S in the range of $10^3 - 10^5$ cm/s.

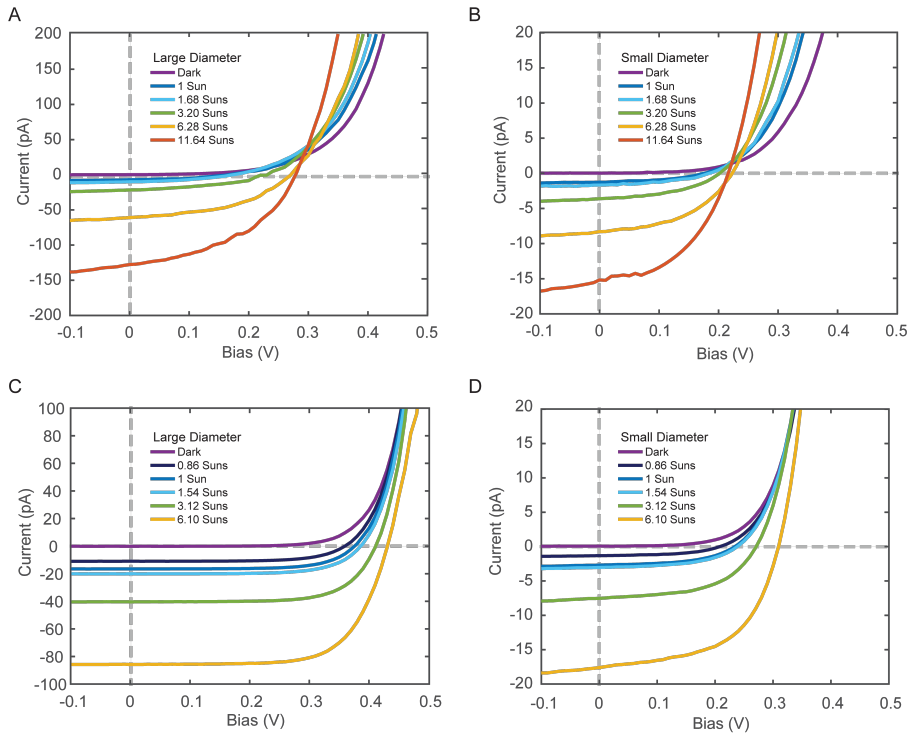

Figure 5.11: PV performance at various illumination intensities after device oxidation and annealing. (A) Large diameter etched *p-i-n* device produced with shallow etching. No oxidation or annealing was performed. While I_{SC} increases greatly as the illumination intensity is increased, there is very little change in V_{OC} between 6.28 suns and 11.64 suns. (B) Small diameter etched *p-i-n* device produced with deep etching. No oxidation or annealing was performed. While I_{SC} increases greatly as the illumination intensity is increased, V_{OC} decreases at higher intensities. (C) Large diameter unetched *p-i-n* device produced with the oxidation and annealing procedure. Both I_{SC} and V_{OC} scale with intensity. (D) Small diameter etched *p-i-n* device produced with the oxidation and annealing procedure. Both I_{SC} and V_{OC} scale with intensity.

To confirm the dependence of I_{SC} and V_{OC} on L_i as predicted in eqs. 5.14 and 5.15, we fabricated *p-i-n* NWs with L_i = 0.5, 1.0, and 1.5 μm. Measurements of these devices under 1-sun illumination yield the *I-V* curves shown in Figure 5.10C and the PV metrics summarized in Table 5.2. As is apparent from this data, the I_{SC} scales linearly with L_i, but the V_{OC} is nearly independent of L_i, with a small increase at shorter L_i. The scaling of I_{SC} is consistent with eq. 5.14 and with IQE values that remain close to unity because of the relatively low S values (c.f. Figure 5.5B). The independence of V_{OC} with respect to L_i is consistent with eq. 5.15 in the limit L_i ¿¿ L_n+L_p, which would occur if S within the doped regions is substantially higher than S within the intrinsic region, as observed previously.[183] All devices exhibit S near 1000 cm/s, which likely reflects only the value within the intrinsic region. As predicted (c.f. Figure 5.3A), I_o increases with L_i, while values for n and FF remain relatively constant, as shown in Figures 5.6 and 5.8, respectively. Note that previously reported axial *p-i-n* Si NW devices exhibited V_{OC} values that substantially increased with increasing L_i.[56] This effect can be attributed to S values that strongly depend on L_i as a result of the specific synthesis conditions used during NW growth.

L_i (μm)	R (nm)	S^b (cm/s)	V_{OC} (V)	I_{SC} (pA)	${J_{sc}}^a$ (mA/cm^2)	FF	η (%)	n	I_o (fA)
0.5	110	1220	0.341	8.0	7.30	0.63	1.57	1.74	3.6
1.0	98	2050	0.310	15.3	7.82	0.61	1.48	1.68	10.7
1.5	126	1450	0.318	23.7	6.26	0.62	1.48	1.69	14.8

Table 5.2: PV metrics oxidized/annealed axial *p-i-n* NW devices with various L_i.

[a] estimated using the intrinsic segment projected area

[b] calculated using eq. 5.13

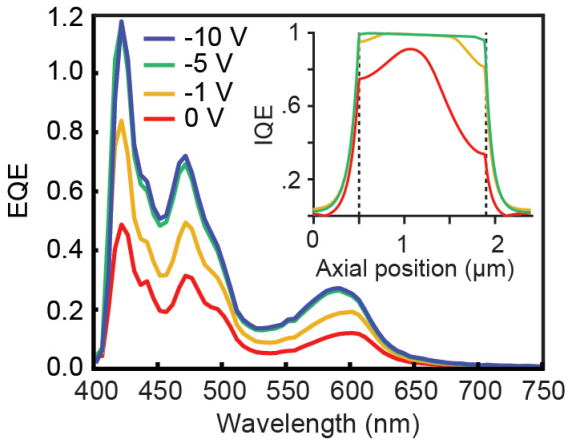

Figure 5.12: Etched *p-i-n* photodiode. EQE spectrum of an etched NW device under TE illumination and reverse bias conditions of 0 V (red), -1 V (yellow), and -5 V (green), and -10 V (blue). Inset, IQE vs axial position, with S = 200,000 cm/s, R = 110 nm, and applied biases of 0 V (red), -1 V (yellow), and -5 V (green).

To explore the IQE of the axial *p-i-n* NW devices, we measured the external quantum efficiency (EQE) spectra of devices as a function of wavelength under various bias conditions. Figure 5.12 displays the EQE spectra of an etched axial *p-i-n* NW with an intrinsic radius of 23 nm and S of 8300 cm/s, as calculated from eq. 5.13 using a measurement of I_o from the dark *I-V* curve (Figure 5.13). Using the calculated value of S, the IQE of this device is not expected to be unity at an applied bias of zero; however, finite-element simulations of IQE (inset of Figure 5.12) indicate that a reverse bias of -5 V should be sufficient to nearly maximize IQE with the intrinsic region. The EQE spectrum progressively improves at -1 V and -5 V but shows no further improvement at lower values. This result is in good agreement with the IQE simulations. The spectra also highlight the potential photodetector applications of the *p-i-n* NWs. Because the spectral response of a NW strongly depends on diameter and polarization,[45,47,180,184–186] selectively etching the intrinsic section of the NW controllably alters the absorption spectrum of the device. The EQE spectrum in Figure 5.12 exhibits peaks that reflect the optical modes of the intrinsic region (see Figure 5.14. However, this etching process introduces surface defects, which increases S and tends to degrade photodetector performance. Nevertheless, our results show that near-unity IQE in the intrinsic region can be achieved under mild reverse bias. Thus, wavelength-tunable NW photodiodes can be created using modulation doping and etching, and surface recombination may be rendered inconsequential through the application of a reverse bias.

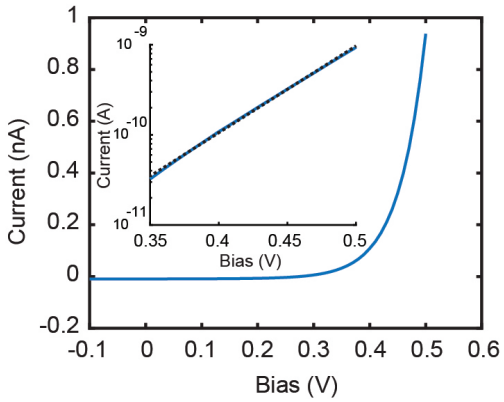

Figure 5.13: Dark *I-V* curve of etched *p-i-n* device. Dark I-V curve of etched *p-i-n* NW photodetector. Inset, a linear fit to a portion of the curve to extract I_o.

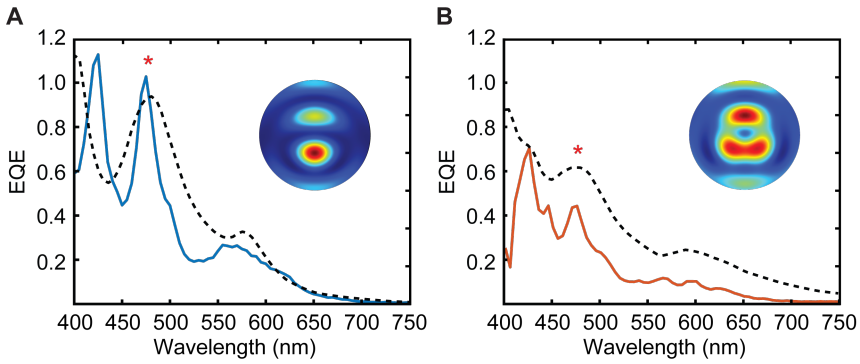

Figure 5.14: Polarization-resolved EQE spectra. (A) EQE spectrum of an etched p-i-n NW under TM illumination (solid blue) and the simulated absorption spectrum (black, dashed). Inset, simulated absorption profile at 480 nm. (B) EQE spectrum the NW shown in panel B under TE illumination (orange) and the simulated absorption spectrum (black, dashed), Inset, simulated absorption profile at 475 nm.

5.3 Conclusions

A combination of theoretical analysis, finite-element simulations, and experimental measurements on single-NW devices has been used to evaluate the effect of diode geometry and surface recombination on the PV performance of axial *p-i-n* junctions. The results reveal a direct analytical connection between the dark saturation current I_o, surface recombination velocity S, and diode geometry (radius R and intrinsic length L_i), thus allowing the prediction of *I-V* curves and PV metrics from the surface and geometrical parameters. Although the photocurrent (I_{SC}) from devices is generally found to increase with increasing

size of the diode (i.e. increasing L_i), the photovoltage (V_{OC}) is surprisingly found to remain constant or decrease, which can be attributed to increases in I_o. In addition, the IQE of devices is found to be uniformly high within the intrinsic region regardless of S for short L_i, but it is found to vary significantly with longer L_i when S is high. Experimental measurements on single-NWs with well-defined geometry and dopant profile, as confirmed by s-SNOM measurements, confirm the theoretical predictions. This analysis on the interplay of surface recombination and geometry provides a framework for the rational design of higher performance axial *p-i-n* junctions for solar energy and solar fuel applications.

CONCLUSIONS

"All men dream: but not equally. Those who dream by night in the dusty recesses of their minds wake up in the day to find it was vanity, but the dreamers of the day are dangerous men, for they may act their dreams with open eyes, to make it possible."

- T.E. Lawrence *Seven Pillars of Wisdom*

Semiconductors provide a promising platform for incorporating nanoscale effects into macroscopic architectures. Bridging this gap, however, requires precise control of nanoscale geometries and their interactions. This work is founded upon understanding the chemical and physical processes that occur during the synthesis of nanowires and their incorporation into devices, and manipulating these factors to highlight the unique properties that can appear in nanoscale materials.

Much of this work is based on the ENGRAVE technique, by which geometric control can be achieved through dopant control. As doping occurs during synthesis, proper understanding of the chemical processes of NW growth fundamentally underlies all further manipulations of structure. Similarly, the electronic properties of diodes depend on the exact location and quantity of dopants within the structure, which ultimately derive from the synthetic techniques.

While the precise geometric control achieved through the ENGRAVE process is unique, properly exploiting their photonic interactions also requires precise control of illumination. Conventional far-field illumination techniques, such as DFM are non-selective: the input wavevector, polarization, and angle of incidence are not well controlled, and the light interacts with both nanoscale and bulk materials. Techniques that are able to more precisely control aspects of the illumination geometry typically utilize lasers and require a complex focusing apparatus. Instead, we present WSM as an alternative technique to produce tightly controlled interactions with anisotropic nanostructures. WSM is simple to implement, making it useful in a wide variety of scenarios. The use of an evanescent field accentuates interactions with nanostructures and suppresses interactions with bulk materials, making it particularly well suited to low-background measurements of nanomaterials. Furthermore, as polarization is tied to the wavevector

of the incident field, the incident polarization can be controlled without the use of polarization optics. As a result, we can controllably excite the unique photonic modes of anisotropic nanostructures with ease.

While being able to access photonic modes is useful, our control of geometry in Si NWs was previously limited to n-type structures. Most active device architectures, whether electronic or optoelectronic require both p- and n-type doping. Therefore, in order to realize NW devices, we needed to expand the ENGRAVE technique to p-type Si. Implementing ENGRAVE not only requires the obvious conditions of degenerate doping levels and abrupt dopant transitions, but also requires straight, uniform NW growth without VS deposition. Many of these problems, however, are endemic to p-type Si growth. By carefully understanding and manipulating the chemical processes of NW growth, we are able to overcome many conventional growth limitations to produce NWs that are suitable for the ENGRAVE process. The growth parameters, especially temperature and HCl content, must strike a balance between competing factors: while surface chlorination helps to prevent VS deposition, it can also slow down dopant evaporation, exacerbating the impact of the reservoir effect. There is a complex interplay between temperature and chemical species that dictates NW growth, and only when these processes are counterbalanced can the desired NWs be produced. These chemical processes also allow us to overcome the barriers of traditional syntheses, producing doping levels well in excess of the solid solubility limit. As VLS is a kinetic process, it is not subject to the same limitations as equilibrium processes, and enables the ENGRAVE process where was once thought impossible. Through chemical control, we are able to create abrupt n-type and p-type segments within a NW under the same conditions, enabling us to produce the unique photonic effects highlighted by WSM in an active, optoelectronic architecture.

While NWs with axial *p-i-n* junctions have been widely explored as microscopic diodes for optoelectronic and solar energy applications, their performance is strongly influenced by charge recombination at the surface, due to their small size. A robust understanding of how geometry and surface quality interacts in these devices has been in part constrained by limited synthetic control. Without abrupt, degenerate doping profiles, the electrostatic environment within the device is complex, and it is difficult to separate out individual effects without extensive modelling. Our synthetic control, however, has afforded us the ability to create well-defined *p-in* junctions, and thus probe the underlying relationship between geometry and surface recombination. We developed an analytical model that can quickly predict NW device properties, and verified this model through both finite-element modelling and experimental device construction. We are able to show how the geometry produces a trade off between various device

metrics, and provide a framework for both designing and interpreting device performance. With these techniques in hand, we have expanded the synthetic repertoire available for nanoscale morphological control. The production of electronically and morphologically complex *p-n* structures, coupled with the ability to control their interactions with light, will provide the basis for new technologies that overcome the limitations of bulk materials.

Among these new technologies is the opportunity to construct more advanced electronic structures within nanowires. While the *p-i-n* structure forms the basis for simplistic solar cells, the voltage that these cells produce is insufficient to perform most electrochemical reactions. By placing these device elements in series, however, a multi-junction cell could be created, in which the photovoltages of each device add together in a $(p\text{-}i\text{-}n)_x$ configuration. Tunnel junctions at the *p-n* interfaces would allow for Ohmic contact between the individual components and produce nearly loss-less voltage addition. Multijunction devices could then be tuned for solar water splitting, CO_2 reduction, or N_2 fixation by adding more *p-i-n* junctions to reach the necessary voltage. The thyristor, a bistable switch that can be gated to conduct in one direction or the other, uses a $(p\text{-}n)_4$ geometry, which could be easily achieved with the synthetic techniques provided herein. Also necessary to thyristor formation is the placement of gate electrode. Using a variant of the ENGRAVE process - selective etching of n-type segments only using HF - the p- and n-type segments could be optically distinguished. Avalanche photodiodes - photodetectors that use avalanche multiplication to enhance their sensitivity - can also be constructed in NWs using these techniques. They often take the form of a $p^+i\text{-}pn^+$ or similar configuration, in which the intrinsic region produces charge carriers, and their acceleration to the $p\text{-}n^+$ junction results in avalanche multiplication. This configuration could produce detectors with single photon sensitivity and high signal-to-noise ratios.[187] An example of this device is shown in Figure 6.1.

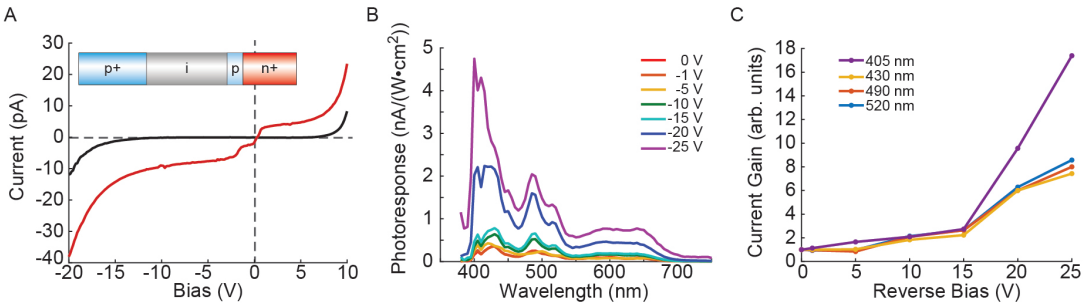

Figure 6.1: Avalanche photodiode. (A) *I-V* curves for an avalanche photodiode in the dark (black) and under illumination (red). Inset, schematic illustration of the avalanche photodiode. (B) EQE spectra of an avalanche photodiode taken at reverse biases of 0 V (red), 1 V (orange), 5 V (yellow), 10 V (green), 15 V (light blue), 20 V (dark blue), and 25 V (purple). (C) Current gain relative to 0 V reverse bias at wavelengths of 405 nm (purple), 430 nm (yellow), 490 nm (orange), and 520 nm (blue).

By taking advantage of the ENGRAVE process, it may also be possible to overcome one of the most fundamental limitations on the use of Si in optoelectronics - its indirect band gap. At small diameters (<5 nm), Si undergoes quantum confinement, transforming from an indirect to a direct band gap material.[188–191] However, quantum confined NWs also exhibit quantized conduction,[192] and no longer obey the simple rules of p- and n-type doping. Instead, the optimal geometry is to produce non-quantum p-type and n-type leads with a quantum, direct band gap gain material in between. Using ENGRAVE, we can produce *p-i-n* structures with etched intrinsic segments, a structure which emulates this ideal device geometry. By taking advantage of kinetically-limited oxidation processes,[193–195] *p-(quantum Si)-n* device could be created. In theory, charge injection from the p- and n-type regions would result in radiative recombination within the quantum Si, producing a Si NW LED. Similarly, these structures should also be suitable for multi-exciton generation, as in other quantum dot systems.[196] An example of this architecture is shown in Figure 6.2.

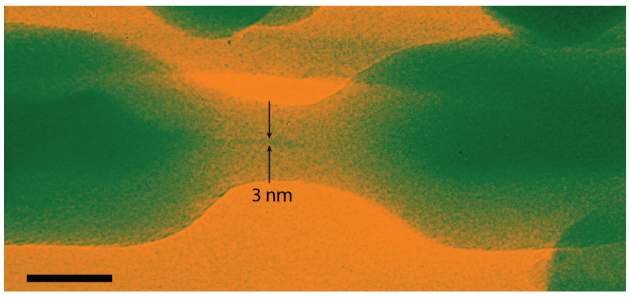

Figure 6.2: Quantum filament. False-color TEM image of a quantum Si filament between two doped segments after etching and self-limiting oxidation; scale bar, 50 nm.

By utilizing Si, which is easily integrated with conventional electronics, in new and unique ways, we expand the limitations of what is possible in electronic and optoelectronic devices.

BIBLIOGRAPHY

"If I have seen further, it is by standing on the shoulders of Giants."

- Isaac Newton

[1] Shockley, W. *Bell Syst. Tech. J.* **1949**, *28*, 435–489.

[2] Sze, S. M. Physics of Semiconductor Devices. 1969; `http://books.google.com/?id=2NTpSnfhResC{&}pg=PA27`.

[3] Ekimov, A. I.; Onushchenko, A. A. Quantum size effect in the optical spectra of semiconductor microcrystals. 1982.

[4] Faraday, M. *Philos. Trans. R. Soc. London* **1857**, *147*, 145–181.

[5] Mie, G. *Ann. Phys.* **1908**, *25*, 377–445.

[6] Wu, B.; Kumar, A.; Pamarthy, S. *Journal of Applied Physics* **2010**, *108*, 51101.

[7] Huang, Z.; Geyer, N.; Werner, P.; de Boor, J.; Gösele, U. *Advanced Materials* **2011**, *23*, 285–308.

[8] Cheung, C. L.; Nikolić, R. J.; Reinhardt, C. E.; Wang, T. F. *Nanotechnology* **2006**, *17*, 1339–1343.

[9] Chou, S. Y.; Krauss, P. R.; Renstrom, P. J. *Science* **1996**, *272*, 85–87.

[10] Wagner, R. S.; Ellis, W. C. *Applied Physics Letters* **1964**, *4*, 89–90.

[11] Christesen, J. D.; Pinion, C. W.; Hill, D. J.; Kim, S.; Cahoon, J. F. *The Journal of Physical Chemistry Letters* **2016**, *7*, 685–692.

[12] Gudiksen, M. S.; Lauhon, L. J.; Wang, J.; Smith, D. C.; Lieber, C. M. *Nature* **2002**, *415*, 617–620.

[13] Heurlin, M.; Magnusson, M. H.; Lindgren, D.; Ek, M.; Wallenberg, L. R.; Deppert, K.; Samuelson, L. *Nature* **2012**, *492*, 90–94.

[14] Hobbs, R. G.; Petkov, N.; Holmes, J. D. *Chemistry of Materials* **2012**, *24*, 1975–1991.

[15] Pinion, C. W.; Christesen, J. D.; Cahoon, J. F. *J. Mater. Chem. C* **2016**, *4*.

[16] Hamano, T.; Hirayama, H.; Aoyagi, Y. *Japanese Journal of Applied Physics* **1997**, *36*, L286–L288.

[17] Bierman, M. J.; Lau, Y. K.; Kvit, A. V.; Schmitt, A. L.; Jin, S. *Science* **2008**, *320*, 1060–1063.

[18] Heitsch, A. T.; Fanfair, D. D.; Tuan, H.-Y.; Korgel, B. A. *Journal of the American Chemical Society* **2008**, *130*, 5436–5437.

[19] Qin, L.; Park, S.; Huang, L.; Mirkin, C. A. *Science* **2005**, *309*, 113–115.

[20] Sun, Y.; Gates, B.; Mayers, B.; Xia, Y. *Nano Letters* **2002**, *2*, 165–168.

[21] Christesen, J. D.; Pinion, C. W.; Grumstrup, E. M.; Papanikolas, J. M.; Cahoon, J. F. *Nano Letters* **2013**, *13*, 6281–6286.

[22] Dick, K. A.; Bolinsson, J.; Borg, B. M.; Johansson, J. *Nano Letters* **2012**, *12*, 3200–3206.

[23] Lim, S. K.; Crawford, S.; Haberfehlner, G.; Grade??ak, S. *Nano Lett.* **2013**, *13*, 331–336.

[24] Qian, F.; Li, Y.; Gradecak, S.; Park, H. G.; Dong, Y.; Ding, Y.; Wang, Z. L.; Lieber, C. M. *Nature Materials* **2008**, *7*, 701–706.

[25] Jacobsson, D.; Panciera, F.; Tersoff, J.; Reuter, M. C.; Lehmann, S.; Hofmann, S.; Dick, K. A.; Ross, F. M. *Nature* **2016**, *531*, 317–322.

[26] Boeisenko, V. E.; Yudin, S. G. *Physica Status Solidi A* **1987**, *101*, 123–127.

[27] Amit, I.; Jeon, N.; Lauhon, L. J.; Rosenwaks, Y. *ACS Applied Materials & Interfaces* **2016**, *8*, 128–134.

[28] Christesen, J. D.; Pinion, C. W.; Zhang, X.; McBride, J. R.; Cahoon, J. F. *ACS Nano* **2014**, *8*, 11790–11798.

[29] Ozel, T.; Bourret, G. R.; Mirkin, C. A. *Nat. Nanotechnol.* **2015**, *10*, 319–324.

[30] Schmid, H.; Borg, M.; Moselund, K.; Gignac, L.; Breslin, C. M.; Bruley, J.; Cutaia, D.; Riel, H. *Appl. Phys. Lett.* **2015**, *106*.

[31] Tian, B.; Kempa, T. J.; Lieber, C. M. *Chemical Society Reviews* **2009**, *38*, 16–24.

[32] Day, R. W.; Mankin, M. N.; Gao, R.; No, Y.-S.; Kim, S.-K.; Bell, D. C.; Park, H.-G.; Lieber, C. M. *Nature Nanotechnology* **2015**, *10*.

[33] Musin, I. R.; Shin, N.; Filler, M. A. *Journal of Materials Chemistry C* **2014**, *2*, 3285–3291.

[34] Vick, G. L.; Whittle, K. M. *Journal of The Electrochemical Society* **1969**, *116*, 1142.

[35] White, C. W.; Wilson, S. R.; Appleton, B. R.; Young, F. W. *J. Appl. Phys.* **1980**, *51*, 738–749.

[36] Reitano, R.; Smith, P. M.; Aziz, M. J. *J. Appl. Phys.* **1994**, *76*, 1518–1529.

[37] Berencén, Y. et al. CMOS-Compatible Controlled Hyperdoping of Silicon Nanowires. 2018.

[38] Zhou, S.; Liu, F.; Prucnal, S.; Gao, K.; Khalid, M.; Baehtz, C.; Posselt, M.; Skorupa, W.; Helm, M. *Sci. Rep.* **2015**, *5*, 8329.

[39] Wen, C. Y.; Tersoff, J.; Reuter, M. C.; Stach, E. A.; Ross, F. M. *Phys. Rev. Lett.* **2010**, *105*.

[40] Moutanabbir, O.; Isheim, D.; Blumtritt, H.; Senz, S.; Pippel, E.; Seidman, D. N. *Nature* **2013**, *496*, 78–82.

[41] Chen, W.; Yu, L.; Misra, S.; Fan, Z.; Pareige, P.; Patriarche, G.; Bouchoule, S.; Cabarrocas, P. R. I. *Nat. Commun.* **2014**, *5*.

[42] Yan, R. X.; Gargas, D.; Yang, P. D. *Nat. Photonics* **2009**, *3*, 569–576.

[43] A STUDY OF CONTACTS TO P- AND N-TYPE SILICON NANOWIRES SYNTHESIZED VIA VAPOR-LIQUID-SOLID GROWTH PROCESS. Ph.D. thesis.

[44] Kuznetsov, A. I.; Miroshnichenko, A. E.; Brongersma, M. L.; Kivshar, Y. S.; Luk'yanchuk, B. *Science* **2016**, *354*.

[45] Cao, L.; Fan, P.; Barnard, E. S.; Brown, A. M.; Brongersma, M. L. *Nano Letters* **2010**, *10*, 2649–2654.

[46] Abujetas, D. R.; Paniagua-Domínguez, R.; Sánchez-Gil, J. A. *ACS Photonics* **2015**, *2*, 921–929.

[47] Bronstrup, G.; Jahr, N.; Leiterer, C.; Csaki, A.; Fritzsche, W.; Christiansen, S.; Brönstrup, G.; Jahr, N.; Leiterer, C.; Csáki, A.; Fritzsche, W.; Christiansen, S. *ACS Nano* **2010**, *4*, 7113–7122.

[48] Zhang, J.; Ding, F.; Zallo, E.; Trotta, R.; Hofer, B.; Han, L.; Kumar, S.; Huo, Y.; Rastelli, A.; Schmidt, O. G. *Nano Letters* **2013**, *13*, 5808–5813.

[49] Kim, S. K.; Zhang, X.; Hill, D. J.; Song, K. D.; Park, J. S.; Park, H. G.; Cahoon, J. F. *Nano Letters* **2015**, *15*, 753–758.

[50] Cao, L.; Fan, P.; Vasudev, A. P.; White, J. S.; Yu, Z.; Cai, W.; Schuller, J. A.; Fan, S.; Brongersma, M. L. *Nano Lett.* **2010**, *10*, 439–445.

[51] Gao, H.; Fu, A.; Andrews, S. C.; Yang, P. *Proc. Natl. Acad. Sci.* **2013**, *110*, 865–869.

[52] Seo, K.; Wober, M.; Steinvurzel, P.; Schonbrun, E.; Dan, Y.; Ellenbogen, T.; Crozier, K. B. *Nano Letters* **2011**, *11*, 1851–1856.

[53] Walia, J.; Dhindsa, N.; Khorasaninejad, M.; Saini, S. S. *Small* **2014**, *10*, 144–151.

[54] Anttu, N.; Abrand, A.; Asoli, D.; Heurlin, M.; Åberg, I.; Samuelson, L.; Borgström, M. *Nano Res.* **2014**, *7*, 816–823.

[55] Ramos, D.; Gil-Santos, E.; Malvar, O.; Llorens, J. M.; Pini, V.; San Paulo, A.; Calleja, M.; Tamayo, J. *Scientific Reports* **2013**, *3*, 3445.

[56] Kempa, T. J.; Tian, B.; Kim, D. R.; Hu, J.; Zheng, X.; Lieber, C. M. *Nano Letters* **2008**, *8*, 3456–3460.

[57] Heurlin, M.; Wickert, P.; Falt, S.; Borgstrom, M. T.; Deppert, K.; Samuelson, L.; Magnusson, M. H. *Nano Lett.* **2011**, *11*, 2028–2031.

[58] Wallentin, J.; Anttu, N.; Asoli, D.; Huffman, M.; Aberg, I.; Magnusson, M. H.; Siefer, G.; Fuss-Kailuweit, P.; Dimroth, F.; Witzigmann, B.; Xu, H. Q.; Samuelson, L.; Deppert, K.; Borgstrom, M. T. *Science* **2013**, *339*, 1057–1060.

[59] Cui, Y.; Wang, J.; Plissard, S. R.; Cavalli, A.; Vu, T. T.; van Veldhoven, R. P.; Gao, L.; Trainor, M.; Verheijen, M. A.; Haverkort, J. E.; Bakkers, E. P. *Nano Lett.* **2013**, *13*, 4113–4117.

[60] Tsakalakos, L.; Balch, J.; Fronheiser, J.; Korevaar, B. A.; Sulima, O.; Rand, J. *Appl. Phys. Lett.* **2007**, *91*, 233117.

[61] Holm, J. V.; Jorgensen, H. I.; Krogstrup, P.; Nygard, J.; Liu, H.; Aagesen, M. *Nat. Commun.* **2013**, *4*, 1498.

[62] Krogstrup, P.; Jørgensen, H. I.; Heiss, M.; Demichel, O.; Holm, J. V.; Aagesen, M.; Nygard, J.; Fontcuberta i Morral, A. *Nat. Photonics* **2013**, *7*, 306–310.

[63] Jain, V.; Heurlin, M.; Barrigon, E.; Bosco, L.; Nowzari, A.; Shroff, S.; Boix, V.; Karimi, M.; Jam, R. J.; Berg, A.; Samuelson, L.; Borgstrom, M. T.; Capasso, F.; Pettersson, H. *ACS Photonics* **2017**, *4*, 2693–2698.

[64] Yang, C.; Barrelet, C. J.; Capasso, F.; Lieber, C. M. *Nano Letters* **2006**, *6*, 2929–2934.

[65] Kim, C. J.; Lee, H. S.; Cho, Y. J.; Kang, K.; Jo, M. H. *Nano Letters* **2010**, *10*, 2043–2048.

[66] Sadaf, S. M.; Ra, Y. H.; Nguyen, H. P.; Djavid, M.; Mi, Z. *Nano Letters* **2015**, *15*, 6696–6701.

[67] Kivisaari, P.; Berg, A.; Karimi, M.; Storm, K.; Limpert, S.; Oksanen, J.; Samuelson, L.; Pettersson, H.; Borgstrom, M. T. *Nano Lett.* **2017**, *17*, 3599–3606.

[68] Perea, D. E.; Allen, J. E.; May, S. J.; Wessels, B. W.; Seidman, D. N.; Lauhon, L. J. *Nano Letters* **2006**, *6*, 181–185.

[69] Schlitz, R. A.; Perea, D. E.; Lensch-Falk, J. L.; Hemesath, E. R.; Lauhon, L. J. *Appl. Phys. Lett.* **2009**, *95*.

[70] Kim, S.; Hill, D. J.; Pinion, C. W.; Christesen, J. D.; McBride, J. R.; Cahoon, J. F. *ACS Nano* **2017**,

[71] Li, Z.; Yang, I.; Li, L.; Gao, Q.; Chong, J. S.; Li, Z.; Lockrey, M. N.; Tan, H. H.; Jagadish, C.; Fu, L. *Prog. Nat. Sci. Mater. Int.* **2018**, *28*, 178–182.

[72] Darbandi, A.; McNeil, J. C.; Akhtari-Zavareh, A.; Watkins, S. P.; Kavanagh, K. L. *Nano Letters* **2016**,

[73] He, K.; Cho, J. H.; Jung, Y.; Picraux, S. T.; Cumings, J. *Nanotechnology* **2013**, *24*, 115703.

[74] Lysov, A.; Vinaji, S.; Offer, M.; Gutsche, C.; Regolin, I.; Mertin, W.; Geller, M.; Prost, W.; Bacher, G.; Tegude, F. J. *Nano Res.* **2011**, *4*, 987–995.

[75] Minj, A.; Cros, A.; Auzelle, T.; Pernot, J.; Daudin, B. *Nanotechnology* **2016**, *27*, 385202.

[76] Sun, X. X.; Wang, X. Q.; Wang, P.; Sheng, B. W.; Li, M.; Su, J.; Zhang, J.; Liu, F.; Rong, X.; Xu, F. J.; Yang, X. L.; Qin, Z. X.; Ge, W. K.; Shen, B. *Opt. Mater. Express* **2017**, *7*, 904–912.

[77] Ritchie, E. T.; Hill, D. J.; Mastin, T. M.; Deguzman, P. C.; Cahoon, J. F.; Atkin, J. M. *Nano Lett.* **2017**, *17*, 6591–6597.

[78] Mohite, A. D.; Perea, D. E.; Singh, S.; Dayeh, S. A.; Campbell, I. H.; Picraux, S. T.; Htoon, H. *Nano Lett.* **2012**, *12*, 1965–1971.

[79] Dan, Y.; Seo, K.; Takei, K.; Meza, J. H.; Javey, A.; Crozier, K. B. *Nano Lett.* **2011**, *11*, 2527–2532.

[80] Zhong, Z. Q.; Li, Z. Y.; Gao, Q.; Li, Z.; Peng, K.; Li, L.; Mokkapati, S.; Vora, K.; Wu, J.; Zhang, G. J.; Wang, Z. M.; Fu, L.; Tan, H. H.; Jagadish, C. *Nano Energy* **2016**, *28*, 106–114.

[81] Zhang, P.; Liu, P.; Siontas, S.; Zaslavsky, A.; Pacifici, D.; Ha, J. Y.; Krylyuk, S.; Davydov, A. V. *J. Appl. Phys.* **2015**, *117*, 125104.

[82] Himwas, C.; Collin, S.; Rale, P.; Chauvin, N.; Patriarche, G.; Oehler, F.; Julien, F. H.; Travers, L.; Harmand, J. C.; Tchernycheva, M. *Nanotechnology* **2017**, *28*, 495707.

[83] Huang, N. F.; Povinelli, M. L. *IEEE J. Photovoltaics* **2014**, *4*, 1511–1517.

[84] Christesen, J. D.; Zhang, X.; Pinion, C. W.; Celano, T. A.; Flynn, C. J.; Cahoon, J. F. *Nano Letters* **2012**, *12*, 6024–6029.

[85] Yu, S.; Roemer, F.; Witzigmann, B. *J. Photonics Energy* **2012**, *2*, 28001–28002.

[86] Chen, Y.; Kivisaari, P.; Pistol, M. E.; Anttu, N. *Nanotechnology* **2018**, *29*, 45401.

[87] Shalev, G. *Nanoscale* **2017**, *9*, 15707–15716.

[88] Fernandes, C.; Shik, A.; Byrne, K.; Lynall, D.; Blumin, M.; Saveliev, I.; Ruda, H. E. *Nanotechnology* **2015**, *26*, 85204.

[89] Solanki, A.; Li, S.; Park, H.; Crozier, K. B. *ACS Photonics* **2017**, *5*, 520–527.

[90] Xu, F.; Lu, W.; Zhu, Y. *ACS Nano* **2010**, *5*, 672–678.

[91] Jain, P. K.; Lee, K. S.; El-Sayed, I. H.; El-Sayed, M. A. *Journal of Physical Chemistry B* **2006**, *110*, 7238–7248.

[92] Hu, M.; Novo, C.; Funston, A.; Wang, H.; Staleva, H.; Zou, S.; Mulvaney, P.; Xia, Y.; Hartland, G. V. *Journal of Materials Chemistry* **2008**, *18*, 1949–1960.

[93] Kelley, K. L.; Coronado, E.; Zhao, L. L.; Schatz, G. C. *Journal of Physical Chemistry B* **2003**, *107*, 668–677.

[94] Link, S.; El-Sayed, M. A. *International Reviews in Physical Chemistry* **2000**, *19*, 409–453.

[95] Harrick, N. J. *Internal Reflection Spectroscopy*; New York, Interscience Publishers, 1967.

[96] Qi, Z.-m.; Matsuda, N.; Yoshida, T.; Asano, H.; Takatsu, A.; Kato, K. *Optics Letters* **2002**, *27*, 2001–2003.

[97] Tcherniak, A.; Ha, J. W.; Dominguez-Medina, S.; Slaughter, L. S.; Link, S. *Nano Letters* **2010**, *10*, 1398–1404.

[98] Huang, X.; El-Sayed, I. H.; Qian, W.; El-Sayed, M. A. *Journal of the American Chemical Society* **2006**, *128*, 2115–2120.

[99] Murphy, C. J.; Gole, A. G.; Stone, J. W.; Sisco, P. N.; Alkilany, A. M.; Goldsmith, E. C.; Baxter, S. C. *Accounts of Chemical Research* **2008**, *41*, 1721–1730.

[100] Gao, X.; Yang, L.; Petros, J. A.; Marshall, F. F.; Simons, J. W.; Nie, S. *Current Opinion in Biotechnology* **2005**, *16*, 63–72.

[101] Rosi, N. L.; Mirkin, C. A. *Chemical Reviews* **2005**, *105*, 15471562.

[102] Jain, P. K.; Huang, X.; El-Sayed, I. H.; El-Sayed, M. A. *Plasmonics* **2007**, *2*, 107–118.

[103] Schultz, S.; Smith, D. R.; Mock, J. J.; Schultz, D. A. *Proceedings of the National Academy of Sciences of the United States of America* **2000**, *97*, 996–1001.

[104] Cao, L. Y.; Fan, P. Y.; Brongersma, M. L. *Nano Letters* **2011**, *11*, 1463–1468.

[105] Willets, K. A.; Van Duyne, R. P. *Annual Review of Physical Chemistry* **2007**, *58*, 267–297.

[106] Fan, J. A.; Bao, K.; Lassiter, J. B.; Bao, J.; Halas, N. J.; Nordlander, P.; Capasso, F. *Nano Letters* **2012**, *12*, 2817–2821.

[107] Knight, M. W.; Fan, J.; Capasso, F.; Halas, N. J. *Optics Express* **2010**, *18*, 2579–2587.

[108] Huang, Y.; Kim, D. H. *Nanoscale* **2011**, *3*, 3228–3232.

[109] Thoma, F.; Armitage, J.; Trembley, H.; Menges, B.; Langbein, U.; Mittler-Neher, S. *Opto-Contact: Workshop on Technology Transfers, Start-up Opportunities, and Strategic Alliances* **1998**, *3414*, 242–249.

[110] Thoma, F.; Langbein, U.; Mittler-Neher, S. *Optics Communications* **1997**, *134*, 16–20.

[111] Nahar, Q.; Fleißner, F.; Shuster, J.; Morawitz, M.; Halfpap, C.; Stefan, M.; Langbein, U.; Southam, G.; Mittler, S. *Journal of Biophotonics* **2013**, Early view DOI:10.1002/jbio.201300135.

[112] Sönnichsen, C.; Geier, S.; Hecker, N. E.; von Plessen, G.; Feldmann, J.; Ditlbacher, H.; Lamprecht, B.; Krenn, J. R.; Aussenegg, F. R.; Chan, V. Z.-H.; Spatz, J. P.; Möller, M. *Applied Physics Letters* **2000**, *77*, 2949–2951.

[113] Yang, S.-C.; Kobori, H.; He, C.-L.; Lin, M.-H.; Chen, H.-Y.; Li, C.; Kanehara, M.; Teranishi, T.; Gwo, S. *Nano Letters* **2010**, *10*, 632–637.

[114] Koen, K. A.; Weber, M. L.; Mayer, K. M.; Fernandez, E.; Willets, K. A. *Journal of Physical Chemistry C* **2012**, *116*, 16198–16206.

[115] Mock, J. J.; Hill, R. T.; Tsai, Y. J.; Chilkoti, A.; Smith, D. R. *Nano Letters* **2012**, *12*, 1757–1764.

[116] Ha, J. W.; Marchuk, K.; Fang, N. *Nano Letters* **2012**, *12*, 4282–4288.

[117] Marchuk, K.; Fang, N. *Nano Letters* **2013**, *13*, 5414–5419.

[118] Axelrod, D.; Burghardt, T. P.; Thompson, N. L. *Annual Review of Biophysics and Bioengineering* **1984**, *13*, 247–268.

[119] Axelrod, D. *Biophysical Journal* **2013**, *104*, 1401–1409.

[120] Ni, W.; Chen, H.; Kou, X.; Yeung, M. H.; Wang, J. *The Journal of Physical Chemistry C* **2008**, *112*, 8105–8109.

[121] Chronis, N.; Lee, L. P. *Lab on a Chip* **2004**, *4*, 125–130.

[122] Grandin, H. M.; Stadler, B.; Textor, M.; Voros, J. *Biosensors & Bioelectronics* **2006**, *21*, 1476–1482.

[123] Hassanzadeh, A.; Nitsche, M.; Mittler, S.; Armstrong, S.; Dixon, J.; Langbein, U. *Applied Physics Letters* **2008**, *92*, 233503.

[124] Agnarsson, B.; Ingthorsson, S.; Gudjonsson, T.; Leosson, K. *Optics Express* **2009**, *17*, 5075–5082.

[125] Asanov, A.; Zepeda, A.; Vaca, L. *Biochimica Et Biophysica Acta-Molecular and Cell Biology of Lipids* **2010**, *1801*, 147–155.

[126] Ramachandran, S.; Cohen, D. A.; Quist, A. P.; Lal, R. *Scientific Reports* **2013**, *3*, 2133.

[127] Sowa, Y.; Steel, B. C.; Berry, R. M. *The Review of Scientific Instruments* **2010**, *81*, 113704.

[128] Ringe, E.; Sharma, B.; Henry, A. I.; Marks, L. D.; Van Duyne, R. P. *Physical Chemistry Chemical Physics* **2013**, *15*, 4110–4129.

[129] Knight, M. W.; Wu, Y.; Lassiter, J. B.; Nordlander, P.; Halas, N. J. *Nano Letters* **2009**, *9*, 2188–2192.

[130] Hecht, E. *Optics*, 4th ed.; Addison Wesley: San Francisco, 2002.

[131] Axelrod, D. *Traffic* **2001**, *2*, 764–774.

[132] Rivas, J.; Muskens, O.; Borgström, M.; Diedenhofen, S.; Bakkers, E. A. M. In *One-Dimensional Nanostructures*; Wang, Z., Ed.; Springer New York, 2008; Vol. 3; Chapter 6, pp 127–145.

[133] Genet, C.; Ebbesen, T. W. *Nature* **2007**, *445*, 39–46.

[134] Degiron, A.; Ebbesen, T. W. *Journal of Optics A: Pure and Applied Optics* **2005**, *7*, S90–S96.

[135] van der Molen, K. L.; Klein Koerkamp, K. J.; Enoch, S.; Segerink, F. B.; van Hulst, N. F.; Kuipers, L. *Physical Review B: Condensed Matter* **2005**, *72*, 045421.

[136] Sven Rühle Elad Koren,, S. G.; Zaban,; Arie, *Optics Express* **2008**, *16*, 21801.

[137] Weintraub, B.; Wei, Y.; Wang, Z. L. *Angewandte Chemie International Edition* **2009**, *48*, 8981–8985.

[138] Li, D.; Wu, Y.; Fan, R.; Yang, P.; Majumdar, A. *Applied Physics Letters* **2003**, *83*, 3186.

[139] Hochbaum, A. I.; Chen, R.; Delgado, R. D.; Liang, W.; Garnett, E. C.; Najarian, M.; Majumdar, A.; Yang, P. *Nature* **2008**, *451*, 163–167.

[140] Dresselhaus, M. .; Chen, G.; Tang, M. .; Yang, R. .; Lee, H.; Wang, D. .; Ren, Z. .; Fleurial, J. P.; Gogna, P. *Advanced Materials* **2007**, *19*, 1043–1053.

[141] Boukai, A. I.; Bunimovich, Y.; Tahir-Kheli, J.; Yu, J. K.; Goddard 3rd, W. A.; Heath, J. R. *Nature* **2008**, *451*, 168–171.

[142] Kim, S. J.; Choi, W. C.; Zyung, T. H.; Jang, M. G. *Applied Physics A* **2015**, *120*, 265–269.

[143] Brouzet, V.; Salem, B.; Periwal, P.; Rosaz, G.; Baron, T.; Bassani, F.; Gentile, P.; Ghibaudo, G. *Applied Physics A* **2015**, *121*, 1285–1290.

[144] Patolsky, F.; Timko, B. P.; Yu, G.; Fang, Y.; Greytak, A. B.; Zheng, G.; Lieber, C. M. *Science* **2006**, *313*, 1100–1104.

[145] Cui, Y.; Wei, Q.; Park, H.; Lieber, C. M. *Science* **2001**, *293*, 1289–1292.

[146] Lu, W.; Xie, P.; Lieber, C. M. *IEEE Transactions on Electron Devices* **2008**, *55*, 2859–2876.

[147] Cui, Y.; Zhong, Z.; Wang, D.; Wang, W. U.; Lieber, C. M. *Nano Letters* **2003**, *3*, 149–152.

[148] Luo, Z.; Jiang, Y.; Myers, B. D.; Isheim, D.; Wu, J.; Zimmerman, J. F.; Wang, Z.; Li, Q.; Wang, Y.; Chen, X.; Dravid, V. P.; Seidman, D. N.; Tian, B. *Science* **2015**, *348*, 1451–1455.

[149] Seidel, H.; Csepregi, L.; Heuberger, A.; Baumgartel, H. *Journal of The Electrochemical Society* **1990**, *137*, 3626.

[150] Palik, E. D. *Journal of The Electrochemical Society* **1982**, *129*, 2051.

[151] Schmid, H.; Bessire, C.; Björk, M. T.; Schenk, A.; Riel, H. *Nano Letters* **2012**, *12*, 699–703.

[152] Mokhberi, A.; Griffin, P. B.; Plummer, J. D.; Paton, E.; McCoy, S.; Elliott, K. *IEEE Transactions on Electron Devices* **2002**, *49*, 1183–1191.

[153] Chen, L.; Lu, W.; Lieber, C. M. **2014**, 1–53.

[154] Farrow, R. F. C. *Journal of The Electrochemical Society* **1974**, *121*, 899.

[155] Pan, L.; Lew, K.-K.; Redwing, J. M.; Dickey, E. C. *Journal of Crystal Growth* **2005**, *277*, 428–436.

[156] Amit, I.; Givan, U.; Connell, J. G.; Paul, D. F.; Hammond, J. S.; Lauhon, L. J.; Rosenwaks, Y. *Nano Letters* **2013**, *13*, 2598–2604.

[157] Musin, I. R.; Boyuk, D. S.; Filler, M. A. *Journal of Vacuum Science & Technology B: Microelectronics and Nanometer Structures* **2013**, *31*, 20603.

[158] Gentile, P.; Solanki, A.; Pauc, N.; Oehler, F.; Salem, B.; Rosaz, G.; Baron, T.; Den Hertog, M.; Calvo, V. *Nanotechnology* **2012**, *23*, 215702.

[159] Oehler, F.; Gentile, P.; Baron, T.; Ferret, P. *Nanotechnology* **2009**, *20*, 475307.

[160] Chou, L. W.; Boyuk, D. S.; Filler, M. A. *ACS Nano* **2015**, *9*, 1250–1256.

[161] Gupta, P.; Coon, P. A.; Koehler, B. G.; George, S. M. *Surface Science* **1991**, *249*, 92–104.

[162] Gao, Q.; Cheng, C. C.; Chen, P. J.; Choyke, W. J.; Yates, J. T. *Thin Solid Films* **1993**, *225*, 140–144.

[163] Gupta, P.; Coon, P. A.; Koehler, B. G.; George, S. M. *The Journal of Chemical Physics* **1990**, *93*, 2827.

[164] Sivaram, S. V.; Hui, H. Y.; de la Mata, M.; Arbiol, J.; Filler, M. A. *Nano Letters* **2016**,

[165] Sun, Z.; Seidman, D. N.; Lauhon, L. J. *Nano Lett.* **2017**, *17*, 4518–4525.

[166] Sze, S.; Irvin, J. *Solid-State Electronics* **1968**, *11*, 599–602.

[167] Connell, J. G.; Yoon, K.; Perea, D. E.; Schwalbach, E. J.; Voorhees, P. W.; Lauhon, L. J. *Nano Letters* **2013**, *13*, 199–206.

[168] Yang, C.; Zhong, Z.; Lieber, C. M. *Science* **2005**, *310*, 1304–1307.

[169] Wallentin, J.; Borgstrom, M. T. *J. Mater. Res.* **2011**, *26*, 2142–2156.

[170] Hill, D. J.; Teitsworth, T. S.; Kim, S.; Christesen, J. D.; Cahoon, J. F. *ACS Appl. Mater. Interfaces* **2017**, *9*, 37105–37111.

[171] Chen, L.; Yang, J.; Klaus, S.; Lee, L. J.; Woods-Robinson, R.; Ma, J.; Lum, Y.; Cooper, J. K.; Toma, F. M.; Wang, L. W.; Sharp, I. D.; Bell, A. T.; Ager, J. W. *Journal of the American Chemical Society* **2015**, *137*, 9595–9603.

[172] Lieber, C. M. *MRS Bull.* **2011**, *36*, 1052–1063.

[173] Spirkoska, D. et al. *Phys. Rev. B Condens. Matter Mater. Phys.* **2009**, *80*.

[174] Hoffmann, S.; Bauer, J.; Ronning, C.; Stelzner, T.; Michler, J.; Ballif, C.; Sivakov, V.; Christiansen, S. H. *Nano Lett.* **2009**, *9*, 1341–1344.

[175] Jung, Y.; Vacic, A.; Perea, D. E.; Picraux, S. T.; Reed, M. A. *Adv. Mater.* **2011**, *23*, 4306–4311.

[176] Huang, N.; Lin, C.; Povinelli, M. L. *J. Appl. Phys.* **2012**, *112*.

[177] Zhang, X.; Xie, H.; Liu, Z.; Tan, C.; Luo, Z.; Li, H.; Lin, J.; Sun, L.; Chen, W.; Xu, Z.; Xie, L.; Huang, W.; Zhang, H. *Angewandte Chemie International Edition* **2015**, *54*, 3653–3657.

[178] Gray, J. L. In *Handb. Photovolt. Sci. Eng.*, 2nd ed.; Antonio Luque, S. H., Ed.; Wiley, 2005; Chapter 3, pp 61–112.

[179] Allen, J. E.; Hemesath, E. R.; Perea, D. E.; Lensch-Falk, J. L.; Li, Z. Y.; Yin, F.; Gass, M. H.; Wang, P.; Bleloch, A. L.; Palmer, R. E.; Lauhon, L. J. *Nat. Nanotechnol.* **2008**, *3*, 168–173.

[180] Kim, S. K.; Day, R. W.; Cahoon, J. F.; Kempa, T. J.; Song, K. D.; Park, H. G.; Lieber, C. M. *Nano Letters* **2012**, *12*, 4971–4976.

[181] Green, M. A. *Solid State Electron.* **1981**, *24*, 788–789.

[182] Suzuki, E.; Takato, H.; Ishii, K.; Hayashi, Y. *Japanese J. Appl. Phys. Part 2-Letters Express Lett.* **1990**, *29*, L2300–L2303.

[183] Gabriel, M. M.; Grumstrup, E. M.; Kirschbrown, J. R.; Pinion, C. W.; Christesen, J. D.; Zigler, D. F.; Cating, E. E.; Cahoon, J. F.; Papanikolas, J. M. *Nano Letters* **2014**, *14*, 3079–3087.

[184] Zhang, X.; Pinion, C. W.; Christesen, J. D.; Flynn, C. J.; Celano, T. A.; Cahoon, J. F. *The Journal of Physical Chemistry Letters* **2013**, *4*, 2002–2009.

[185] Cao, L.; White, J. S.; Park, J. S.; Schuller, J. A.; Clemens, B. M.; Brongersma, M. L. *Nature Materials* **2009**, *8*, 643–647.

[186] Mokkapati, S.; Saxena, D.; Tan, H. H.; Jagadish, C. *Sci. Rep.* **2015**, *5*, 15339.

[187] Bulgarini, G.; Reimer, M. E.; Hocevar, M.; Bakkers, E. P. A. M.; Kouwenhoven, L. P.; Zwiller, V. *Nature Photonics* **2012**, *6*, 455–458.

[188] Shen, M.-Y.; Zhang, S.-L. *Physics Letters A* **1993**, *176*, 254–258.

[189] Yu, D. P.; Bai, Z. G.; Wang, J. J.; Zou, Y. H.; Qian, W.; Fu, J. S.; Zhang, H. Z.; Ding, Y.; Xiong, G. C.; You, L. P.; Xu, J.; Feng, S. Q. *Physical Review B: Condensed Matter* **1999**, *59*, R2498–R2501.

[190] Zheng, W. H.; Xia, J.-B.; Cheah, K. W. *Journal of Physics: Condensed Matter* **1997**, *9*, 5105–5116.

[191] Nolan, M.; O'Callaghan, S.; Fagas, G.; Greer, J. C.; Frauenheim, T. *Nano Letters* **2007**, *7*, 34–38.

[192] Andergassen, S.; Meden, V.; Schoeller, H.; Splettstoesser, J.; Wegewijs, M. R. *Nanotechnology* **2010**, *21*, 2001.

[193] Krzeminski, C. D.; Larrieu, G. *Applied Physics Letters* **2012**, *100*, 263111.

[194] Liu, M.; Jin, P.; Xu, Z.; Hanaor, D. A. H.; Gan, Y.; Chen, C. *Theoretical and Applied Mechanics Letters* **2016**, *6*, 195–199.

[195] Liu, H. I.; Biegelsen, D. K.; Ponce, F. A.; Johnson, N. M.; Pease, R. F. W. *Appl. Phys. Lett.* **1994**, *64*, 1383–1385.

[196] Schaller, R. D.; Klimov, V. I. *Phys. Rev. Lett.* **2004**, *92*.